Adressierung von Adhäsionsrezeptoren durch synthetische Liganden

Dissertation zur Erlangung des akademischen Grades des Doktors der Naturwissenschaften (Dr. rer. nat.)

eingereicht im Fachbereich Biologie, Chemie, Pharmazie

der Freien Universität Berlin

vorgelegt von

Christian Kühne

aus Berlin

2016

Die praktischen Arbeiten wurden am Institut für Laboratoriumsmedizin, Klinische Chemie und Pathobiochemie,

Charité – Universitätsmedizin Berlin

in der Arbeitsgruppe von Dr. J. Dernedde / Univ.-Prof. Dr. R. Tauber angefertigt.

1. Gutachter: Univ.-Prof. Dr. H. Fuchs
                    Institut für Laboratoriumsmedizin, Klinische Chemie und Pathobiochemie
                    Charité – Universitätsmedizin Berlin

2. Gutachter: Univ.-Prof. Dr. R. Haag
                    Institut für Chemie und Biochemie
                    Freie Universität Berlin

Disputation am: 16.12.2016

Für meine Familie.

Inhalt

1 Einleitung

1.1 Zelladhäsion

1.1.1 Adhäsionskaskade der Leukozyten

Unser Immunsystem schützt uns durch angeborene und adaptive Mechanismen vor Schäden durch Mikroorganismen, körperfremde Substanzen oder aber vor entarteten körpereigenen Zellen. Während das angeborene Immunsystem unspezifisch und sofort auf gängige Erkennungsmuster von Pathogenen durch Phagozytose oder Aktivierung des Komplementsystems reagiert, vermittelt die adaptive Immunität einen umfangreicheren, wenn auch weitaus komplexeren und zeitaufwändigeren Schutz.

Wenn Pathogene im Körper mit Makrophagen in Kontakt kommen, werden diese aktiviert und sezernieren Signalmoleküle, die andere Zellen rekrutieren (Chemokine) und stimulieren (Zytokine) können. Die Rekrutierung weiterer Zellen des Immunsystems erfolgt durch die gerichtete Wanderung dieser Zellen entlang eines Signalmolekülgradienten, der sogenannten Chemotaxis. Die Stimulation von Zellen über Zytokine führt zur Zelldifferenzierung und/oder Veränderung deren Expressionsmusters.

Die so ausgelöste Entzündungsreaktion lockt zum einen neue Zellen des Immunsystems an und ermöglicht es diesen zum anderen aus dem Blutgefäßsystem in das umliegende Gewebe auszuwandern. Dort können sie dann Pathogene durch Freisetzung von zytotoxischen Substanzen, wie Enzymen, zellpenetrierenden Peptiden oder Sauerstoffradikalen direkt eliminieren oder durch Markierung mittels Antikörpern oder Komplementproteinen für die Phagozytose präformieren.

Um ein Auswandern in das Gewebe zu ermöglichen, müssen die Leukozyten aus dem Blutstrom an das Gefäßendothel adhärieren und ihre Geschwindigkeit drastisch reduzieren. Dies geschieht durch **1. initialen Kontakt** mit dem Endothel und **2.** anschließendem **Rollen** entlang des Endothels. Diese beiden Schritte werden durch Zelladhäsionsmoleküle der Familie der Selektine ermöglicht. Weiterer Kontakt mit aktivierten Endothelzellen bremst die Leukozyten ab und führt zu **3. langsamen Rollen und** zur **Aktivierung** der beteiligten Zellen. Anschließend kommt es **4.** zur **festen Adhäsion und** zum **Kriechen** der Leukozyten und letztendlich zu **5.** der **Transmigration** durch das Endothel in das Gewebe (Butcher 1991; Ley *et al.* 2007) (Abbildung 1). Durch das langsame Rollen der Leukozyten kommt es durch Kontakt von Chemokinen an G-Protein-gekoppelte Rezeptoren (**GPCR**) zu sogenanntem *outside-in signaling* bei dem intrazelluläre Signalkaskaden aktiviert werden. Im Zuge dieser

Aktivierung verändert sich der Leukozyt morphologisch durch Umbau des Zytoskeletts wodurch er abflacht, noch mehr Kontakt zum Endothel entsteht und die folgende Transmigration ermöglicht. Auch die Präsentation der Oberflächenproteine ändert sich nach Aktivierung. L-Selektin wird durch *shedding*, also Spaltung, von der Oberfläche entfernt (Kishimoto *et al.* 1989). Die Integrine $\alpha_4\beta_7$, **LFA-1** und **VLA-4** ändern durch *inside-out signaling* ihre Konformation in einen hochaffinen Zustand und können auf Seite des Endothels ihre Liganden der Immunoglobin-Superfamilie wie **MADCAM1**, **ICAM1** und **VCAM1** binden und dadurch zur festen Adhäsion sowie zur Transmigration beitragen (Campbell *et al.* 1998; Dunne *et al.* 2002).
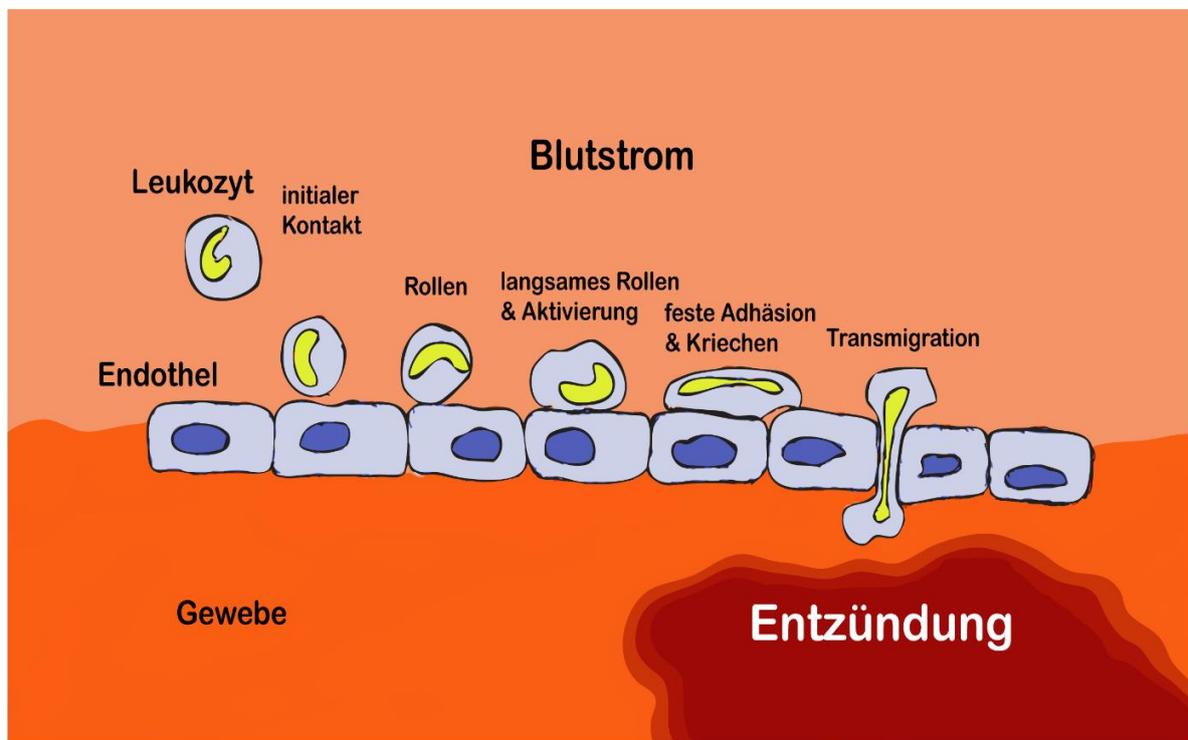
Abbildung 1: Leukozytenadhäsionskaskade

1.1.2 Selektine

Die Selektine vermitteln die ersten beiden Schritte der Leukozytenadhäsionskaskade und damit den initialen Kontakt und das Rollen der Leukozyten auf dem Endothel. Zur Familie der Selektine gehören L-Selektin, P-Selektin und E-Selektin. L-Selektin wird konstitutiv auf den **L**eukozyten selbst exprimiert und ist somit immer bindungsaktiv. P-Selektin wird auf Blutplättchen (*p*latelets) und auf Endothelzellen präsentiert. Es wird nach Expression in den Zellen gespeichert und nach Aktivierung aus α-Granula in den Blutplättchen und aus Weibel-Palade-Körperchen in den Endothelzellen auf der Zelloberfläche präsentiert.

E-Selektin aus **E**ndothelzellen wird nach zellulärer Aktivierung *de novo* synthetisiert (Keelan *et al.* 1994; Kansas 1996).

Sowohl strukturell, als auch funktionell ähneln sich die verschiedenen Selektine. Es sind C-Typ Lektine, die calciumabhängig bestimmte Kohlenhydratstrukturen binden können und besitzen *N*-terminal die **Lektindomäne** gefolgt von einer dem epidermalen Wachstumsfaktor ähnlichen **EGF**-Domäne. Es folgen, je nach Selektin, eine unterschiedliche Anzahl von *short consensus repeats* (**SCR´**s), welche Homologien zu Komplement bindenden Proteinen aufweisen. L-Selektin besitzt zwei SCR´s, humanes E-Selektin sechs und humanes P-Selektin neun. Diesen extrazellulären Bereich schließt sich *C*-terminal eine membranspannende Transmembrandomäne und ein zytoplasmatischer Teil an, über den Signale aus der Zelle heraus (*inside-out*) sowie in die Zelle hinein (*outside-in*) übertragen werden können (Bevilacqua *et al.* 1989; Johnston *et al.* 1989; Lasky *et al.* 1989; Siegelman *et al.* 1989; Siegelman and Weissman 1989; Tedder *et al.* 1989) (Abbildung 2). Trotz der gesamtheitlichen strukturellen Ähnlichkeit zwischen den Selektinen besitzen diese unterschiedliche Affinitäten zu ihrem gemeinsamen Bindungspartner, dem Tetrasaccharid Sialyl Lewis^X (Abbildung 3). Die Lektindomänen von L-, E- und P-Selektin zeigen etwas mehr als 50% Sequenzhomologie (Kansas 1996).
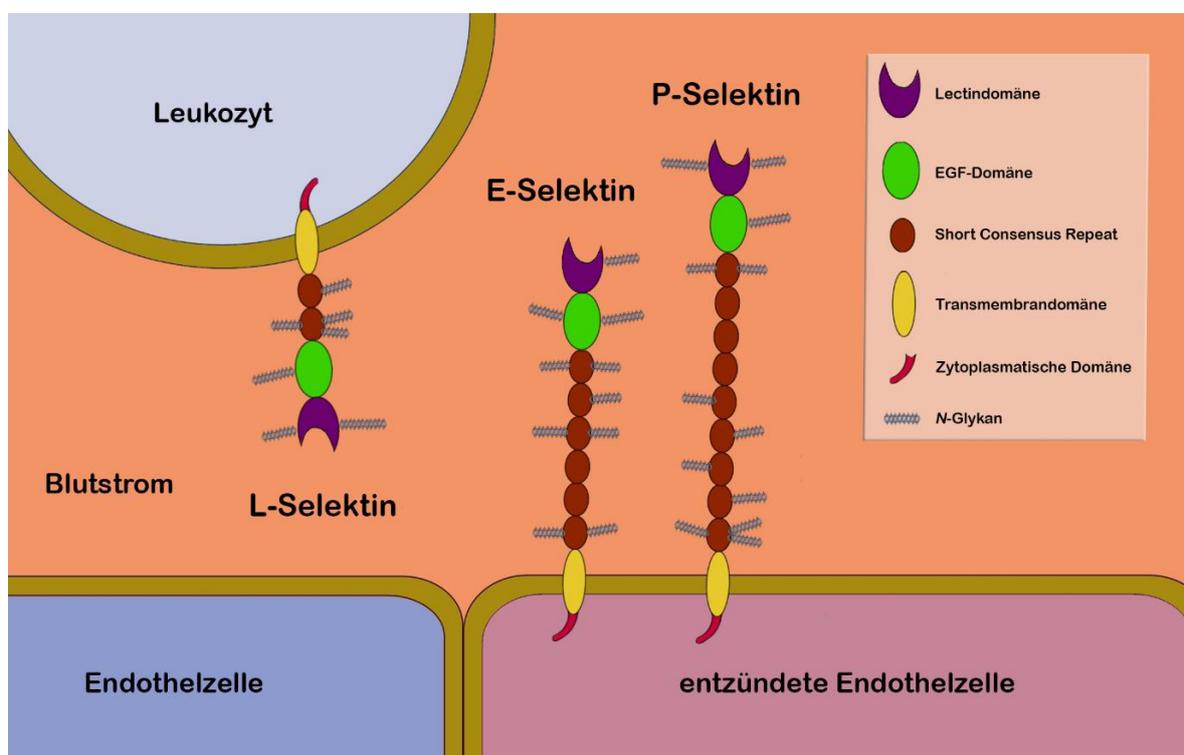

Abbildung 2: Grundstruktur der Selektine, schematisch

Selektine sind als Glykoproteine posttranslational mit Kohlenhydraten modifiziert. Glykosylierungen können als sogenannte *N*-Glykane an Asparagin oder aber als *O*-Glykane an den Aminosäuren Serin, Hydroxylysin, Hydroxyprolin oder Threonin auftreten. Glykanstrukturen sind wichtig bei der Zellerkennung, der Sekretion von Proteinen, der korrekten Faltung, der Löslichkeit von Proteinen und bei der Regulation der Serumhalblebenszeit. Die Selektine selbst sind an verschiedenen Stellen *N*-glykosyliert.

1.1.3 Selektine im pathologischen Kontext

Während die Extravasation der Leukozyten in das umliegende Gewebe im Rahmen einer normalen Immunantwort notwendig und erwünscht ist, kann durch unkontrolliertes Auswandern, zum Beispiel im Falle einer Autoimmunerkrankung wie Morbus Crohn oder rheumatoider Arthritis (Muller 2002), bei der sich das Immunsystem gegen körpereigene Strukturen richtet, umliegendes Gewebe beträchtlich geschädigt werden.

Von Bedeutung ist dies auch bei Erkrankungen, wie Infarkten oder nach Operationen und Transplantationen, bei denen es aufgrund von Ischämie und dem damit verbundenen Sauerstoffmangel bei einer wiederhergestellten Durchblutung zu Reperfusionsschäden kommt (Gumina *et al.* 1996). Die hierbei entstehenden Sauerstoffradikale führen zu direkter Zellschädigung, was wiederum das Immunsystem aktiviert. Die hierdurch eingeleitete Leukozytenauswanderung kann zu einem beträchtlichen Sekundärschaden des Gewebes beitragen.

Da die Selektine den initialen Kontakt der Leukozytenadhäsionskaskade vermitteln, eignen sie sich als Ansatzpunkt, um die überschießende Infiltration von Leukozyten ins Gewebe zu modulieren. Mäusen, welche entweder Selektin- oder Selektinligand-defizient sind, ist es nicht möglich Leukozyten effektiv zu rekrutieren (Jung and Ley 1999; Robinson *et al.* 1999; Lowe 2002).

Patienten mit einer *Leukocyte Adhesion Deficiency type II* (LAD-II) leiden unter bakteriellen Infektionen der Haut und der Schleimhäute. Bei dieser Krankheit können die Selektinliganden durch eine Punktmutation im Fukosetransporter keine Selektine mehr binden, wodurch es im entsprechenden Gewebe zu keiner angemessenen Immunantwort mehr kommt (Etzioni *et al.* 1999). Unter Laborbedingungen zeigen knock-out Mäuse, die keine Fukose auf den Selektinliganden, sLe^x (Abbildung 3) übertragen können aber nur leicht erhöhte Tendenzen zu Hautkrankheiten (Maly *et al.* 1996; Weninger *et al.* 2000; Collins *et al.* 2001). Fehlen ihnen aber E- und P-Selektin entwickeln sich schwere Dermatosen (Bullard *et al.* 1996; Frenette *et al.* 1996). Das Fehlen nur eines Selektins zeigt neben einer 2-4 stündigen Verzögerung der Leukozyteninfiltration nur geringe Defizite in der Hämostase (Mayadas *et al.* 1993). Die

Selektine sind also in ihrer Kombination wichtig für die Generierung einer effizienten Immunantwort. Einzelne Defizite können aber dem Anschein nach gut kompensiert werden.

Betrachtet man auf der anderen Seite aber Krankheitsmodelle, bei denen überschießende Entzündung zu einem Problem wird, zeigt sich bei knock-out Mäusen, denen E-Selektin, P-Selektin oder aber beide fehlen, dass sie vor Neutrophil-abhängigen Schäden, wie beispielsweise Ischämie-Reperfusionsschaden geschützt sind (Singbartl *et al.* 2000; Singbartl and Ley 2000). Auf L-Selektin defiziente Mäuse trifft das für einige dieser Modelle zu (Tedder *et al.* 1995). Auch konnte gezeigt werden, dass in L-Selektin defizienten Mäusen insbesondere das Homing naiver T-Zellen in das lymphatische Gewebe zu 90% reduziert ist (Arbones *et al.* 1994). Beim Homing kehren Leukozyten in primäres lymphatisches Gewebe zurück um dort in Kontakt mit antigenpräsentierenden Zellen zu kommen und zu aktiven Zellen heranzureifen. Generell muss die Anzahl der rollenden Leukozyten auf dem Endothel >90% inhibiert werden bevor es zu signifikanten Effekten in der Neutrophilenrekrutierung kommt (Kubes *et al.* 1995). Außerdem ist die selektinabhängige Leukozytenrekrutierung stark organspezifisch. In Haut, Schleimhäuten, Skelettmuskulatur, Nieren und Herz ist diese in den Tiermodellen stark abhängig von E- und P-Selektin. Leber und Lunge hingegen sind größtenteils unabhängig von selektinabhängiger Leukozytenrekrutierung (Wong *et al.* 1997).

Das Zusammenspiel der unterschiedlichen Selektine, welche einen Funktionsverlust einzelner Selektine während der Immunantwort gegenseitig kompensieren können, als auch der benötigte Grad der Inhibition bis zum vollständigen Verlust der Leukozytenrekrutierung ergeben ein potentielles therapeutisches Fenster, in dem sich eine überschießende Entzündung möglicherweise modulieren lässt ohne die gewünschte Immunantwort vollständig zu unterdrücken.

Neben verschiedenen L-Selektin spezifischen Antikörpern und DNA-Aptameren gegen L-Selektin (Hicke *et al.* 1996; Romig *et al.* 1999; *Riese *et al.* 2016)[1] und P-Selektin (Jenison *et al.* 1998) wurden bisher Glykomimetika und Glykokonjugate (Aydt and Wolff 2002; Ehrhardt *et al.* 2004) für die Inhibition von Selektinen entwickelt. Rivipansel (GMI-1070) ist ein vielversprechender Pan-Selektin-Inhibitor von GlycoMimetics und Pfizer, der sich zurzeit in Phase 3 der Klinischen Studie zur Behandlung vaso-okklusiver Krisen bei Sichelzellanämie befindet (Chang *et al.* 2010). Hierbei akkumulieren E-Selektin abhängig sichelförmige, rote Blutkörperchen im Gefäßendothel, was zu einer Reduktion des Blutflusses und später zu Ischämie führt.

---

[1] Publikationen, die mit einem „*" markiert sind, verweisen auf eigene Autorschaften/Koautorschaften

Vor kurzem wurden dendritische Polymere, welche multivalent Sulfatgruppen präsentieren als potente Inhibitoren für P- und L-Selektin beschrieben. In einem Tiermodell für Kontaktdermatitis konnte die Leukozytenextravasation effektiv reduziert werden. Damit waren diese Polymere so wirksam, wie die bei diesem Krankheitsbild standardmäßig verabreichten Glukokortikoide (Dernedde *et al.* 2010). Diese dendritischen Polyglycerolsulfate (dPGS) inhibieren abhängig von ihrer Größe und Ladungsdichte (Weinhart *et al.* 2011) und konnten auch in einem Tiermodell der Autoimmun-Myositis durch Reduktion der Leukozytenauswanderung den Schweregrad des induzierten Gewebeschadens signifikant mindern (Oishi *et al.* 2014).

1.1.4 Bindungsmotiv der Selektine

Der physiologisch bedeutendste Ligand für alle drei Selektine ist der P-Selektin Glycoprotein Ligand-1 (**PSGL-1**). PSGL-1 wird post-translational mit Sialyl-Lewis^X (sLe^x) modifiziert. Das *O*-Glykan Tetrasaccharid aus Neuraminsäure, Galaktose, *N*-Acetylglucosamin und Fukose ist das minimale Bindungsmotiv für alle Selektine (Abbildung 3).
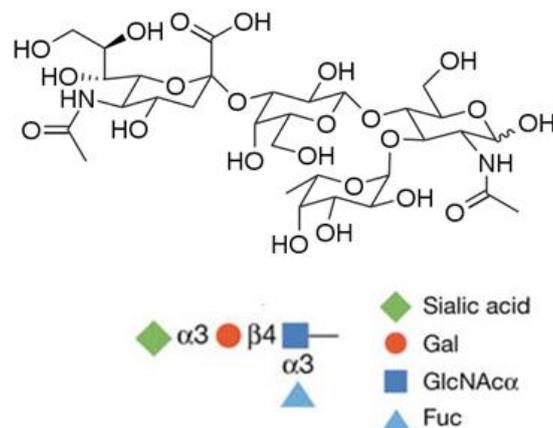
Abbildung 3: Struktur von Sialyl Lewis^X

Zusätzlich ist PSGL-1 in der Nachbarschaft zu sLe^x an Tyrosinresten sulfatiert (Abbildung 4). Diese Sulfatierung führt bei der Bindung an L- und P-Selektin zu einer Bindungsverstärkung im Vergleich zur Bindung an sLe^x allein. E-Selektin dagegen wird von der Sulfatierung nicht beeinflusst (Pouyani and Seed 1995; Sako *et al.* 1995; Mehta *et al.* 1998; Rodgers *et al.* 2001). Mangels der Verfügbarkeit an Kristallstrukturen von L- und E-Selektin ko-kristallisiert mit ihrem Liganden PSGL-1 sind genaue Aussagen über die an der Bindung beteiligten Strukturen schwierig. In der vorliegenden Arbeit wurde deshalb die bekannte ko-kristallisierte Struktur von P-Selektin/PSGL-1 (Somers *et al.* 2000) mit Kristallstrukturen von L-Selektin (ohne Ligand),

E-Selektin (nur *soaked* Struktur mit sLe^x) und P-Selektin (*soaked* mit sLe^x) verglichen (*Woelke *et al.* 2013). In der Röntgenkristallstrukturanalyse von Rezeptor-Ligand Strukturen können nur bei ko-kristallisierten Strukturen sichere Aussagen über die Bindungsverhältnisse getroffen werden, denn hierbei werden Rezeptor und Ligand schon in Lösung zusammengebracht und anschließend kristallisiert. Dagegen kann bei schwieriger zu kristallisierenden Rezeptor-Ligand Fragestellungen zuerst der Rezeptor allein kristallisiert werden, um dann nachträglich den Liganden in Lösung in den Kristall zu geben (*soaked* Struktur). Hierbei kann sich allerdings die Struktur des zu kristallisierenden Rezeptors ändern, was dann zu falschen Konformationen in der Rezeptor-Ligand Kristallstruktur führt. Durch den Vergleich der Selektinstrukturen und Berechnung der Bindungsenergien sollte festgestellt werden, inwieweit die anderen Kristallstrukturen von der ko-kristallisierten Struktur abweichen. Experimentell verifiziert wurde das Bindungsverhalten dann anhand einiger Punktmutationen durch Bestimmung von Bindungsaffinitäten mittels Oberflächenplasmonresonanz (*Woelke *et al.* 2013).
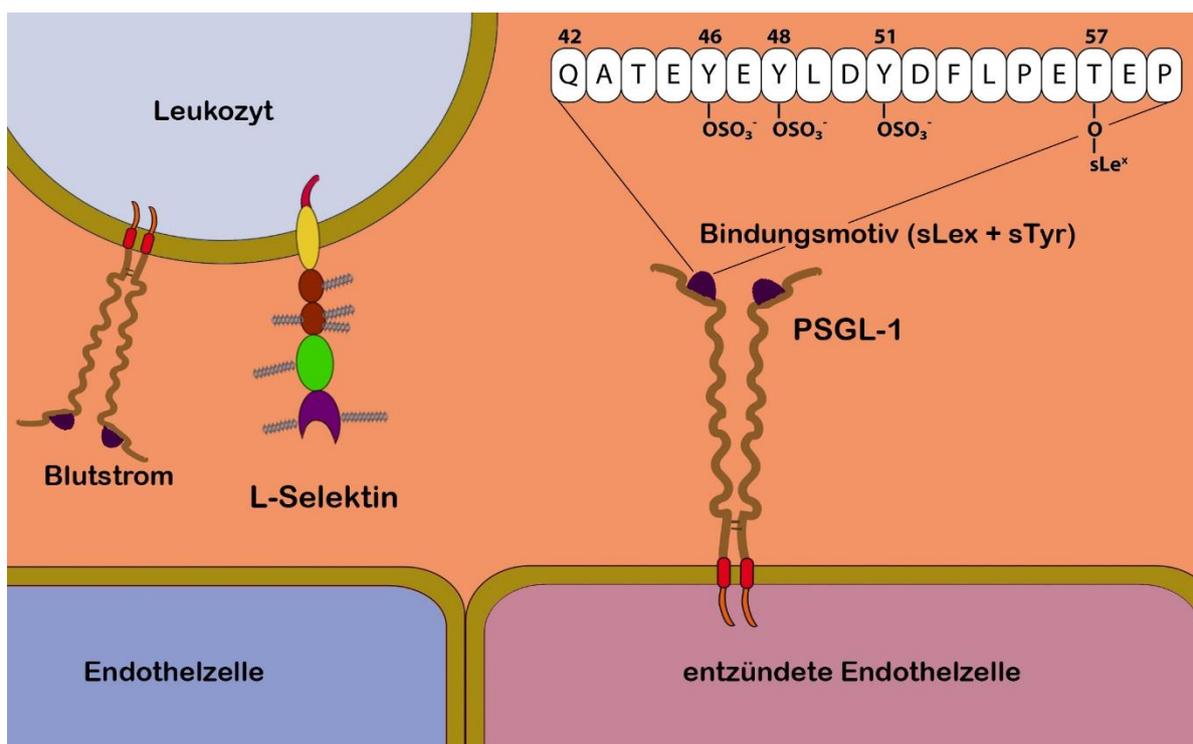

Abbildung 4: Struktur von PSGL-1

1.1.5 *Catch-Bond* **Konzept**

Die Selektin/PSGL-1 Interaktion ist ein Beispiel für eine Bindung die unter Zugkraft ihre Dissoziationszeit verlängert. Werden zwei parallele Flächen durch Scherkräfte gegeneinander verschoben, wirkt Scherstress auf sie. Dieser kann bei sogenannten *catch-bonds* die Lebenszeit der Bindung, gegenüber dem Fall mit geringerer Krafteinwirkung, verlängern. Das *catch-bond* Konzept erklärt, warum Leukozyten in Gefäßen mit hohem Scherstress im Entzündungsfall auf dem Endothel adhärieren können. Eine einzelne Selektin/PSGL-1 Bindung zeigt bis zu einer Zugkraft von 11 pN *catch-bond* Verhalten, darüber dann *slip-bond* Eigenschaften; die Lebenszeit verkürzt sich dann also wieder mit zunehmender Zugkraft (Marshall *et al.* 2003). Strukturell können die Selektine eine gebeugte oder eine gestreckte Konformation einnehmen (Somers *et al.* 2000). Die zugkraftinduzierte gestreckte Variante konnte dabei als affinere Konformation identifiziert werden. Ein durch eine Punktmutation dauerhaft in gestreckter Struktur konserviertes L-Selektin zeigte dabei schon bei geringem Scherstress erhöhte Bindungsaffinität (Konstantopoulos *et al.* 2003; Lou *et al.* 2006). Kürzlich konnte gezeigt werden, dass der L-Selektin spezifische monoklonale Antikörper DREG-55 L-Selektin in der gestreckten Konformation hält. L-Selektin präsentierende Zellen konnten durch Vorinkubation mit DREG-55 im Flusskammerassay auf PSGL-1 ab einem Scherstress von $1 \frac{dyn}{cm^2}$ viel langsamer Rollen als unbehandelte Zellen (*Riese *et al.* 2014). Um die Selektin/PSGL-1 Interaktion zu untersuchen eignen sich also dynamische Assays unter Fluss wie die Flusskammer oder aber SPR viel besser als statische Assays wie ELISA oder MST.

1.2 Inhibitoren

1.2.1 Spezifische Inhibitoren

Die Kristallstruktur der Ligandbindungsstelle der Selektine kann zur gezielten Modellierung von synthetischen Liganden genutzt werden die durch Kompetition die Bindung an natürliche Selektinliganden inhibieren.

Zu den bisher bekannten spezifischen Selektininhibitoren gehören unter anderem monoklonale Antikörper wie die L-Selektin spezifischen Antikörper DREG-56 und DREG-200. Diese binden ihr Epitop direkt in der Lektindomäne und sind dadurch in der Lage, Interaktionen mit anderen Liganden zu blockieren (Jutila *et al.* 1990; Kishimoto *et al.* 1990; *Riese *et al.* 2014).

Zu den momentan prominentesten Vertretern der Ligandmimetika zählt wohl GMI-1070 (Abbildung 5). In der Gruppe von Beat Ernst an der Universität Basel in Kooperation mit GlycoMimetics entwickelt, befindet sich der Pan-Selektin-Inhibitor nun unter dem Namen Rivipansel und Lizenzvertrag mit Pfizer in der Phase 3 der Klinischen Studie. Es ähnelt in seiner Struktur stark dem gemeinsamen Bindungsmotiv der Selektine, sLex, in Kombination mit adjazenten Sulfaten zur Adressierung von L- und P-Selektin. Rivipansel soll durch Blockade der E-Selektin-Ligand-Interaktion ein Verklumpen der Erythrozyten bei Patienten mit Sichelzellanämie verhindern. Die verklumpten roten Blutkörperchen können kleine Blutgefäße verstopfen und zu Durchblutungsstörungen (vaso-okklusiven Krisen) führen. Die Akkumulation kleinerer, schmerzhafter Gerinnsel verursacht im weiteren Verlauf lebensbedrohliche venöse Thrombosen. Eine spätere Zulassung von GMI-1070 für andere Selektin-assoziierte Krankheitsbilder ist bei erfolgreicher Markteinführung von Rivipansel sehr wahrscheinlich.
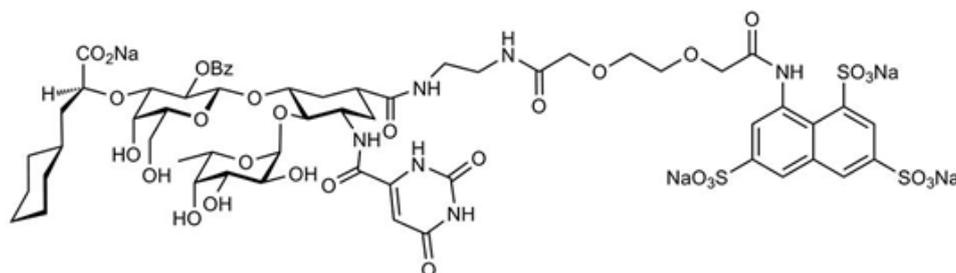

Abbildung 5: Struktur von GMI-1070 (Chang *et al.* 2010)

1996 beschrieben Hicke *et al.* ein L-Selektin spezifisches Aptamer, das Ca^{2+}-abhängig, die Lektindomäne bindet und damit blockierenden Charakter hat (Hicke *et al.* 1996; O'Connell *et*

al. 1996). Das 40 Nukleotide umfassende Aptamer wurde mittels SELEX-Verfahren (*systematic evolution of ligands by exponential enrichment*) identifiziert und besitzt für ein Aptamer eine außerordentliche hohe Bindungsaffinität im niedrigen nanomolaren Bereich an L-Selektin-IgG. 1999 wurde erstmals eine etwas verkürzte Variante (36 Nukleotide, Abbildung 6) des originalen Aptamers zur Aufreinigung von L-Selektin benutzt (Romig *et al.* 1999). Eine kürzlich beschriebene 28 Nukleotid-Version ist mit Blick auf die Schmelztemperatur signifikant stabiler ohne wesentlich an Affinität zu verlieren (*Riese *et al.* 2016). Diese Variante wurde im Rahmen dieser Arbeit auf ihre Bindungsaffinität und auch auf ihren Nutzen für die Aufreinigung von L-Selektin direkt aus Zellkulturüberstand untersucht (*Kuehne *et al.* 2017).
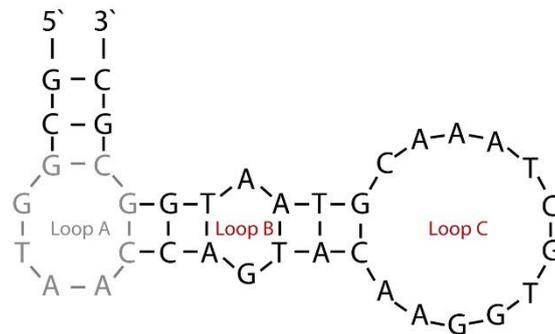
Abbildung 6: gesamt, Struktur des L–Selektin Aptamers (Romig *et al.* 1999)

ausgegraute Sequenz deletiert, Struktur der verkürzten Variante (*Riese *et al.* 2016)

1.2.2 Unspezifische Inhibitoren

Der natürliche Ligand der Selektine, PSGL-1, besitzt neben dem Tetrasaccharid Sialyl-Lewis[X] auch sulfatierte Tyrosine in seinem Bindungsmotiv. Für L- und P-Selektin sind diese negativen Ladungen in der Nähe des Zuckers wichtig für die Bindungsstärke. Bei Bindung an multivalent präsentiertes sLe[x] konnte eine Bindungsverstärkung gegenüber dem Wildtyp für eine die sLe[x]-Bindungstasche betreffende Mutation (D107E) beobachtet werden. Bei gleichzeitiger multivalenter Präsentation von sLe[x] und Tyrosinsulfaten war kein Unterschied messbar (*Woelke *et al.* 2013). Aufgrund der starken Interaktion zwischen L-Selektin und den Tyrosinsulfaten wurde der Gewinn an Bindungsstärke der geänderten Aminosäure maskiert und ist dadurch nicht messbar gewesen (Abbildung 7). Polysulfate sind deshalb potentielle, wenn auch unspezifische Inhibitoren für die L- und P-Selektin-Ligand-Interaktion.
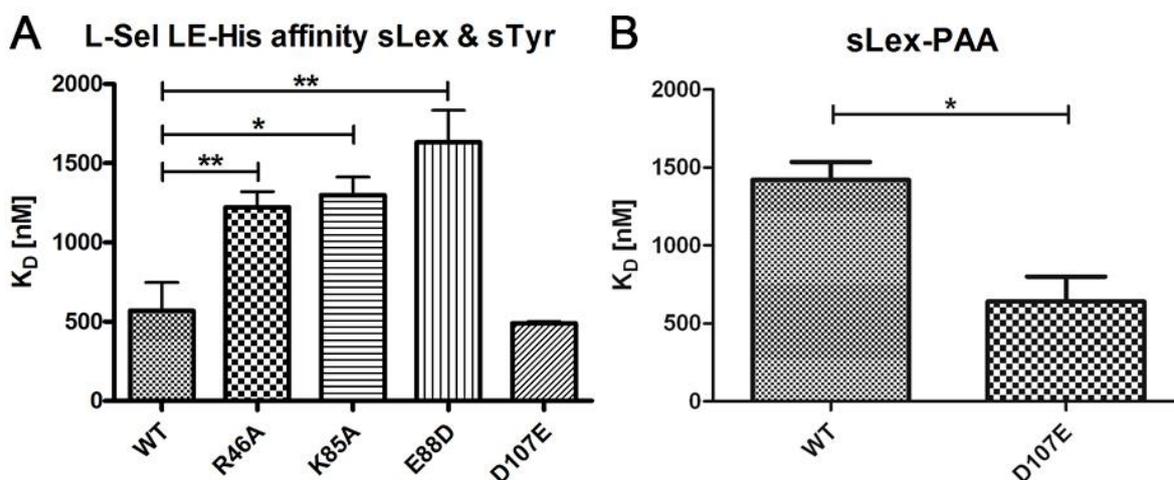
Abbildung 7: A: Affinitäten von L-Selektin-Mutanten an artifizielle sLe^x-Liganden mit und

B: ohne sulfatierte Tyrosine bestimmt mittels SPR. Die Mutante D107E betrifft die sLex Bindungstasche.

Die zuerst von Sunder *et al.* beschriebenen stark verzweigten Polyglycerole (Sunder *et al.* 1999) können sulfatiert werden und wurden zuerst als Heparinanaloga und Inhibitoren für das Komplementsystem beschrieben (Turk *et al.* 2004) (Abbildung 8). In folgenden Untersuchungen zeigte das dendritische Polyglycerolsulfat (dPGS) dann auch als Selektininhibitor, dass es im Tiermodell signifikant Entzündung bei Kontakt-Dermatitis und Lipopolysaccharid (LPS) induzierter Inflammation reduzieren kann (Dernedde *et al.* 2010). Weitere Veröffentlichungen betrachteten den Zusammenhang zwischen Größe, Sulfatierungsgrad, Verzweigungsgrad und der Biokompatibilität sowie dem inhibitorischen Potential von dPGS in einem SPR-basierten artifiziellen L-Selektin Inhibitionsassay (Weinhart *et al.* 2011; Paulus *et al.* 2014). Problematisch blieb bei einer möglichen Anwendung als Therapeutikum allerdings immer die Frage nach der Ausscheidung aus dem Organismus (*Clearance*), sowie, ob der unspezifischen Natur der Substanz geschuldet, die Orte der Akkumulation. Hier wurden deshalb im Rahmen dieser Arbeit neuartige dPGS Moleküle mit pH-sensitiven Linkern getestet, welche im Organismus gespalten und dann ausgeschieden werden können (*Reimann *et al.* 2015). Weiterhin konnten dPGS dekorierte Goldnanostäbchen erfolgreich als Diagnostika im Tiermodell getestet werden (*Vonnemann *et al.* 2014). Hier wurde durch multispektrale optoakustische Tomographie eine Akkumulation der Goldnanostäbchen in den entzündeten Gelenken eines rheumatoiden Arthritismodells beobachtet. Weiterhin wurde die Bindungsaffinität von divalent präsentiertem L-Selektin

(IgG-Chimäre) an dPGS via SPR und *Fluorescence Lifetime Imaging Microscopy* (FLIM) im unteren nanomolaren Bereich bestimmt (*Boreham *et al.* 2015). Die apparente Bindungsstärke von dPGS liegt damit in der Größenordnung der Bindungsaffinität des Aptamers. Trotz der für eine Ein-Schritt-ROMBP (*ring-opening multibranching polymerization*) sehr guten Kontrolle der Polydispersität ist bei der Synthese von dPGS die Massenverteilung sowie die Präsentation der Anionen in absoluten Zahlen immer noch relativ hoch, um später eine Aussage der inhibitorischen Leistung der einzelnen Sulfatgruppen im multivalent präsentierten Verband zu machen und damit Multivalenz entsprechend zu quantifizieren. Deshalb wurden in einer weiterführenden Arbeit sulfatierte, perfekte Dendrone verwendet (*Heek *et al.* 2016). In Verbindung mit einem fluorophoren Kern als Grundgerüst und sehr hoher Quantenausbeute könnten diese dendronisierten Perylenbisimide zum Imaging entzündlicher Prozesse verwendet werden.
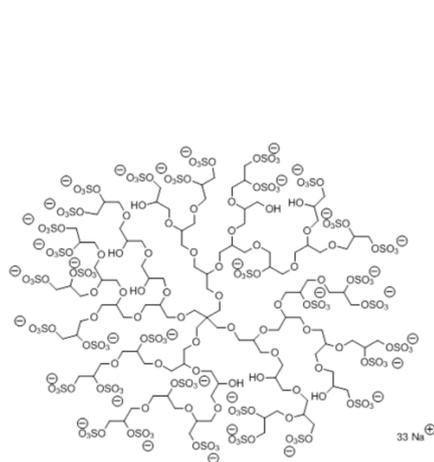

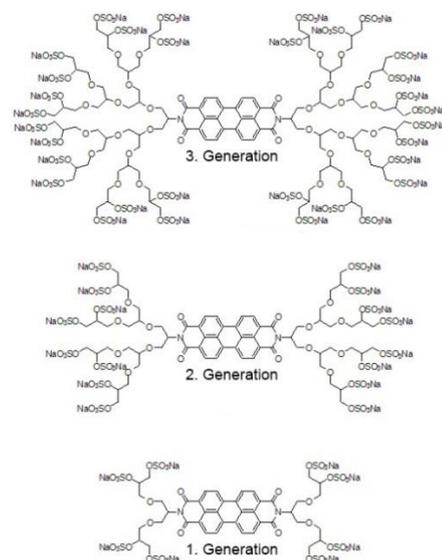Abbildung 8: Struktur von dPGS

(Weinhart *et al.* 2011)

Abbildung 9: Strukturen der dendronisierten Perylenbisimide (Generation 1 bis 3) (*Heek *et al.* 2016)

1.3 Multivalenz

1.3.1 Selektine und Multivalenz

Die monovalente Interaktion der Selektine mit ihren Liganden ist schwach, kann aber durch multivalente Präsentation drastisch gesteigert werden. Im biologischen Kontext verringert dies die Fehleranfälligkeit des Systems, denn einige wenige präsentierte Liganden oder Selektine auf Endothelseite führen nicht sofort zum Auswandern der Leukozyten. Erst im Verbund mehrerer Selektin-Ligand Paare steigt die Bindungsstärke so an, dass Leukozyten in der Lage sind aus dem Blutstrom an das Endothel zu adhärieren. In NMR Experimenten wurde die Bindungsaffinität von monovalentem L-Selektin an sLe^x beispielsweise mit 3,9 mM beziffert (Poppe *et al.* 1997); an PSGL-1 mittels SPR auf 47µM bestimmt (Klopocki *et al.* 2008). In der vorliegenden Arbeit konnte deglykosyliertes, monovalentes L-Selektin an einen artifiziellen Liganden im SPR mit ~1400 nM ohne sulfatierte Tyrosine, und ~600 nM mit sulfatierten Tyrosinen bestimmt werden (*Woelke *et al.* 2013). Die sehr schwachen Bindungsstärken von glykosyliertem L-Selektin an sLe^x oder PSGL-1 reichen nicht aus, um Leukozyten effektiv aus dem Blutstrom heraus zu rekrutieren. Erst die multivalente Präsentation sowie ein *clustern* der Liganden und Selektine führt zu ausreichend hohen Affinitäten.

1.3.2 Der Multivalenzbegriff

Interagieren mehrere miteinander verbrückte Rezeptoren ($m \geq 2$) mit wiederum mehreren miteinander verbrückten Liganden ($n \geq 2$), spricht man von Poly- oder Multivalenz. Während der Begriff der Polyvalenz bislang nur für flächige Interaktionen mit einer hohen Zahl ($n \geq 10$) gebräuchlich war (Joshi *et al.* 2008), erweitert der Begriff der Multivalenz dieses Konzept auch auf grenzflächenunabhängige, sich in Lösung befindliche, mehrbindige Interaktionen (Fasting *et al.* 2012). Der Begriff der Multivalenz beinhaltet auch das Konzept der Kooperativität, bei der die resultierende Bindungsstärke größer ist als nur die Summe der Affinitäten des monovalenten Falles (positive Kooperativität) sowie den Einfluss des Symmetrieeffektes. Durch diesen können die ersten bindenden Liganden eines Rezeptor-Ligand Paares ($m \neq n$) bei genügend großem Unterschied zwischen m und n sowie äquivalenten Bindungsplätzen ($m - n$)-mal häufiger den Rezeptor binden als später bindende Liganden (Ercolani 2003; Ercolani *et al.* 2007).

1.3.3 Bewertung multivalenter Interaktionen

Um den Gewinn an Bindungsstärke im multivalenten Fall gegenüber der monovalenten Bindung quantifizieren zu können, wurde von Whitesides et al. ein Verstärkungsfaktor vorgeschlagen, welcher den Quotienten aus der multivalenten Bindungsaffinität und der

monovalenten Bindungsaffinität darstellt (Mammen *et al.* 1998). Tatsächlich kann in einem einzelnen Bindungsexperiment nur die scheinbare Affinität des gesamten multivalenten Liganden gegenüber seinem multivalenten Rezeptor bestimmt werden. Auch wenn dieser Wert schon reicht, um dieses Rezeptor-Ligand-Paar mit anderen direkt zu vergleichen, kann aus diesem einzelnen Wert noch keine Aussage über Kooperativität gemacht werden. Hierzu muss die Anzahl der Rezeptor-Ligand Interaktionen durch experimentelles und synthetisches Design sukzessive bis hin zum monovalenten Fall bestimmt werden. Auch kann man bei schlecht zugänglichem Experimentaldesign dafür den Umweg über das inhibitorische Potential eines Liganden nehmen, welches benötigt wird, um die Bindung des Rezeptors an einen gut charakterisierten Modellliganden zu verhindern.

So lässt sich beispielsweise die Selektininteraktion zu einem auf Polyacrylamidrückgrat präsentiertem Bindungsmotiv (Polyacrylamid (PAA) +20% sLe^x +5% sTyr) durch verschiedene Ligandmimetika unterdrücken. In einem entsprechenden SPR basierten Ansatz wurden dazu Selektine multivalent auf Goldnanopartikeln präsentiert und als Substrat über den immobilisierten PAA-Liganden gegeben. Das resultierende Bindungssignal wurde dann durch Titration und Vorinkubation von potentiellen Inhibitoren reduziert. Der IC$_{50}$ spiegelt dabei die Konzentration an Inhibitor wider, die notwendig ist um das initiale Bindungssignal um 50% zu reduzieren (Enders *et al.* 2007). Durch diesen Selektin-Inhibitionsassay wurde auch dPGS als potenter Inhibitor für L-und P-Selektin identifiziert (Dernedde *et al.* 2010). Beim Bestimmen von Affinitäten über inhibitorisches Potential spielt für den IC$_{50}$-Wert aber noch die Größe von Rezeptor und Inhibitor, und der Einfluss der abgeschirmten, für andere Binder nicht mehr zugänglichen Flächen, eine Rolle. Dieses *steric shielding* ist im IC$_{50}$-Wert enthalten und muss bei der Berechnung der Affinität beachtet werden. Im Rahmen dieser Arbeit konnte der Effekt des *steric shielding* für globuläre Inhibitoren vom Multivalenzeffekt so getrennt werden, dass beide Faktoren nun einzeln bestimmt werden können (*Vonnemann *et al.* 2015).

2 Motivation und Zielsetzung

Die Selektin-vermittelte Leukozytenadhäsion ist der initiale Schritt für das ortsspezifische Auswandern der Leukozyten aus dem Blutstrom. Damit sind die Selektine wichtig für die Aufrechterhaltung der Immunität und gleichfalls ein interessanter Ansatzpunkt für die Entwicklung antiinflammatorischer Therapeutika bei deregulierten Entzündungsprozessen. Die Notwendigkeit des Zusammenspiels der einzelnen Selektine sowie der multivalente Charakter der Bindung ermöglichen eine gezielte Intervention und eröffnen ein relativ großes therapeutisches Fenster. Ein Pan-Selektin-Inhibitor beispielsweise könnte je nach Krankheitsbild und Schweregrad über einen weiten Konzentrationsbereich verabreicht werden, ohne die Immunität vollständig zu unterdrücken. Durch Auswahl spezifischer Inhibitoren und deren Konzentration könnte eine Therapie an individuelle Krankheitsbilder angepasst werden (personalisierte Medizin).

Ziel der vorliegenden Arbeit ist es daher neue Substanzen, die Adhäsionsrezeptoren adressieren, exemplarisch am Adhäsionsrezeptor L-Selektin zu untersuchen. Der Fokus liegt dabei auf Strukturaufklärung beim spezifischen *Targeting* und der *Traceability* bei unspezifischen Wirkstoffen. Die exakte Kenntnis der Struktur bei spezifischen Wirkstoffen auf der einen, sowie die Frage möglicher weiterer Bindungspartner und der damit verbundenen Biokompatibilität von unspezifischen Wirkstoffen auf der anderen Seite, stellten besondere Anforderungen an die Konzeptentwicklung, das Design unterschiedlicher Assayformate und die Datenevaluation.

Um hoch spezifische Substanzen modellieren zu können, benötigt man ein tiefergehendes Verständnis der Struktur des Rezeptors. Eine korrekte Struktur der zu adressierenden Bindungsstelle wie sie auch *in vivo*, also in gepufferten Lösungen vorkommt, erhält man meist nur durch Ko-Kristallisation mit seinem Liganden. Im Falle von L-Selektin war solch eine Struktur leider nicht verfügbar. Deshalb wird anhand verfügbarer Strukturen für P-Selektin die L-Selektin Kristallstruktur reorientiert und die Gültigkeit der Modellierung experimentell durch Bestimmung von Bindungsaffinitäten von L-Selektin Mutanten überprüft (*Woelke *et al.* 2013).

Hochspezifische Liganden können auch durch Screening von Substanzbibliotheken identifiziert werden. Ein besonderes Verfahren zum Erstellen und screenen solcher Bibliotheken ist das SELEX-Verfahren (*systematic evolution of ligands by exponential enrichment*). Die dabei identifizierten Aptamere sind synthetisch meist gut zugänglich. Ein zuvor beschriebenes L-Selektin spezifisches Aptamer wird im Rahmen dieser Arbeit auf seine

bindungsaffine Kernstruktur hin untersucht und konnte zur Reinigung von rekombinant hergestelltem L-Selektin verwendet werden (*Riese *et al.* 2016).

Bei unspezifischen Liganden wie beispielsweise Polyanionen muss wiederum ein besonderes Augenmerk auf die Biodistribution gelegt werden. Wie verteilt sich die Substanz, wo reichert sie sich an, wie gelangt sie in die Zelle? Die bereits als antiinflammatorisch beschriebenen dendritischen Polyglycerolsulfate werden deshalb durch verschiedene Techniken für *in vivo* als auch für *in vitro* Applikation nachverfolgbar gemacht (*Vonnemann *et al.* 2014; *Heek *et al.* 2016).

Generell stellt sich für alle Substanzen, die perspektivisch *in vivo* verwendet werden sollen, die Frage der Biokompatibilität. Die dendritischen Polyglycerolsulfate reichern sich in Leber und Milz an und besitzen eine unzureichende *Clearance*. Deshalb wurden dendritische Polyglycerolsulfate mit pH-sensitiven Linkern hergestellt und ihr inhibitorisches Potential charakterisiert (*Reimann *et al.* 2015). Weiterhin wurde der Einfluss von Polysulfaten auf die Blutgerinnung und das Komplementsystem hin untersucht (*Heek *et al.* 2016).

Der multivalente Charakter der L-Selektin-Ligand Interaktion stellt besondere Anforderungen an das Experimentaldesign beim Überprüfen größerer Inhibitoren. Sterisch anspruchsvolle Substanzen sind in der Lage Bindungsflächen abzuschirmen ohne möglicherweise einen Gewinn an Affinität zu erzielen. Die Trennung von multivalenter Bindungsstärke und sterischer Abschirmung bei der *in vitro* Validierung neuer Inhibitoren konnte im Rahmen dieser Arbeit mathematisch beschrieben werden (*Vonnemann *et al.* 2015).

3 Publikationen und Manuskripte

In diesem Kapitel werden sowohl die publizierten Arbeiten als auch die eingereichten Manuskripte aufgelistet, wobei der Anteil des Autors an der jeweiligen Arbeit kenntlich gemacht wird.

3.1 Understanding selectin counter-receptor binding from electrostatic energy computations and experimental binding studies

Anna Lena Woelke, Christian Kuehne, Tim Meyer, Gegham Galstyan, Jens Dernedde, Ernst-Walter Knapp
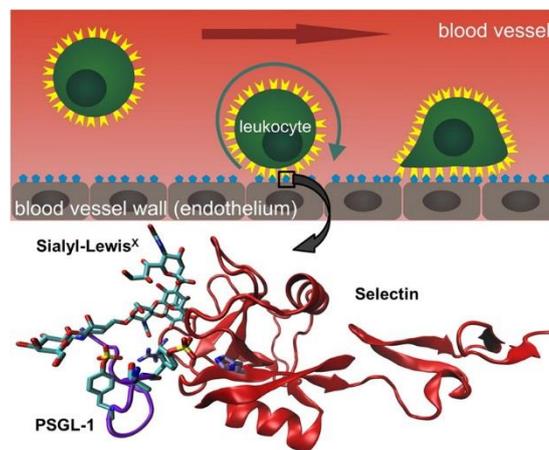
Zu dieser Veröffentlichung hat der Autor mit Teilen des Konzepts, dem Design und der Herstellung der L-Selektin Mutanten, den Bindungsstudien und der Erstellung von Teilen des Manuskripts beigetragen.

Woelke, A. L., C. Kuehne, T. Meyer, G. Galstyan, J. Dernedde and E. W. Knapp (2013) Understanding selectin counter-receptor binding from electrostatic energy computations and experimental binding studies. *The journal of physical chemistry. B*. **117**, 16443-54.

https://dx.doi.org/10.1021/jp4099123

3.2   Structural requirements of mono- and multivalent L-selectin blocking aptamers for enhanced receptor inhibition in vitro and in vivo

Sebastian B. Riese, Konrad Buscher, Sven Enders, Christian Kuehne, Rudolf Tauber, Jens Dernedde
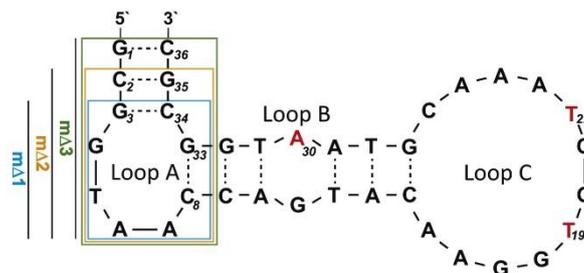
Zu dieser Veröffentlichung hat der Autor mit der Durchführung und Auswertung der SPR Bindungsstudien und der Erstellung von Teilen des Manuskripts beigetragen.

Riese, S. B., K. Buscher, S. Enders, C. Kuehne, R. Tauber and J. Dernedde (2016) Structural requirements of mono-
    and multivalent L-selectin blocking aptamers for enhanced receptor inhibition in vitro and in vivo.
    Nanomedicine : nanotechnology, biology, and medicine. **12**, 901-8.

3.3 Single-step purification of monomeric L-selectin via aptamer affinity chromatography

Christian Kuehne, Stefanie Wedepohl, Jens Dernedde
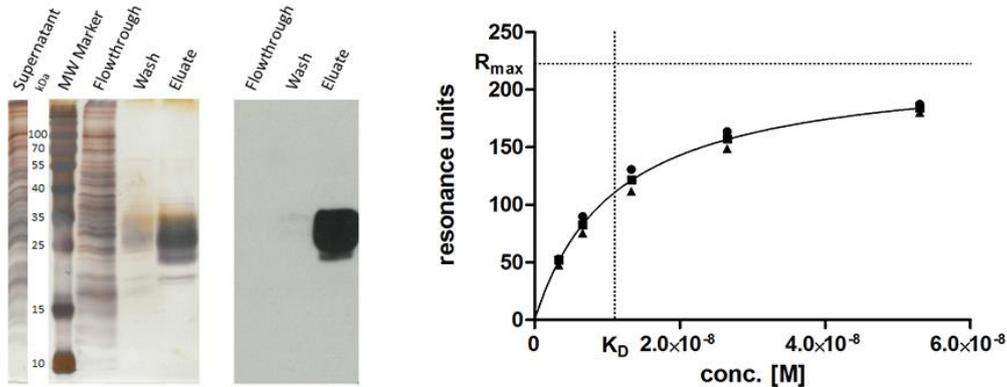
Zu dieser Arbeit hat der Autor mit dem Konzept, der Durchführung und Auswertung der experimentellen Arbeiten und der Erstellung des Manuskripts beigetragen.

Kuehne, C., S. Wedepohl and J. Dernedde (2017) Single-Step Purification of Monomeric l-Selectin via Aptamer Affinity Chromatography. *Sensors*. **17**, 226.

https://dx.doi.org/10.3390/s17020226

Single-step purification of monomeric L-selectin via aptamer affinity chromatography

Christian Kuehne [#], Stefanie Wedepohl [°], Jens Dernedde [#]*

[#]Institute of Laboratory Medicine, Clinical Chemistry and Pathobiochemistry, Charité-Universitätsmedizin Berlin, Germany,

[°] Institute of Chemistry and Biochemistry, Freie Universität Berlin, Germany

* Address correspondence to christian.kuehne@charite.de

Keywords: L-selectin, aptamer, DNA, recombinant protein, purification, affinity, SPR

Abstract

L-selectin is a transmembrane receptor expressed on the surface of white blood cells and responsible for the tethering of leukocytes to vascular endothelial cells. This initial intercellular contact is the first step of the complex leukocyte adhesion cascade that ultimately permits extravasation of leukocytes into the surrounding tissue in case of inflammation. Here we show the binding of a soluble histidine tagged L-selectin to a recently described shortened variant of an L-selectin specific DNA aptamer. The high specificity of this aptamer in combination with its high binding affinity of ~12 nM, allows for a single-step protein purification from cell culture supernatants. In comparison to the well-established Ni-NTA based technology, aptamer affinity chromatography (AAC) was easier to establish, resulted in a 3.6-fold higher protein yield, and increased protein purity. Moreover, due to target specificity, the DNA aptamer facilitated binding studies directly from cell culture supernatant, a helpful characteristic to quickly monitor successful expression of biological active L-selectin.

Introduction

Histidine tagged proteins are widely used in recombinant protein expression as the purification of His-tagged proteins via Ni-NTA is a versatile and well established method. However, to obtain pure and biological active protein in adequate yields, optimization strategies are commonly necessary. Depending on the quality and quantity of unspecific protein binding from crude mixture to the Ni-NTA matrix, different approaches including competitor based binding and washing buffer compositions (e.g. imidazole, high salt, pH, detergents) are needed, but might reduce the overall yield of the target protein. Protein purification via aptamer affinity chromatography (AAC) is an outstanding alternative, if appropriate. The typically high affinity and specificity of aptamers (Keefe et al. 2010, Acquah et al. 2015) result in high yields of pure protein due to very low unspecific binding. Additionally, genetic engineering to equip the target protein with an affinity tag is dispensable. In contrast, for every new target a suitable aptamer has to be created. A further problem might be the essential modification of the aptamer, to link the nucleic acid to a solid support. Slight modifications might change the aptamer structure and render the molecule inactive (Hianik et al. 2005, Acquah et al. 2015).

Selectins are a family of adhesion receptors that recognize the common tetrasaccharide ligand sialy Lewis X. Selectins are involved in the first steps of leukocyte adhesion, which leads to the guidance of immune cells out of the vasculature to sites of inflammation (Ley et al. 2007). Neutralization of pathogens is their task in healthy individuals, but in pathological settings such as rheumatoid arthritis or phenoma like reperfusion injury, the migration of leukocytes from the blood stream to the tissues is dysregulated and contributes to damage of healthy tissue as well (Muller 2002). Here the first step of the adhesion, the tethering of the leukocytes, is a hallmark for the cascade and mainly mediated by the selectins (Sperandio et al. 2006, Ley et al. 2007).

Besides E-selectin that is expressed on activated endothelium and P-selectin that can be found on both, activated endothelium and platelets, L-selectin is expressed by most leukocytes (Ley 2003). The L-selectin specific aptamer LD201 (39 bp) described by Hicke et al. (Hicke et al. 1996) binds in a calcium dependent manner with nanomolar affinity. In 1999 Romig et al. already used a slightly shortened variant (36 bp, LD201mod) of the originally described aptamer for affinity purification of L-selectin IgG fusion protein from CHO cells (Romig et al. 1999). An even shorter version of LD201, LD201mΔ1 (28 bp, Table 1), with comparable affinity but significant increase in stability (i.e. increased melting temperature) was recently described (Riese et al. 2016). In this study we used the 5´biotinylated LD201mΔ1 for purification of the monomeric, C-terminal histidine-tagged L-selectin (LE-His) from cell culture supernatant. Purification was achieved in a single step. Moreover, calibration-free concentration analysis and affinity determination was possible directly from the crude supernatant by surface plasmon resonance.

Table 1. Sequences of the various shortened variants of the originally decribed aptamer

Aptamer	Sequence	Reference
LD201	5´-CAAGGTAACC AGTACAAGGT GCTAAACGTA ATGGCTTCG-3´	Hicke et al. 1996
LD201mod	5´- GCGGTAACC AGTACAAGGT GCTAAACGTA ATGGCGC-3´	Romig et al. 1999
LD201mΔ1	5´- GC C AGTACAAGGT GCTAAACGTA ATGGC-3´	Riese et al. 2016

Materials and Methods

Protein expression

L-selectin LE-His was transiently expressed using the HEK 293-F expression system (Life Technologies, Carlsbad, USA) as described before (Wedepohl et al. 2010). Briefly, LE-His inserted in a pcDNA3 vector (Life Technologies, Carlsbad, USA) was used to transfect 500 ml of 293-F cell suspension at a density of $1*10^6$ cells per ml. After 72 h of incubation at 37°C, 8% CO_2 and shaking at 90 RPM the cell culture supernatant was harvested by centrifugation at 4°C and 6000 x g for 20 min and subsequently processed by sterile filtration.

Preparation of the aptamer column

550 µg of biotinylated L-selectin aptamer LD201mΔ1 (Metabion, Steinkirchen, Germany) were coupled to 1 ml streptavidin agarose (Thermo, Waltham, MA, USA) using PBS with 500 mM NaCl as coupling buffer. Prior to coupling, streptavidin agarose was washed at least 5 times with coupling buffer before incubation with the aptamer for 2 hours at room temperature. Coupling efficiency was monitored by A260 absorption of the supernatant (data not shown).

Purification of L-selectin LE-His

For comparison three different purification strategies were performed via gravity flow columns (A: aptamer, B: Ni-NTA, non-optimized, C: Ni-NTA, optimized procedure). Resin capacities were determined using very small column volumes (i.e. 50 µl) and an excess of cell culture supernatant to fully load the resins and keeping unspecific binding at a minimum. The amount of L-selectin bound to the resin was subsequently determined by ELISA. The column volumes were adjusted according to the resin capacities (capacity Ni-NTA: 0.46 mg/ml and aptamer: 0.32 mg/ml; column volume Ni-NTA: 0.695 ml and apamer: 1 ml). Columns were equilibrated with an excess of appropriate binding buffer (A, PBS +/+, i.e. with 0.9 mM $CaCl_2$ and 0.5 mM $MgCl_2$; B, PBS -/-; C, PBS -/- + 20 mM imidazole). Prior to loading the cell culture supernatant

to Ni-NTA columns the supernatant was supplemented with 1 mM NiSO₄ to avoid Ni-ion leaching from the column and for optimized procedure additionally 20 mM imidazole were included. The flow through was collected and the columns were washed with 30 column volumes (CV) washing buffer each (A, PBS +/+; B, PBS-/- + 10 mM imidazole; C, PBS -/- + 500 mM NaCl + 40 mM imidazole). Bound protein was eluted with 5 CV of elution buffer each (A, PBS -/- + 100 mM EDTA; B and C, PBS -/- + 250 mM imidazole).

SDS-PAGE staining and Western blotting

The purity of the LE-His protein was analyzed under non-reducing conditions on a 13% polyacrylamide gel and visualized by silver staining. Identity of L-selectin was confirmed by Western blotting with subsequent immunodetection using standard protocols with monoclonal antibody DREG-200 (self-prepared from hybridoma) as primary antibody and a goat-anti-mouse HRP-conjugate (Dako, Glostrup, Denmark) as secondary antibody.

Selectin quantification via ELISA and SPR

LE-His was quantified by a sandwich ELISA using DREG-200 as capture and biotinylated DREG-55 (self-prepared from hybridoma with subsequent biotinylation) as detection antibody following standard procedures, whereas human serum (Thermo Fisher Scientific) served as a standard.

Selectin concentration from the cell culture supernatant was additionally determined using calibration free concentration analysis provided by the Biacore X100 with plus package (GE Healthcare, Freiburg, Germany). Here, only the active protein that is able to bind the aptamer is considered. In this set-up samples are injected at flow rates of 10 µl/min and 100 µl/min under mass transfer limitation. Therefore, biotinylated LD201mΔ1 was coupled to 1,900 RU to a streptavidin chip (GE Healthcare, Freiburg, Germany). The reference lane was left untreated. By providing information about the mass (32,114 Da) and the diffusion coefficient (8.5*10⁻

[11] m^2s^{-1}) of the analyte, the built-in software of the Biacore X100 calculates protein concentrations from the slope differences (Christensen 1997, Richalet-Secordel et al. 1997, Sigmundsson et al. 2002). HBS-Ca (20 mM HEPES, pH 7.5, 150 mM NaCl and 1 mM $CaCl_2$) was used as running buffer, 100 mM EDTA as regeneration buffer and cell culture medium of untransfected HEK cells was used as a blank.

Affinity determination via SPR

Binding affinities of L-selectin LE-His to aptamer LD201mΔ1 were measured by kinetic titration series using a Biacore X100 with plus package (GE Healthcare, Freiburg, Germany). A series of five sample dilutions was injected at a flow rate of 30 µl/min over biotinylated LD201mΔ1 coupled to a streptavidin chip (61.4 RU immobilized) (GE Healthcare, Freiburg, Germany) and a mock treated reference lane using running buffer and blanks as mentioned above. Data were analyzed by built-in software of the Biacore X100 (Karlsson et al. 2006) providing analyte concentrations as determined by the above mentioned quantification method via SPR.

Results and Discussion

Protein purification by Ni-NTA and AAC

For better comparison of Ni-NTA and AAC based purification strategies, column capacities were determined prior to protein clean up. Therefore, small columns (50 µl column volume) were run with an excess of cell culture supernatant (100 ml) to keep unspecific binding to both columns at a minimum (data not shown). Larger columns were run after adjustment of the column volume according to the calculated capacities to match the capacity of each column material.

Purification of the monomeric L-selectin LE-His via Ni-NTA by standard procedures as recommended by the manufacturer (Qiagen, Hilden, Germany) did not produce satisfying

results in a one-step purification procedure (Fig. 1, A). The addition of 20 mM imidazole to the supernatant and column washing with increased salt and imidazole concentration (PBS -/- + 500 mM NaCl +40 mM imidazole) significantly contributed to shield unspecific binding and resulted in highly pure LE-His protein. In contrast, AAC yielded highly pure L-sel LE-His within one step without the need for further optimization (Fig. 1, B). The eluate shows the differently glycosylated isoforms of the L-selectin including the non-glycosylated, fastest migrating protein (Wedepohl et al. 2010).
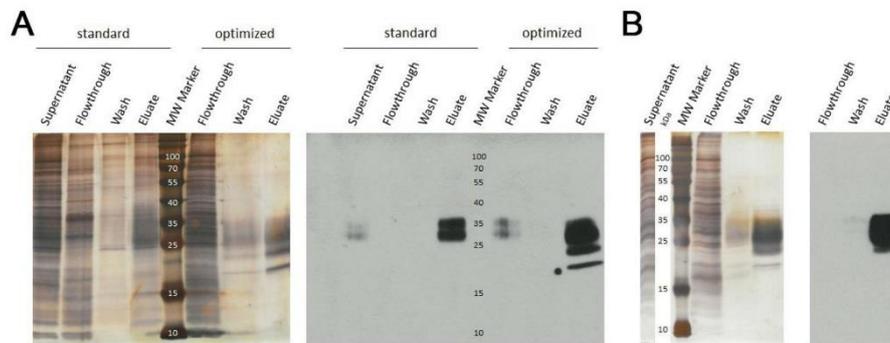
Figure 1, verification of protein purity and identity after A: Ni-NTA chromatography. Left, silver stained SDS-PAGE and right, respective immunoblot detecting L-selectin LE-His. Standard and optimized purification protocols are compared. The molecular weight (MW) marker is given in kDa. B: AAC chromatography. Left, silver stained SDS-PAGE and right, respective immunoblot detecting L-selectin LE-His. The molecular weight (MW) marker is given in kDa.

Aptamer affinity to L-selectin

The originally described aptamer binds to L-selectin with low nanomolar affinity (Hicke et al. 1996). To determine if the shortened 28 bp variant maintains this high affinity binding, SPR analyses were performed. Ascending concentrations of purified monomeric L-selectin (LE-His) cell culture supernatant were injected in a single run (single cycle kinetics; SCK; Fig. 2, A) over the biotinylated and immobilized L-selectin aptamer LD201mΔ1, resulting in an affinity of $K_D = 11.2 \pm 0,8$ nM (Fig. 2, B). Related to the original full length aptamer that showed an affinity of 1.8 nM to dimeric L-selectin Fc-chimera in a filter binding assay (Hicke et al. 1996), this is a comparable result. Prior to the affinity measurement, the concentration of L-selectin LE-His in the cell culture supernatant was determined by a calibration free SPR method (calibration-free concentration analysis; CFCA; Fig. 3) (Christensen 1997, Richalet-Secordel et al. 1997, Sigmundsson et al. 2002) yielding a concentration of 200 ± 0.25 nM (SD from duplicate). Given a total volume of 150 ml and a molecular mass of 32,114 g/mol for the fully glycosylated protein, a total amount of 963 µg was found by CFCA which is in good agreement with 988 µg determined by the ELISA method. Purification via AAC was able to clean up to 4-fold the amount of protein compared to the optimized Ni-NTA procedure (Table 2).

affinity matrix	L-sel LE-His [µg] [a]	yield [%] [b]
Ni-NTA	167 ± 21	17
LD201mΔ1	608 ± 23	62

Table 2, affinity matrix performance. (a) amount of L-sel LE-His from cell culture supernatant bound to 1 eq. Ni-NTA or 1 eq. aptamer LD201mΔ1 (ELISA data) **(b)** yield calculated by the total amount of L-sel LE-His in 150 ml cell culture supernatant (988 ± 276 µg); ± SD from N=2 in duplicates
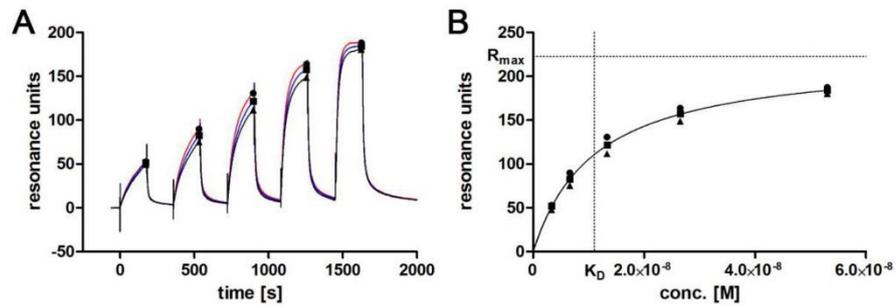
Figure 2, single cycle kinetics of L-selectin LE-His in cell culture supernatant. A: triplicate of the kinetic titration is shown. Symbols mark binding levels that will be plotted against the respective concentrations shown in B: binding levels are plotted against corresponding concentrations. Extrapolated R_{max} and respective K_D at $R_{max}/2$ are marked by dotted lines.
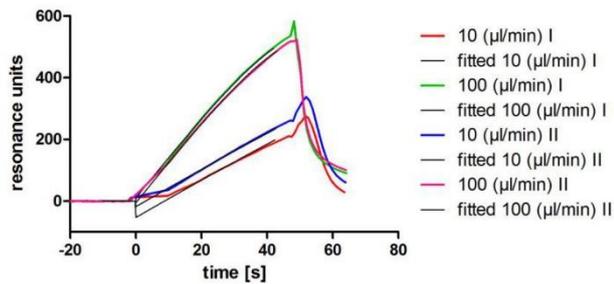
Figure 3, calibration free concentration analysis. L-selectin LE-His in cell culture supernatant was analyzed in duplicate. The sensorgrams (colored lines) and the fits (black lines) at the different flowrates are shown.

<u>Conclusion</u>

The shortened aptamer variant LD201mΔ1 shows binding comparable to the originally described aptamer (Hicke et al. 1996) that is specifically targeting the leukocyte adhesion receptor L-selectin with low nanomolar affinity. The successful application as a blocking agent of leukocyte adhesion (Riese et al. 2016) and the detachment of the protein from the aptamer by complexation of divalent cations with EDTA strongly suggests a binding mode that involves the Ca^{2+} binding lectin domain. Biotinylation of the DNA sequence at the 5´ end did not alter target recognition. Its high affinity and selectivity makes the synthetic ligand perfectly suitable to capture L-selectin from crude mixtures like cell culture supernatant. In contrast to standard affinity approaches for protein purification such as Ni-NTA, AAC does not rely on time consuming optimization procedures and the purified protein can be obtained in a single step in higher yields.

Literature

ACQUAH C, DANQUAH MK, YON JL, SIDHU A AND ONGKUDON CM. 2015. A review on immobilised aptamers for high throughput biomolecular detection and screening. Anal Chim Acta 888: 10-18.

CHRISTENSEN LL. 1997. Theoretical analysis of protein concentration determination using biosensor technology under conditions of partial mass transport limitation. Analytical biochemistry 249: 153-164.

HIANIK T, OSTATNA V, ZAJACOVA Z, STOIKOVA E AND EVTUGYN G. 2005. Detection of aptamer-protein interactions using QCM and electrochemical indicator methods. Bioorganic & medicinal chemistry letters 15: 291-295.

HICKE BJ ET AL. 1996. DNA aptamers block L-selectin function in vivo. Inhibition of human lymphocyte trafficking in SCID mice. The Journal of clinical investigation 98: 2688-2692.

KARLSSON R, KATSAMBA PS, NORDIN H, POL E AND MYSZKA DG. 2006. Analyzing a kinetic titration series using affinity biosensors. Analytical biochemistry 349: 136-147.

KEEFE AD, PAI S AND ELLINGTON A. 2010. Aptamers as therapeutics. Nature reviews Drug discovery 9: 537-550.

LEY K. 2003. The role of selectins in inflammation and disease. Trends in molecular medicine 9: 263-268.

LEY K, LAUDANNA C, CYBULSKY MI AND NOURSHARGH S. 2007. Getting to the site of inflammation: the leukocyte adhesion cascade updated. Nature reviews Immunology 7: 678-689.

MULLER WA. 2002. Leukocyte-endothelial cell interactions in the inflammatory response. Laboratory investigation; a journal of technical methods and pathology 82: 521-533.

RICHALET-SECORDEL PM, RAUFFER-BRUYERE N, CHRISTENSEN LL, OFENLOCH-HAEHNLE B, SEIDEL C AND VAN REGENMORTEL MH. 1997. Concentration measurement of unpurified proteins using biosensor technology under conditions of partial mass transport limitation. Analytical biochemistry 249: 165-173.

RIESE SB, BUSCHER K, ENDERS S, KUEHNE C, TAUBER R AND DERNEDDE J. 2016. Structural requirements of mono- and multivalent L-selectin blocking aptamers for enhanced receptor inhibition in vitro and in vivo. Nanomedicine : nanotechnology, biology, and medicine.

ROMIG TS, BELL C AND DROLET DW. 1999. Aptamer affinity chromatography: combinatorial chemistry applied to protein purification. Journal of chromatography B, Biomedical sciences and applications 731: 275-284.

SIGMUNDSSON K, MÁSSON G, RICE R, BEAUCHEMIN N AND ÖBRINK B. 2002. Determination of Active Concentrations and Association and Dissociation Rate Constants of Interacting Biomolecules: An Analytical Solution to the Theory for Kinetic and Mass Transport Limitations in Biosensor Technology and Its Experimental Verification†. Biochemistry 41: 8263-8276.

SPERANDIO M, PICKARD J, UNNIKRISHNAN S, ACTON ST AND LEY K. 2006. Analysis of Leukocyte Rolling In Vivo and In Vitro. 416: 346-371.

WEDEPOHL S, KAUP M, RIESE SB, BERGER M, DERNEDDE J, TAUBER R AND BLANCHARD V. 2010. N-glycan analysis of recombinant L-Selectin reveals sulfated GalNAc and GalNAc-GalNAc motifs. Journal of proteome research 9: 3403-3411.

3.4   Shell cleavable dendritic polyglycerol sulfates show high anti-inflammatory properties by inhibiting L-selectin binding and complement activation

Sabine Reimann, Dominic Groeger, Christian Kuehne, Sebastian B. Riese, Jens Dernedde, Rainer Haag

Zu dieser Veröffentlichung hat der Autor mit der Durchführung und Auswertung der SPR Bindungsstudien, der Evaluation der Biokompatibilität und der Erstellung von Teilen des Manuskripts beigetragen.

Reimann, S., D. Gröger, C. Kühne, S. B. Riese, J. Dernedde and R. Haag (2015) Shell Cleavable Dendritic Polyglycerol Sulfates Show High Anti-Inflammatory Properties by Inhibiting L-Selectin Binding and Complement Activation. *Advanced healthcare materials*. **4**, 2154-2162.

Shell cleavable dendritic polyglycerol sulfates show high anti-inflammatory properties by inhibiting L-selectin binding and complement activation

3.5 Detecting and quantifying biomolecular interactions of a dendritic polyglycerol sulfate nanoparticle using fluorescence lifetime measurements

Alexander Boreham, Jens Pikkemaat, Pierre Volz, Robert Brodwolf, Christian Kuehne, Kai Licha, Rainer Haag, Jens Dernedde, Ulrike Alexiev

Zu dieser Veröffentlichung hat der Autor mit der Durchführung und Auswertung der SPR Bindungsstudien und der Erstellung von Teilen des Manuskripts beigetragen.

Boreham, A., J. Pikkemaat, P. Volz, R. Brodwolf, C. Kuehne, K. Licha, R. Haag, J. Dernedde and U. Alexiev (2015) Detecting and Quantifying Biomolecular Interactions of a Dendritic Polyglycerol Sulfate Nanoparticle Using Fluorescence Lifetime Measurements. *Molecules*. **21**, E22.

molecules

MDPI

Article

Detecting and Quantifying Biomolecular Interactions of a Dendritic Polyglycerol Sulfate Nanoparticle Using Fluorescence Lifetime Measurements

Alexander Boreham [1]**, Jens Pikkemaat** [1]**, Pierre Volz** [1]**, Robert Brodwolf** [1,2]**, Christian Kuehne** [3]**, Kai Licha** [4]**, Rainer Haag** [2,5]**, Jens Dernedde** [2,3] **and Ulrike Alexiev** [1,2,*]

[1]   Institut für Experimentalphysik, Freie Universität Berlin, Arnimallee 14, 14195 Berlin, Germany; alexander.boreham@fu-berlin.de (A.B.); jpikkemaat@zedat.fu-berlin.de (J.P.); pierre.volz@fu-berlin.de (P.V.); brodwolf@zedat.fu-berlin.de (R.B.)
[2]   Helmholtz Virtual Institute—Multifunctional Biomaterials for Medicine, Helmholtz-Zentrum Geesthacht, Kantstr. 55, 14513 Teltow, Germany; haag@chemie.fu-berlin.de (R.H.); jens.dernedde@charite.de (J.D.)
[3]   Institut für Laboratoriumsmedizin, Klinische Chemie und Pathobiochemie, Charité—Universitätsmedizin Berlin, Augustenburger Platz 1, 13353 Berlin, Germany; christian.Kuehne@charite.de
[4]   Mivenion GmbH, Robert-Koch-Platz 4, 10115 Berlin, Germany; Licha@mivenion.com
[5]   Institut für Chemie und Biochemie, Freie Universität Berlin, Takustrasse 3, 14195 Berlin, Germany
*   Correspondence: ulrike.alexiev@fu-berlin.de; Tel.: +49-30-838-55157; Fax: +49-30-838-56510

Abstract: Interactions of nanoparticles with biomaterials determine the biological activity that is key for the physiological response. Dendritic polyglycerol sulfates (dPGS) were found recently to act as an inhibitor of inflammation by blocking selectins. Systemic application of dPGS would present this nanoparticle to various biological molecules that rapidly adsorb to the nanoparticle surface or lead to adsorption of the nanoparticle to cellular structures such as lipid membranes. In the past, fluorescence lifetime measurements of fluorescently tagged nanoparticles at a molecular and cellular/tissue level have been proven to reveal valuable information on the local nanoparticle environment via characteristic fluorescent lifetime signatures of the nanoparticle bound dye. Here, we established fluorescence lifetime measurements as a tool to determine the binding affinity to fluorescently tagged dPGS (dPGS-ICC; ICC: indocarbocyanine). The binding to a cell adhesion molecule (L-selectin) and a human complement protein (C1q) to dPGS-ICC was evaluated by the concentration dependent change in the unique fluorescence lifetime signature of dPGS-ICC. The apparent binding affinity was found to be in the nanomolar range for both proteins (L-selectin: 87 ± 4 nM and C1q: 42 ± 12 nM). Furthermore, the effect of human serum on the unique fluorescence lifetime signature of dPGS-ICC was measured and found to be different from the interactions with the two proteins and lipid membranes. A comparison between the unique lifetime signatures of dPGS-ICC in different biological environments shows that fluorescence lifetime measurements of unique dPGS-ICC fluorescence lifetime signatures are a versatile tool to probe the microenvironment of dPGS in cells and tissue.

Keywords: nanomedicine; dendritic polymers; protein corona; fluorescence lifetime

1. Introduction

The molecular basis of nanoparticle interactions with cells and tissue can only be understood with precise knowledge of molecular properties of the nanoparticle. This characterization is of paramount importance, especially with regard to the targeted delivery of drugs or the physiological

action of the nanoparticle itself. New and different analytical methods have to be established to meet the needs of the rapidly growing field of nanomedicine [1–4].

Important properties of dendrimeric nanoparticles like dendritic polyglycerol sulfates (dPGS) [5–10] include the size, shape and flexibility of the nanoparticle [11]. In a recent report we showed that both size and conformational flexibility of dPGS depend on temperature [1]. The fluorescent indocarbocyanine (ICC) (Figure 1) tag proved to be an efficient sensor for environmental properties as shown by the different fluorescence lifetimes in a systematic study of dPGS-ICC in different aqueous and organic solvents [1]. In addition to being dependent on the polarity [3], the fluorescence lifetime of the ICC dye is also sensitive to steric restrictions (Figure 1). In aqueous environments the ICC methine linker can rotate freely, leading to the short fluorescence lifetime of about 0.15 ns of the fluorophore. Steric hindrance of the ICC methine linker results in longer lifetimes [1–3,12]. A longer lifetime component of about 1 ns was observed for ICC bound to dPGS [2] (Figure 1A, Table 1). Upon binding of dPGS-ICC to lipid membranes an additional 4 ns component becomes apparent [1] (Figure 1A).
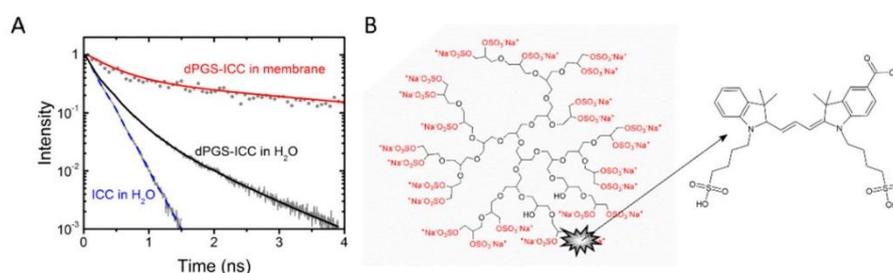
Figure 1. Structure and fluorescence lifetime characteristics of dPGS-ICC. (**A**) Fluorescence lifetime curves of ICC and dPGS-ICC in water and bound to DMPC lipid membranes; and (**B**) structural scheme of dPGS and the bound fluorescent tag ICC. A detailed description of the conjugation procedure is given by Licha *et al.* [13].

Upon administration of dPGS, the nanoparticle would interact with proteins of the blood serum or constituents of biological membranes (e.g., proteins and/or lipids). Interaction of nanoparticles with proteins is known as the "protein corona" [4,14] that determines the biological activity of the respective nanoparticle, because proteins compete with the target structures for the nanoparticle surface [15,16]. In the past several different methods were implemented to study the equilibrium and kinetic parameters of protein-nanoparticle interactions such as isothermal titration calorimetry (ITC), gel filtration, size-exclusion chromatography, surface plasmon resonance (SPR), or centrifugation based pull-down assays [4]. We recently established time-resolved fluorescence spectroscopy and fluorescence lifetime imaging microscopy (FLIM) as a versatile tool to analyze nanoparticle interactions at the molecular and cell/tissue level [1–3].

Here, we extended our previous fluorescence lifetime studies on dPGS-ICC to nanoparticle-protein interactions using L-selectin and the complement protein C1q as well as human serum. We show that fluorescence lifetime methods are well suited to detect the "protein corona" and to quantify binding affinities of individual proteins. Moreover, we show that different biomolecules display different fluorescence decay parameters underscoring our concept of using unique fluorescence lifetimes as target signatures in FLIM-based analyses of nanoparticle interactions in cells and tissue.

2. Results and Discussion

2.1. Determination of Apparent Protein Binding Constants for dPGS-ICC

2.1.1. Binding of L-Selectin

We investigated fluorescence lifetime spectroscopy as a tool to determine affinity of protein–dPGS-ICC interaction. Multivalent dPGS is known to efficiently bind L- and P-selectin [6,7,9,10]. L-selectin is one of the natural cell adhesion molecules on leukocytes that in chronic inflammation processes extravasate into inflamed tissue by interactions of L-, E-, and P- selectins and their corresponding ligands consisting of fucosylated and sialylated glycoproteins on the endothelium.

First, soluble L-selectin (L-selectin-IgG chimera) was titrated in three different concentrations into a solution of 0.1 μM dPGS to evaluate whether a change in the fluorescence lifetime curve occurs. As this was the case we titrated 11 different concentrations into the dPGS-ICC solution until no change in the fluorescence lifetime curve was observable (Figure 2).
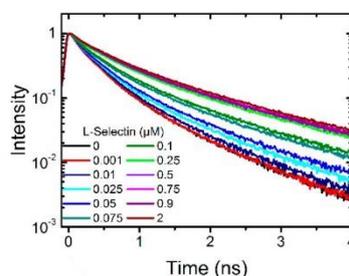
Figure 2. Fluorescence lifetime curves of 0.1 μM dPGS-ICC alone and with 11 different concentrations of soluble L-selectin-IgG chimera (0.001 μM to 2 μM) in DPBS at 20 °C.

The fluorescence decay curves were fitted with a multi-exponential decay function and the mean fluorescence lifetime was determined. The time-resolved fluorescence method belongs to the indirect methods to determine a binding constant. The assumption is made that the measured fluorescence lifetime (or better the change upon binding) is directly proportional to the concentration of the nanoparticle-bound protein, assuming that the protein exists only in two states, in the nanoparticle bound and in the free state, each state having its own unique fluorescence lifetime characteristics.
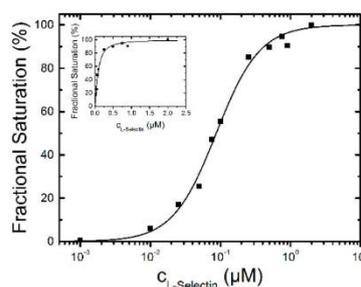
Figure 3. L-selectin-binding curve to 0.1 μM dPGS-ICC in DPBS at 20 °C. The concentrations are plotted on a logarithmic scale. The inset shows the data on a linear scale. The half maximum binding concentration was determined to be 87 ± 4 nM with a Hill-coefficient of $n = 1.4$.

To analyze the binding affinity, the difference between the mean fluorescence lifetime at 0 µM L-selectin and the mean fluorescence lifetimes at different L-selectin concentrations was calculated. The lifetime difference at 2 µM L-selectin constitutes the value at saturation of the binding reaction and was set as 100%. To determine the binding affinity the fractional saturation values (lifetime differences in %) were plotted *vs.* the concentration of L-selectin and fitted by a sigmoidal function (Figure 3). The half-maximum concentration of L-selectin binding was determined to 87 ± 4 nM with a Hill coefficient of n = 1.4 indicating a binding stoichiometry of about 1:1. The fluorescence decay time constants of the saturated lifetime signal are summarized in Table 1.

2.1.2. Binding of C1q

Second, the complement protein C1q is the first protein that binds to immobilized antibodies and activates the classical pathway. In addition to its beneficial role in foreign antigen targeting, C1q plays an important role in autoimmune diseases and triggers inflammation. To study the interaction with dendritic polyglycerol sulfate C1q was titrated to a solution of 0.1 µM dPGS to evaluate whether a change in the fluorescence lifetime curve occurs. This was the case and we titrated eight different concentrations into the dPGS-ICC solution (Figure 4).
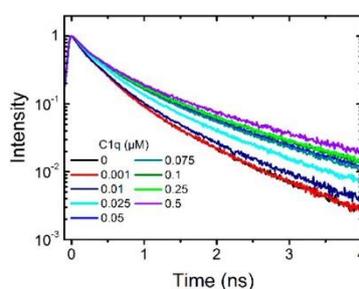

Figure 4. Fluorescence lifetime curves of 0.1 µM dPGS-ICC alone and with eight different concentrations of the complement protein C1q (0.001 µM to 0.5 µM) in DPBS at 20 °C.

Using the fractional saturation method the apparent binding affinity was determined to be 42 ± 12 nM for C1q (Figure 5). The Hill coefficient was n = 1.1 indicating also for C1q a 1:1 binding stoichiometry. The fluorescence decay time constants of the saturated lifetime signal are summarized in Table 1.
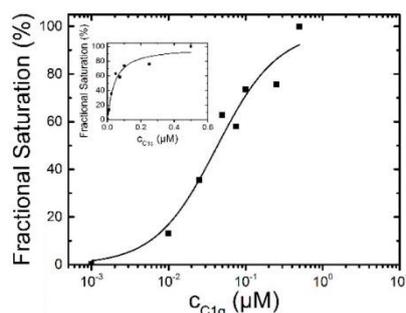
Figure 5. C1q- binding curve to 0.1 µM dPGS-ICC in DPBS at 20 °C. The half maximum binding concentration was determined to be 42 ± 12 nM and n = 1.1.

2.1.3. Binding of Human Serum

Next we tested at which concentration (in %) human serum with a protein content of 53 mg/mL results in a saturation of the fluorescence lifetime signal. Figure 6A shows the fluorescence lifetime curves of dPGS-ICC with 0%, 10%, 30%, 50%, and 70% serum concentration. These data clearly show that already at about 10% serum concentration (equivalent to a 5.3 mg/mL solution) the saturation fluorescence signal is reached. The fluorescence decay time constants of the saturated lifetime signal are summarized in Table 1.

To determine the binding affinity of human serum constituents to dPGS we titrated human serum at different concentrations between 0.001% and 10% serum (Figure 6B). Using the fractional saturation method, the mean fluorescence lifetime derived data were plotted in percent as a function of human serum concentration in Figure 6C,D. Analysis of the binding curve gives a mean apparent binding affinity corresponding to 0.3% serum (with a Hill coefficient $n = 1$). In contrast to the plots shown in Figures 3 and 5 the sigmoidal fit (Figure 6D) does not completely fit the data. This is understandable as the serum consists of a mixture of different proteins which could bind with different affinities. We thus added a second component to the fit and the resulting apparent binding affinities (half maximum binding concentration) were 0.2% serum (78% amplitude) and 5% serum (22% amplitude). Even though there are more than two different proteins in the human serum, the fit considerably improves. We conclude that dPGS has the potential to bind different protein species with varying binding affinity. This is an important result as it provides a rationale that, despite its protein corona, dPGS recognizes L-selectin in living tissue [6].
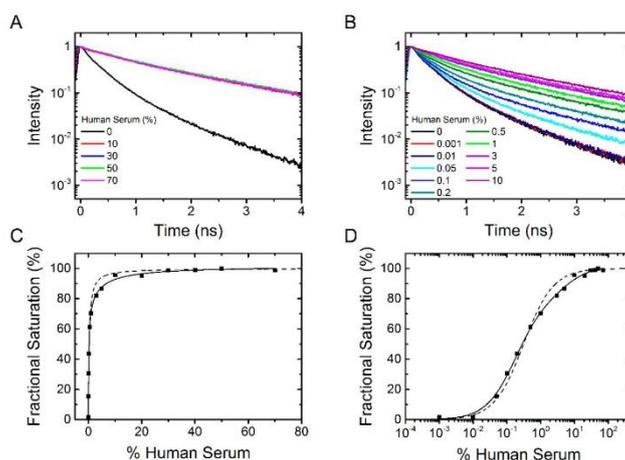

Figure 6. dPGS-ICC binding to human serum. (**A**) Fluorescence lifetime curves of 0.1 μM dPGS-ICC alone and with 10%, 30%, 50%, and 70% human serum in DPBS at 20 °C; (**B**) Fluorescence decay curves for titration of dPGS-ICC with human serum at different concentrations between 0.001% and 10% serum; (**C,D**) Fractional saturation as a function of human serum concentration both linear (**C**) and with a logarithmic *x*-axis (**D**). The half maximum binding concentration was determined to be 0.3% human serum (using a Hill-coefficient of $n = 1$) for a single component fit and 0.2% and 5% for a double component fit.

2.1.4. SPR Measurements of Protein Association

L-selectin binding to dPGS was also investigated by surface plasmon resonance (SPR). The dPGS was immobilized on a chip and the defined concentrations of the analytes L-selectin and C1q were passed over the functionalized surface. Binding affinity was determined from resulting

binding isotherms (Figure 7) and gave values of 45 ± 17 nM for L-selectin and 62 ± 10 nM for C1q. These complementary experiments prove that binding of L-selectin and C1q to dPGS determined by either analysis of fluorescence decay curves or SPR revealed comparable affinities in the lower nanomolar range.
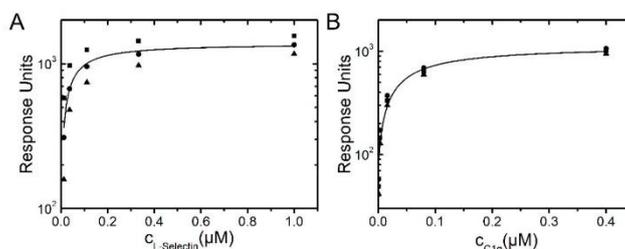
Figure 7. Langmuir binding isotherms of L-selectin (**A**) and C1q (**B**) to dPGS.

2.2. Determination of Protein Binding Kinetics to dPGS-ICC

2.2.1. Binding Kinetics of Human Serum

Binding kinetics measurements offer an additional approach to evaluate protein association. We first tested the binding kinetics of different concentrations of human serum. We choose two concentrations, near the half maximum binding concentration (0.5% serum, Figure 8A) and a concentration that leads to saturation of the fluorescence lifetime signal (10% serum, Figure 8B). Figure 8C shows the binding curves. As expected from the fractional binding signal (Figure 6), the kinetics is faster for 10% serum (34 ± 3 s) than for 0.5% serum (77 ± 4 s).
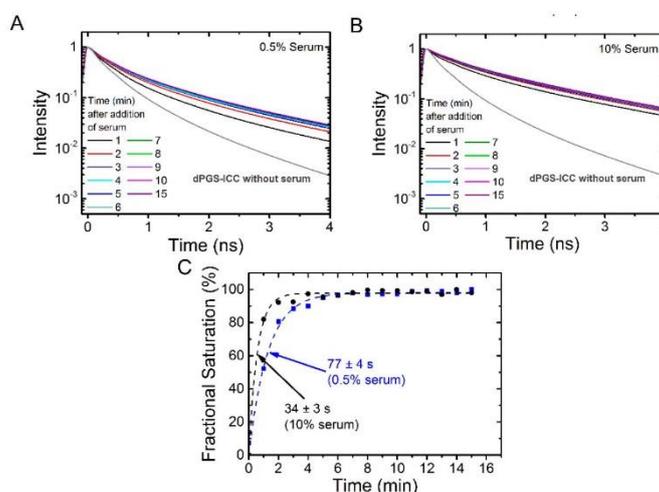
Figure 8. Kinetics of dPGS-ICC binding in human serum. Lifetime decay curves in (**A**) 0.5% serum and (**B**) in 10% human serum at different time points are shown; (**C**) Fractional saturation, based on the mean fluorescence lifetimes, as a function of time. The dashed lines indicate an exponential fit to the data and the time constant τ was 34 s for 10% serum and 77 s for 0.5% serum.

Detecting and quantifying biomolecular interactions of a dendritic polyglycerol sulfate nanoparticle using fluorescence lifetime measurements

2.2.2. Binding Kinetics of L-Selectin

Next, we determined the binding kinetics of L-selectin (Figure 9A,B). At the saturation concentration of 1 µM, L-selectin binds very fast with a time constant of 26 ± 1 s. This is in the same range as the binding time constant of 10% serum (Figure 8). Subsequent addition of 10% serum to L-selectin saturated dPGS-ICC leads to further increase of the fluorescence lifetime (Figure 9C). Evaluation of the kinetics of serum binding to L-selectin saturated dPGS-ICC reveals a bi-exponential binding kinetics with time constants of 24 ± 3 s (30% amplitude) and 242 ± 36 s (70% amplitude). This is in contrast to the monoexponential binding kinetics with a time constant of 34 s observed for 10% serum alone. Clearly, L-selectin competes with the binding of other serum proteins. A comparison of the unique lifetime signatures of dPGS-ICC with 10% serum and dPGS with L-selectin/10% serum shows subtle but clear differences that indicate the presence of dPGS bound L-selectin under saturating binding concentrations of human blood serum. This result supports our conclusion from the previous section that dPGS recognizes L-selectin despite the presence of other competing proteins in blood plasma.
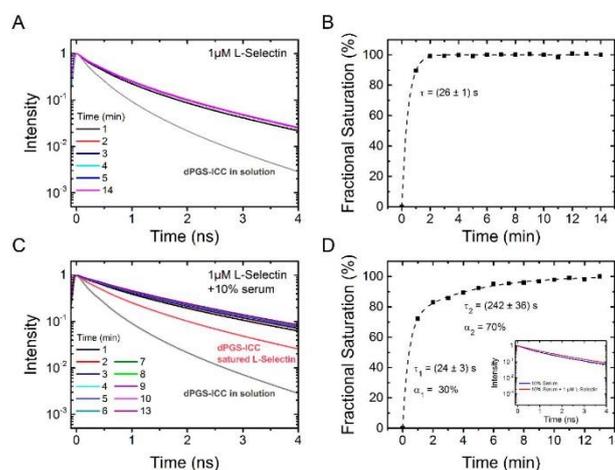
Figure 9. Time dependence of dPGS-ICC binding to L-selectin and effect of serum. (**A**) Lifetime decay curves of 0.1 µM dPGS-ICC binding to 1 µM L-selectin and (**B**) the fractional saturation, based on the mean fluorescence lifetimes, as a function of time. The value of $\tau = 26$ s was obtained from an exponential fit to the data (dashed line); (**C**) Lifetime decay curves of 0.1 µM dPGS-ICC binding to 1 µM L-selectin upon addition of human serum (final concentration: 10% serum) and (**D**) the fractional saturation, based on the mean fluorescence lifetimes, as a function of time. A bi-exponential fit to the data (dashed line) yielded two time constants of $\tau_1 = 24$ s and $\tau_2 = 242$ s with amplitudes of 30% and 70% respectively. Inset: fluorescence lifetime curves of dPGS-ICC in 10% serum and in 10% serum with 1 µM L-selectin.

Table 1. Fluorescence lifetime parameters for different dPGS-ICC interaction partners according to Equation (1). The mean fluorescence lifetime (Equation (2)) and the reduced X^2 is given.

Sample	α_1 (%)	τ_1 (ns)	α_2 (%)	τ_2 (ns)	α_3 (%)	τ_3 (ns)	τ_{mean} (ns)	X^2_R
0.1 µM dPGS-ICC	5.7	1.16	30.7	0.47	63.6	0.17	0.51	1.05
+ 0.5 µM C1q	11.2	1.85	31.3	0.67	57.5	0.18	1.04	0.95
+ 1 µM L-selectin	17.4	1.75	40.5	0.65	42.1	0.19	1.11	1.01
+ 1 µM L-selectin + 10% Serum	37.1	2.24	39.5	0.90	23.4	0.19	1.78	0.91
+ 70% Serum	39.2	2.27	35.1	0.85	25.7	0.14	1.87	0.98

3. Materials and Methods

3.1. Time-Resolved Fluorescence Setup

All measurements were performed on a time-resolved fluorescence setup [17–19] with a tunable white light laser source (SuperK Extreme EUV3, NKT, Birkerød, Denmark), a microchannel plate detector and time-correlated single photon counting (TCSPC) electronics (SPC-830, Becker & Hickl GmbH, Berlin, Germany) with picosecond time resolution. The excitation of ICC at 530 nm was selected via an acousto-optical tunable filter (SELECT UV-VIS, NKT, Birkerød, Denmark). Fluorescence emission was collected above 545 nm using a long-pass filter (HQ545 LP, Chroma, Bellows Falls, VT, USA). The excitation power was 220 µW and the repetition rate was 19.5 MHz. The time range was set to 10 ns divided into 1024 channels resulting in a resolution of 9.8 ps/channel. The instrument response function of the system was ~54 ps full width at half maximum.

3.2. Experimental Procedures

3.2.1. Dendritic Polyglycerol Sulfate Nanocarrier Labeled with a Fluorescent ICC Dye (dPGS-ICC)

Dendritic polyglycerolsulfate (dPGS) with a molecular weight of approx. 12,000 g/mol was synthesized according to literature via an anionic multi-branching ring-opening polymerization of glycidol and sulfation using sulfurtrioxide-pyridinium complex [20]. A detailed description of the dye conjugation procedure is given by Licha *et al.* [13]. Briefly, to attach ICC to dPGS, an azido-linker (linker 11-azido-1-undecanyl-tosylate) was conjugated to the polyglycerol scaffold at a molar ratio of approximately one linker per polymer before sulfation. After sulfation, the azido-containing polymer was conjugated with a propargyl derivative of ICC by copper-catalyzed 1,3-dipolar cycloaddition (click conjugation) in water/ethanol. After synthesis, the dPGS-ICC was lyophilized. All experiments were conducted with a freshly prepared dPGS-ICC sample from the lyophilisate of the same batch.

3.2.2. Determination of Apparent Protein Binding Constants for dPGS-ICC

To determine the apparent protein binding constants for dPGS-ICC, samples containing 0.1 µM dPGS-ICC and varying concentrations of either L-selectin (L-selectin-IgG chimera, R & D Systems, Wiesbaden, Germany) or C1q (Fitzgerald Industries International, Acton, MA, USA) were prepared in DPBS buffer (PAA; 10 mM phosphate, 1 mM calcium, 1 mM magnesium, 3 mM KCl, 137 mM NaCl, pH 7.4). The measurements were conducted after incubating 0.1 µM dPGS-ICC and the different protein concentrations for 2 min at room temperature. In addition the binding behavior of dPGS-ICC in human serum was analyzed. Here, fluorescence lifetime measurements were conducted after incubating 0.1 µM dPGS-ICC and different concentrations of serum for 5 min at room temperature. The fluorescence decay was recorded for 180 s.

3.2.3. Determination of Protein Binding Kinetics to dPGS-ICC

To determine the kinetics of dPGS-ICC binding in human serum, a buffer solution containing dPGS-ICC was prepared. Directly before the start of the measurement human serum was added to either 10% or 0.5% final concentration. The concentration of dPGS-ICC in the final volume was 0.1 µM in both cases. The fluorescence decay was recorded over a time period of 15 min, with a duration of 60 s for each individual recording.

3.2.4. Determination of Protein Exchange

To determine the influence of human serum on preincubated L-selectin, first the kinetics of dPGS-ICC binding to L-selectin were determined and then the effect of human serum addition was followed. A buffer solution containing dPGS-ICC was prepared. Directly before the start of the measurement L-selectin was added at a concentration of 1 µM. The concentration of dPGS-ICC in the final volume was 0.1 µM. The fluorescence decay was recorded over a time period of 14 min, with a

duration of 60 s for each individual recording. Then, human serum was added, final concentration 10%, and further measurements were conducted for the next 13 min, again with a duration of 60 s for each individual recording.

3.2.5. SPR Measurements of Protein Association

Experiments were carried out on a Biacore X100 device (GE Healthcare, Freiburg, Germany). A streptavidin coated chip (SA-Chip, GE Healthcare) was coupled with dPGS-biotin to a level of ~400 resonance units (RU) in HBS-Ca (10mM HEPES pH 7.4 + 150 mM NaCl + 1 mM CaCl$_2$) as a running buffer using standard procedures. Briefly, the chip was conditioned using three consecutive injections of 60 s 1 M NaCl + 50 mM NaOH before injection of dPGS-biotin and washing with three consecutive injections of running buffer. Affinities were measured using a kinetic titration series (single cycle kinetics) at 25 °C in which five ascending concentrations of the analyte (C1q or L-Sel-IgG chimera) were injected consecutively for 120 s at 30 µL/min followed by a dissociation time of 600 s and one regeneration step with 4 M MgCl$_2$ for 120 s. L-selectin was diluted in HBS-Ca to final concentrations of 1000, 333, 111, 37, and 12.34 nM; C1q in surfactant P20 supplemented (+0.005%) running buffer (HBSP) at concentrations of 400, 80, 16, 3.2, and 0.64 nM. The signal of the untreated flow cell was subtracted from the binding signal. Additionally, blank injects of running buffer only were also subtracted (double referencing) for each run. Sensorgrams were analyzed by plotting the analyte concentration against the binding signal at the end of inject. The resulting isotherm was fitted using the steady state model.

3.3. Data Analysis

3.3.1. Determination of Fluorescence Decay Parameters

The fluorescence decay profiles were analyzed using the software package Globals Unlimited V2.2 (Laboratory for Fluorescence Dynamics). An algorithm based on a Marquardt–Levenberg type of nonlinear least-squares analysis was used. The time course of the fluorescence was fitted with a sum of exponentials:

$$I(t) = \sum_i a_i * \exp\left(-\frac{t}{\tau_i}\right) \tag{1}$$

where a_i are the amplitudes and τ_i are the lifetimes of the ith decay component. α_i are the corresponding relative amplitudes, with $\alpha_i = a_i / \sum a_i$ [17,21].

3.3.2. Determination of Apparent Binding Constants

To determine the apparent binding constants of dPGS-ICC, the mean lifetime of the respective fluorescence decay curves was calculated as follows:

$$\tau_{mean} = \sum_i \tau_i * \left(\frac{\alpha_i * \tau_i}{\sum_i \alpha_i * \tau_i}\right) \tag{2}$$

where α_i are the relative amplitudes and τ_i are the lifetimes of the ith decay component.

The fractional saturation (in %) was determined as follows:

$$fractional\ saturation\ (\%) = \left(\frac{\tau_{mean} - \tau_0}{\tau_{max}}\right) * 100 \tag{3}$$

where τ_{mean} is the mean lifetime of the respective lifetime decay curve, τ_0 is the mean lifetime of the lifetime decay curve of dPGS-ICC in solution, and τ_{max} is the highest mean lifetime.

The resulting data points were then fit according to the model function

$$y(x) = \frac{S * x^n}{(K_{50}{}^n + x^n)} \tag{4}$$

where S is the saturation of binding, K_{50} is the half maximum binding concentration (apparent binding affinity), and the Hill-coefficient n, a cooperativity factor.

3.3.3. Determination of Protein Binding Kinetics to dPGS-ICC

To determine the binding kinetics of dPGS-ICC, the mean lifetime of the respective fluorescence decay curves was calculated as described in Equation (2) and the fractional saturation (in %) was calculated according to Equation (3). The kinetic data was then fit with an exponential model function.

$$y(t) = A * e^{\frac{t}{\tau}} \tag{5}$$

3.3.4. Determination of Protein Exchange

The binding kinetics of dPGS-ICC to L-selectin were determined as described in 3.3.2. To evaluate the kinetics of serum addition the fractional saturation (in %) was determined using Equation (3), however with τ_0 the mean lifetime of the lifetime decay curve of dPGS-ICC bound to L-selectin. The kinetic data required a fit with a biexponential model function according to:

$$y(t) = A_1 * e^{\frac{t}{\tau_1}} + A_2 * e^{\frac{t}{\tau_2}} \tag{6}$$

4. Conclusions

dPGS is a multivalent dendritic negatively-charged nanoparticle whose binding affinities are largely determined by electrostatic interactions. For example binding to L-selectin occurs via a patch of basic amino acid residues in the lectin binding domain [22]. However, other proteins including membrane proteins very often feature charged patches that may also undergo transient changes upon protein function [23–25]. Thus it is very likely that in a physiological environment a plethora of dPGS binding partners exists. Here, a comparison of the lifetime signatures of dPGS-ICC with different proteins present in human serum and cellular membranes, like C1q and L-selectin, respectively, shows clear differences (Figure 10).
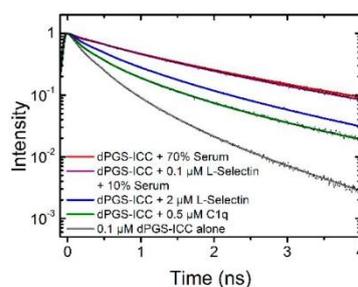

Figure 10. Lifetime signatures of dPGS-ICC with different proteins and human serum.

Previously-published data on dPGS-ICC showed that the two fastest decay components reflect on the polarity of the ICC environment while the slowest component is due to steric hindrance of the methine linker rotation caused by the PG branches [1]. Here, we observed that both the slowest

component and the intermediate component show slower lifetime values upon dPGS-ICC binding to the proteins L-selectin and C1q but also in the presence of human serum, with the exact values depending on the specific protein. This clearly indicates that the binding of dPGS-ICC to the proteins L-selectin and C1q, but also to binding partners in human serum, changes both the polarity of the immediate dPGS-ICC environment and also the steric hindrance for the rotation of the ICC methine linker in a protein dependent fashion.

The measurements presented in this paper were performed in solution. However, fluorescence lifetime can also be recorded in a spatial resolved fashion on cells and tissues under a microscope, *i.e.*, with fluorescence lifetime imaging microscopy (FLIM). The use of FLIM is known to include environmental sensing of, amongst others, polarity, local pH, and calcium concentrations, as well as the study of protein interactions in living cells [26]. The results provided in this study show that the fluorescence lifetime also allows for the environmental sensing of biomolecular interactions with dPGS, as unique dPGS-ICC lifetimes exist depending on the dPGS binding partner (Figure 10). Thus, we now extend our concept of using unique fluorescence lifetime signatures for fast and reliable localization of fluorescently labeled nanoparticles in cellular systems and tissue samples [2,27–30] to the potential detection of biomolecular interactions of dPGS in physiological environments. The results presented allow for the possibility of specifically determining the dPGS interaction partners based on the specific fluorescence signature. Further, this methodology is not necessarily limited to dPGS, as in theory any nanoparticle with a fluorescent reporter group can be used, as long as the environmental sensitivity is high enough. However, the use of ICC, as in this study, offers the additional benefit of being sensitive to the steric hindrance of the dye upon nanoparticle-biomolecule interactions. This concept will be developed further in future experiments.

Author Contributions: A.B. performed fluorescence experiments, analyzed and interpreted the data, and contributed to the writing of the manuscript, J.P. contributed to the fluorescence experiments and data analysis, P.V. contributed to the fluorescence experiments and data analysis, R.B. contributed to the data analysis, C.K. contributed to the SPR experiments and data analysis, K.L. synthesized the fluorescently labeled dPGS-ICC nanoparticle used in the study, R.H. contributed to experiment design, J.D. contributed to experiment design, data interpretation and writing of the manuscript, U.A. designed the experiments, analyzed and interpreted the data and wrote the manuscript.

Conflicts of Interest: The authors declare no conflict of interest.

Abbreviations

The following abbreviations are used in this manuscript:

dPGS	Dendritic polyglycerol sulfate
dPGS-ICC	Indocarbocyanine bound to dendritic polyglycerol sulfate
ICC	Indocarbocyanine
DMPC	Dimyrostoylphosphatidylcholine
ITC	Isothermal titration calorimetry
FLIM	Fluorescence lifetime imaging microscopy
TCSPC	Time-correlated single photon counting
IgG	Immunglobulin G
RU	Resonance units
SPR	Surface plasmon resonance

References

1. Boreham, A.; Brodwolf, R.; Pfaff, M.; Kim, T.-Y.; Schlieter, T.; Mundhenk, L.; Gruber, A.D.; Gröger, D.; Licha, K.; Haag, R.; Alexiev, U. Temperature and environment dependent dynamic properties of a dendritic polyglycerol sulfate. *Polym. Adv. Technol.* **2014**, *25*, 1329–1336. [CrossRef]
2. Boreham, A.; Kim, T.Y.; Spahn, V.; Stein, C.; Mundhenk, L.; Gruber, A.D.; Haag, R.; Welker, P.; Licha, K.; Alexiev, U. Exploiting fluorescence lifetime plasticity in flim: Target molecule localization in cells and tissues. *ACS Med. Chem. Lett.* **2011**, *2*, 724–728. [CrossRef] [PubMed]
3. Boreham, A.; Pfaff, M.; Fleige, E.; Haag, R.; Alexiev, U. Nanodynamics of dendritic core-multishell nanocarriers. *Langmuir* **2014**, *30*, 1686–1695. [CrossRef] [PubMed]
4. Cedervall, T.; Lynch, I.; Lindman, S.; Berggard, T.; Thulin, E.; Nilsson, H.; Dawson, K.A.; Linse, S. Understanding the nanoparticle-protein corona using methods to quantify exchange rates and affinities of proteins for nanoparticles. *Proc. Natl. Acad. Sci. USA* **2007**, *104*, 2050–2055. [CrossRef] [PubMed]
5. Calderon, M.; Quadir, M.A.; Sharma, S.K.; Haag, R. Dendritic polyglycerols for biomedical applications. *Adv. Mater.* **2010**, *22*, 190–218. [CrossRef] [PubMed]
6. Dernedde, J.; Rausch, A.; Weinhart, M.; Enders, S.; Tauber, R.; Licha, K.; Schirner, M.; Zügel, U.; von Bonin, A.; Haag, R. Dendritic polyglycerol sulfates as multivalent inhibitors of inflammation. *Proc. Natl. Acad. Sci. USA* **2010**, *107*, 19679–19684. [CrossRef] [PubMed]
7. Paulus, F.; Schulze, R.; Steinhilber, D.; Zieringer, M.; Steinke, I.; Welker, P.; Licha, K.; Wedepohl, S.; Dernedde, J.; Haag, R. The effect of polyglycerol sulfate branching on inflammatory processes. *Macromol. Biosci.* **2014**, *14*, 643–654. [CrossRef] [PubMed]
8. Quadir, M.A.; Haag, R. Biofunctional nanosystems based on dendritic polymers. *J. Control. Release* **2012**, *161*, 484–495. [PubMed]
9. Weinhart, M.; Gröger, D.; Enders, S.; Dernedde, J.; Haag, R. Synthesis of dendritic polyglycerol anions and their efficiency toward L-selectin inhibition. *Biomacromolecules* **2011**, *12*, 2502–2511. [CrossRef] [PubMed]
10. Weinhart, M.; Gröger, D.; Enders, S.; Riese, S.B.; Dernedde, J.; Kainthan, R.K.; Brooks, D.E.; Haag, R. The role of dimension in multivalent binding events: Structure-activity relationship of dendritic polyglycerol sulfate binding to L-selectin in correlation with size and surface charge density. *Macromol. Biosci.* **2011**, *11*, 1088–1098. [CrossRef] [PubMed]
11. Kannan, R.M.; Nance, E.; Kannan, S.; Tomalia, D.A. Emerging concepts in dendrimer-based nanomedicine: From design principles to clinical applications. *J. Intern. Med.* **2014**, *276*, 579–617. [CrossRef] [PubMed]
12. Chibisov, A.K.; Zakharova, G.V.; Gorner, H.; Sogulyaev, Y.A.; Mushkalo, I.L.; Tolmachev, A.I. Photorelaxation processes in covalently-linked indocarbocyanine and thiacarbocyanine dyes. *J. Phys. Chem.* **1995**, *99*, 886–893. [CrossRef]
13. Licha, K.; Welker, P.; Weinhart, M.; Wegner, N.; Kern, S.; Reichert, S.; Gemeinhardt, I.; Weissbach, C.; Ebert, B.; Haag, R.; Schirner, M. Fluorescence imaging with multifunctional polyglycerol sulfates: Novel polymeric near-IR probes targeting inflammation. *Bioconjugate Chem.* **2011**, *22*, 2453–2460. [CrossRef] [PubMed]
14. Monopoli, M.P.; Aberg, C.; Salvati, A.; Dawson, K.A. Biomolecular coronas provide the biological identity of nanosized materials. *Nat. Nanotechnol.* **2012**, *7*, 779–786. [CrossRef] [PubMed]
15. Walkey, C.D.; Chan, W.C. Understanding and controlling the interaction of nanomaterials with proteins in a physiological environment. *Chem. Soc. Rev.* **2012**, *41*, 2780–2799. [CrossRef] [PubMed]
16. Mu, Q.; Jiang, G.; Chen, L.; Zhou, H.; Fourches, D.; Tropsha, A.; Yan, B. Chemical basis of interactions between engineered nanoparticles and biological systems. *Chem. Rev.* **2014**, *114*, 7740–7781. [CrossRef] [PubMed]
17. Alexiev, U.; Rimke, I.; Pöhlmann, T. Elucidation of the nature of the conformational changes of the EF-interhelical loop in bacteriorhodopsin and of the helix VIII on the cytoplasmic surface of bovine rhodopsin: A time-resolved fluorescence depolarization study. *J. Mol. Biol.* **2003**, *328*, 705–719. [CrossRef]
18. Kim, T.Y.; Winkler, K.; Alexiev, U. Picosecond multidimensional fluorescence spectroscopy: A tool to measure real-time protein dynamics during function. *Photochem. Photobiol.* **2007**, *83*, 378–384. [CrossRef] [PubMed]

19. Richter, C.; Schneider, C.; Quick, M.T.; Volz, P.; Mahrwald, R.; Hughes, J.; Dick, B.; Alexiev, U.; Ernsting, N.P. Dual-fluorescence pH probe for bio-labelling. *Phys. Chem. Chem. Phys.* **2015**, *17*, 30590–30597. [CrossRef] [PubMed]

20. Türk, H.; Haag, R.; Alban, S. Dendritic polyglycerol sulfates as new heparin analogues and potent inhibitors of the complement system. *Bioconjugate Chem.* **2004**, *15*, 162–167. [CrossRef] [PubMed]

21. Alexiev, U.; Farrens, D.L. Fluorescence spectroscopy of rhodopsins: Insights and approaches. *Biochim. Biophys. Acta* **2014**, *1837*, 694–709. [CrossRef] [PubMed]

22. Woelke, A.L.; Kuehne, C.; Meyer, T.; Galstyan, G.; Dernedde, J.; Knapp, E.W. Understanding selectin counter-receptor binding from electrostatic energy computations and experimental binding studies. *J. Phys. Chem. B* **2013**, *117*, 16443–16454. [CrossRef] [PubMed]

23. Alexiev, U.; Scherrer, P.; Marti, T.; Khorana, H.G.; Heyn, M.P. Time-resolved surface-charge change on the cytoplasmic side of bacteriorhodopsin. *Febs Lett.* **1995**, *373*, 81–84. [CrossRef]

24. Möller, M.; Alexiev, U. Surface charge changes upon formation of the signaling state in visual rhodopsin. *Photochem. Photobiol.* **2009**, *85*, 501–508. [CrossRef] [PubMed]

25. Narzi, D.; Winkler, K.; Saidowsky, J.; Misselwitz, R.; Ziegler, A.; Böckmann, R.A.; Alexiev, U. Molecular determinants of major histocompatibility complex class I complex stability: Shaping antigenic features through short and long range electrostatic interactions. *J. Biol. Chem.* **2008**, *283*, 23093–23103. [CrossRef] [PubMed]

26. Festy, F.; Ameer-Beg, S.M.; Ng, T.; Suhling, K. Imaging proteins *in vivo* using fluorescence lifetime microscopy. *Mol. Biosyst.* **2007**, *3*, 381–391. [CrossRef] [PubMed]

27. Alnasif, N.; Zoschke, C.; Fleige, E.; Brodwolf, R.; Boreham, A.; Rühl, E.; Eckl, K.M.; Merk, H.F.; Hennies, H.C.; Alexiev, U.; Haag, R.; Küchler, S.; Schäfer-Korting, M. Penetration of normal, damaged and diseased skin—An *in vitro* study on dendritic core-multishell nanotransporters. *J. Control. Release* **2014**, *185*, 45–50. [CrossRef] [PubMed]

28. Ostrowski, A.; Nordmeyer, D.; Boreham, A.; Brodwolf, R.; Mundhenk, L.; Fluhr, J.W.; Lademann, J.; Graf, C.; Rühl, E.; Alexiev, U.; Gruber, A.D. Skin barrier disruptions in tape stripped and allergic dermatitis models have no effect on dermal penetration and systemic distribution of ahaps-functionalized silica nanoparticles. *Nanomedicine* **2014**, *10*, 1571–1581. [CrossRef] [PubMed]

29. Ostrowski, A.; Nordmeyer, D.; Boreham, A.; Holzhausen, C.; Mundhenk, L.; Graf, C.; Meinke, M.C.; Vogt, A.; Hadam, S.; Lademann, J.; Rühl, E.; Alexiev, U.; Gruber, A.D. Overview about the localization of nanoparticles in tissue and cellular context by different imaging techniques. *Beilstein J. Nanotechnol.* **2015**, *6*, 263–280. [CrossRef] [PubMed]

30. Witting, M.; Boreham, A.; Brodwolf, R.; Vávrová, K.; Alexiev, U.; Friess, W.; Hedtrich, S. Interactions of hyaluronic acid with the skin and implications for the dermal delivery of biomacromolecules. *Mol. Pharm.* **2015**, *12*, 1391–1401. [CrossRef] [PubMed]

Sample Availability: Samples of the compound dPGS-ICC are available from the authors.

Detecting and quantifying biomolecular interactions of a dendritic polyglycerol sulfate nanoparticle using fluorescence lifetime measurements

3.6 Polyglycerolsulfate functionalized gold nanorods as optoacoustic signal nanoamplifiers for in vivo bioimaging of rheumatoid arthritis

Jonathan Vonnemann, Nicolas Beziere, Christoph Böttcher, Sebastian B. Riese, Christian Kuehne, Jens Dernedde, Kai Licha, Claudio von Schacky, Yvonne Kosanke, Melanie Kimm, Reinhard Meier, Vasilis Ntziachristos, Rainer Haag

Zu dieser Veröffentlichung hat der Autor mit der Durchführung und Auswertung der SPR Bindungsstudien und der Erstellung von Teilen des Manuskripts beigetragen.

Vonnemann, J., N. Beziere, C. Bottcher, S. B. Riese, C. Kuehne, J. Dernedde, K. Licha, C. von Schacky, Y. Kosanke, M. Kimm, R. Meier, V. Ntziachristos and R. Haag (2014) Polyglycerolsulfate functionalized gold nanorods as optoacoustic signal nanoamplifiers for in vivo bioimaging of rheumatoid arthritis. *Theranostics*. **4**, 629-41.

Polyglycerolsulfate functionalized gold nanorods as optoacoustic signal nanoamplifiers for in vivo bioimaging of rheumatoid arthritis

Polyglycerolsulfate Functionalized Gold Nanorods as Optoacoustic Signal Nanoamplifiers for In Vivo Bioimaging of Rheumatoid Arthritis

Jonathan Vonnemann[1✉], Nicolas Beziere[2✉], Christoph Böttcher[3], Sebastian B. Riese[4], Christian Kuehne[4], Jens Dernedde[4], Kai Licha[5], Claudio von Schacky[6], Yvonne Kosanke[6], Melanie Kimm[6], Reinhard Meier[6], Vasilis Ntziachristos[2], Rainer Haag[1]

1. Institute of Chemistry and Biochemistry, Freie Universität Berlin, 14195 Berlin, Germany;
2. Chair for Biological Imaging, Technische Universität München, 81675 Munich, Germany and Institute for Biological and Medical Imaging, Helmholtz Zentrum München, 85764 Neuherberg, Germany;
3. Research Centre of Electron Microscopy and Core Facility BioSupraMol, Freie Universität Berlin, 14195 Berlin, Germany;
4. Institute of Laboratory Medicine, Clinical Chemistry and Pathobiochemistry, Charité-Universitätsmedizin Berlin, 13353 Berlin, Germany;
5. mivenion GmbH, 10115 Berlin, Germany;
6. Department of Radiology, Klinikum rechts der Isar, Technische Universität München, 81675 Munich, Germany.

✉   Corresponding   authors: Jonathan   Vonnemann,   jonathan.vonnemann@chemie.fu-berlin.de;   Nicolas   Beziere, nicolas.beziere@helmholtz-muenchen.de.

Abstract

We have synthesized a targeted imaging agent for rheumatoid arthritis based on polysulfated gold nanorods. The CTAB layer on gold nanorods was first replaced with PEG-thiol and then with dendritic polyglycerolsulfate at elevated temperature, which resulted in significantly reduced cytotoxicity compared to polyanionic gold nanorods functionalized by non-covalent approaches. In addition to classical characterization methods, we have established a facile UV-VIS based $BaCl_2$ agglomeration assay to confirm a quantitative removal of unbound ligand. With the help of a competitive surface plasmon resonance-based L-selectin binding assay and a leukocyte adhesion-based flow cell assay, we have demonstrated the high inflammation targeting potential of the synthesized gold nanorods *in vitro*. In combination with the surface plasmon resonance band of AuNRs at 780 nm, these findings permitted the imaging of inflammation in an *in vivo* mouse model for rheumatoid arthritis with high contrast using multispectral optoacoustic tomography. The study offers a robust method for otherwise difficult to obtain covalently functionalized polyanionic gold nanorods, which are suitable for biological applications as well as a low-cost, actively targeted, and high contrast imaging agent for the diagnosis of rheumatoid arthritis. This paves the way for further research in other inflammation associated pathologies, in particular, when photothermal therapy can be applied.

Key words: gold nanorods, optoacoustic, dendritic polyglycerolsulfate, inflammation, polyanion, MSOT.

1. Introduction

The use of multiple wavelengths for illumination, advanced data processing methods, and identification and distribution of photoabsorbers based on their light absorbance spectra enables multispectral optoacoustic tomography (MSOT) to exceed the depth and resolution of classical optical imaging methods [1]. As pulsed laser light reaches photoabsorbers, pressure waves are emitted as a result of their ther-

moelastic expansion, which can be detected by classical ultrasonic transducers [2]. While classical optical methods require challenging multi-step syntheses of organic dyes, MSOT can circumvent this problem because of its ability to image photo-absorbance *in vivo* without relying on fluorescence. Anisotropic gold colloids, *i.e.*, gold nanorods (AuNRs), are extremely well suited as a contrast agent because of their predominantly non-radiative de-excitation which results in one of the highest photothermal conversions and thus efficiency known in literature [1,3]. Consequently, they are well detectable by MSOT as recently shown in different models [4,5]. Their anisotropy results in a transversal and longitudinal surface plasmon resonance (TSPR/LSPR) band, of which the latter is especially interesting for *in vivo* applications due to its adjustable absorption wavelength that is dependent on the dimension of the nanorod [6,7]. An LSPR band that absorbs within the "water window" absorption range of 700-1200 nm, therefore minimizing photon absorption by tissue components, is thus readily accessible just by increasing the aspect ratio of the AuNRs [8]. Nevertheless, capitalizing on the favorable optoacoustic properties in imaging of inflammation *via* MSOT requires targeted AuNRs. Moieties for the targeting of inflammation associated pathologies, *i.e.*, in cancer, mostly consist of expensive peptides or synthetically challenging oligosaccharides. Low-cost polymeric dPGS, however, has been shown by our group to exhibit high affinity towards leukocytes and inflamed endothelia, mainly governed by their interaction with L- and P-selectin [9,10]. Selectins and their ligands play prominent roles in inflammation and disease and are crucial for the innate immune response [11]. Effective leukocyte recruitment requires these cell adhesion molecules, as demonstrated in mice that lack selectins or selectin ligands [12,13]. P- and E-selectin are expressed on vascular epithelia at high density at sites of inflammation. Therefore it is not surprising that both molecules have been used as targets for drug delivery and imaging purposes [14,15]. Due to the low affinity of the most abundant physiological ligand for all selectins, the tetrasaccharide SiaLe^x, antibodies were mainly used as high affinity probes for selectin targeting *in vivo*. Recently an antibody directed fluorescence imaging of E-selectin was successfully applied in a mouse model for arthritis and the authors claimed that the quantified fluorescence signal can be related to a disease score [16]. Besides the interaction of selectins with specific antibodies, numerous experiments confirm an essential electrostatic contribution in L- and P-selectin binding [17–20]. Our group has shown that sulfates are by far the strongest binders for L- and P-selectin of all anions, which explains the high

binding affinity of dPGS [21]. The targeting potential of dPGS has already been successfully exploited by our group in several mouse models for the *in vivo* imaging of inflammation with synthetically challenging organic fluorophores [22–24], while difficulties in the anionic functionalization prohibited the use of readily available gold nanorods as imaging modality. Although gold nanorods can be synthesized by a single-step, gram-scale procedure [25], the functionalization of gold nanorods for biocompatibility and active targeting is not trivial. In order to achieve an anisotropic growth of gold nanorods, a highly concentrated solution of cetyltrimethylammonium bromide (CTAB) is required for the stabilization of the dispersion [8]. This surfactant is not only inherently cytotoxic, it also renders the nanorods cationic in surface charge [8]. The polyanionic functionalization of the gold nanorods is thus challenging, as the strong interaction of anionic substances with the positively charged CTAB prohibits ligand exchange on the gold nanorods. Therefore, several synthetic methods have been established for the anionic functionalization of AuNRs including layer-by-layer (LBL) coating with polyelectrolytes [26,27], silica-functionalization with subsequent grafting from/to [28], and a round-trip phase transfer of the gold nanorods [29]. Layer-by-layer functionalization proved to not be applicable for *in vivo* applications because the supramolecular structures were unstable under high salt concentrations. The alternative, namely, functionalizing silica coated AuNRs, is chemically demanding as this requires fine-tuned reaction conditions and solvent mixtures for retaining the colloidal stability. We present here, for the first time, a reliable method for the preparation of covalently functionalized polysulfated AuNRs stable under physiological conditions *via* a thermally induced ligand replacement reaction of PEG. Even though displacement of monothiol ligands for quantification by dithiothreitol (DTT) at room temperature is reported in the literature [30], a thermally induced replacement of PEG-thiol by disulfide modified ligands has not been reported as a functionalization mechanism. As the CTAB and PEG replacement reactions are performed in aqueous solution and do not require additional solvents, this offers a new universal method for the functionalization of gold nanorods with anionic ligands. The intermediate PEGylation step renders the AuNR surface neutral and at the same time sterically stabilizes the colloid. Given the targeting properties of dPGS, they are expected to specifically address inflamed tissue and bind to L-selectin of invading leukocytes as well as to P-selectin expressed on vascular epithilia [22]. Therefore, we employed in this study a well-established murine rheumatoid arthritis model to observe the

Polyglycerolsulfate functionalized gold nanorods as optoacoustic signal nanoamplifiers for in vivo bioimaging of rheumatoid arthritis

accumulation of AuNR-dPGS at the inflamed region of the joints [31]. For the first time, we were able to show the successful application of an inflammation targeted, colloidal contrast agent for MSOT. The easy functionalization of readily available AuNR-CTAB with the low-costs of dPGS highlights the advantage of nanoparticular imaging agents over conventional organic dyes and establishes a basis for a cheap and efficient diagnosis and photothermal therapy of additional inflammatory diseases. Furthermore, the established thermally induced ligand exchange of PEG offers a novel method for the functionalization of anisotropic gold colloids with hydrophilic ligands.

2. Experimental

2.1 Materials

Air and moisture sensitive reactions were carried out in flame-dried glassware under argon atmosphere. Anhydrous solvents were either commercially purchased from Acros Organics™ in septum sealed bottles or chemically dried using a MBRAUN SPS 800 solvent purification system. All other chemicals were purchased from Aldrich™. Cellulose acetate filters (0.2 µm) were purchased from Whatman™. TA-NHS ester was synthesized according to the method described by Bawendi *et al*. 10% amine and 85% sulfate functionalized dendritic polyglycerolsulfate with an average molecular weight of 10 kDa was provided by mivenion GmbH [32]. Centrifugation was performed with a Hettich™ Rotina 380R. ^{1}H-NMR and ^{13}C-NMR spectra were recorded on a Bruker™ Biospin spectrometer operating at 700 MHz. The chemical shifts are reported in δ (ppm) and were referenced to the solvent peak. Multiplicities are indicated by s (singlet), d (doublet), t (triplet), q (quartet) and m (multiplet). The corresponding coupling constants J are reported in Hertz (Hz). Data analysis was performed using MestReNova™ version: 6.0.2. UV/Vis absorption spectra were recorded using a UV/Vis spectrophotometer by Scinco™ Co., LTD. Data analysis was performed by the corresponding LabProPlus™ software. Dynamic light scattering and zeta potential measurements were performed on a Zetasizer Nano ZS analyzer™ with integrated 4 mW He-Ne laser, λ = 633 nm (Malvern Instruments™ Ltd, U.K.). Transmission electron microscopy was conducted on a CM-12 by FEI™ with an accelerating voltage of 100 kV. Graphical analysis of TEM images were performed using JImage v1.43.

2.2 Chemical Synthesis

2.2.1 Synthesis of TA-dPGS 10 kDa

dPGS-Amine 10 kDa (500 mg, 0.05 mmol) was dissolved in a mixture of dimethylformamide (16 mL)

and distilled water (4 mL). TA–NHS ester (15.15 mg, 0.05 mmol) and *N,N*-diisopropylethylamine (0.017 mL, 0.1 mmol) were added and the solution was stirred for 3 d. The solvent was removed *in vacuo* and the crude product dialyzed against 100 mM sodium chloride solution and distilled water in a regenerated cellulose dialysis tube with a MW cut-off of 2000 g/mol. After lyophilization, the product was obtained as white crystals (491 mg, 98%).

^{1}H-NMR (700 MHz, D$_2$O): δ (ppm) 4.90-3.21 (m, 338 H, PG-backbone, S–S–**CH$_2$**–) 3.21 – 3.06 (m, 2 H, S–S–**CH$_2$**–, S–S–**CH**–), 2.69 (m, 1 H, S–**CH$_2$**–**CH$_2$**–), 2.48 (t, 2 H, *J* = 7.5 Hz, **CH$_2$**CO–), 2.20 (m, 1 H, S–**CH$_2$**–**CH$_2$**–), 1.95 – 1.53 (m, 6 H, **CH$_2$**–**CH$_2$**–**CH$_2$**–**CH$_2$**CO–), 1.55 (t, 2H, **CH$_2$**- initiator) 0.78 (m, 3 H, **CH$_3$**- initiator).

^{13}C-NMR (700 MHz, D$_2$O): δ (ppm) 177.4 (1 C, -CO-NH-), 78-66 (PG-backbone), 56.6 (1 C, -S-CH-), 54.5 (1 C, -NH-CH-), 42.7 (1 C, -C- starter), 41.2 (1 C, -S-CH$_2$-), 38.3 (1 C, -CH$_2$-CO-), 35.7 (1 C, -S-CH$_2$-CH$_2$-), 33.9 (1 C, -S-CH-CH$_2$-), 28.0 (1 C, -CO-CH$_2$-CH$_2$-CH$_2$-), 25.1 (1 C, -CO-CH$_2$-CH$_2$-CH$_2$-), 22.0 (1 C, -CH$_2$-CH$_3$ initiator), 7.0 (1 C, -CH$_2$-CH$_3$ initiator) sulfur content from elemental analysis: 15.5%

2.2.2 Synthesis of AuNR-CTAB

Gold nanorods were synthesized according to a slightly modified procedure described by Nikhil R. Jana [25]. Cetyltrimethylammonium bromide (18.225 g, 50 mmol) was added to a solution of hydrogen tetrachloroaureate(III) hydrate (98.5 mg, 0.25 mmol) in ultrapure water (255 mL) at 35 °C under magnetic stirring. The color changed from yellow to deep red. The solution was cooled down to RT and silver nitrate (8.48 mg, 50 µmol) and ascorbic acid (88 mg, 0.5 mmol) was added to the reaction mixture, resulting in a colorless solution. After the fast addition of an aqueous solution of sodium borohydride (25 µL, 1 mM) under rapid stirring, the reaction mixture turned from colorless to dark purple within 30 min. The colloidal dispersion was purified twice by centrifugation at 6,500 rpm and 35 °C for 2 h and redispersion in water, and was stored in the dark at 4 °C.

2.2.3 Synthesis of AuNR-PEG

Poly(ethylene glycol)monomethyl ether thiol (134 mg, 134 mmol, 1.24·10^5 eq.) was added to a dispersion of AuNR-CTAB (4 mL, 270 nM) and stirred for 24 h at RT. The colloidal dispersion was purified twice by centrifugation at 6,500 rpm for 1.5 h and redispersion in ultrapure water and stored in the dark at 4 °C.

2.2.4 Synthesis of AuNR-dPGS

TA-dPGS 10 kDa (270 mg, 27 µmol, 1.24·10^5 eq.) were added to an aqueous dispersion of AuNR-PEG

Polyglycerolsulfate functionalized gold nanorods as optoacoustic signal nanoamplifiers for in vivo bioimaging of rheumatoid arthritis

(15 mL, 14.5 nM), decanted into 1.5 ml Eppendorf tubes and agitated at 60 °C for 12 h. The colloidal dispersion was purified five times by centrifugation at 11,000 rpm for 15 min and redispersion in ultrapure water and stored in the dark at 4 °C.

2.3 Characterization and biological evaluation

2.3.1 Quantification of dPGS mass-fraction on AuNRs via ATR-FTIR

The calibration curve was established by measuring the absorption of the characteristic stretching vibrations of TA-dPGS (1224 cm^{-1}) and mPEG$_{1000}$-SH (1105 cm^{-1}) for seven different mass-fractions of TA-dPGS between X(TA-dPGS)=0-1 *via* ATR-FTIR spectroscopy. For this, 1 µl of the aqueous solutions were placed on the ATR-crystal and dried under air flow until the IR spectrum did not exhibit any further changes. AuNR-dispersions were measured in an analogous manner.

2.3.2 BaCl₂ induced agglomeration assay

For a typical aggregation test, an aqueous dispersion of gold nanorods (0.5 mL, 2.72 nM, 1.6 OD) was incubated with either BaCl$_2$ (0.5 mL, 66 mM, IS=200 mM) or NaCl (0.5 mL, 0.2 mM, IS=200 mM). Directly after addition of the salt, UV-VIS absorption spectra were recorded at 20 s time intervals.

SPR-based competitive L-selectin binding assay

Binding of AuNR-PEG and AuNR-dPGS to L-selectin was tested by inhibition of L-selectin binding to an artificial ligand *via* a competitive binding assay performed on a BIACore X device (GE Healthcare, Freiburg, Germany) [9,10,33,34]. Briefly, protein A coated gold nanoparticles (15 nm, Aurion, Wageningen, Netherlands) were loaded with L-selectin/Fc chimera (R&D systems, Minneapolis, USA). The binding signal to the artificial ligand bound onto a streptavidin coated gold chip (GE Healthcare, Freiburg, Germany) was measured, and samples without gold nanorods were set to 100%. In turn, binding signals of the L-selectin loaded gold nanoparticles preincubated with different concentrations of either AuNR-PEG or AuNR-dPGS were taken, yielding the respective dose-dependent curve.

2.3.3 Parallel plate flow chamber assay

The human leukemia cell line K562 stably transfected with L-selectin was used to study ligand binding in cell rolling assays. Cells were resuspended in Hanks' balanced salt solution (PAA, Pasching, Austria) to a final concentration of 1×10^6 cells/ml and transferred into a syringe. A parallel plate flow chamber (µ-slide VI, ibidi GmbH, Germany) was incubated with 30 µg/ml of the L-selectin ligand

PSGL-1-Fc (R&D Systems, Wiesbaden, Germany) for 2 h at room temperature in order to coat the surface. Subsequently, the surface was blocked with bovine serum albumin (2 mg/ml) for 30 min. The flow channel was connected to a high precision perfusion pump KDS 101 (KD Scientific, Holliston, MA, USA) and the assays were performed at a constant shear stress of 1 dyn/cm². An inverted microscope IM (Carl Zeiss AG, Oberkochen, Germany) that had been equipped with a digital camera AxioCam MRc (Carl Zeiss AG, Jena, Germany) was used to visualize the cell rolling. To monitor inhibition of receptor-ligand interaction, cells were respectively preincubated for 10 min at 37 °C with AuNR-dPGS or AuNR-PEG at given concentrations. Movies were taken at 100× magnification for a 1 min period and the number of rolling cells (flux) was determined by counting.

2.3.4 Cytotoxicity assay

Cytotoxicity of AuNR-CTAB, AuNR-PEG and AuNR-dPGS was analyzed in real time by the impedance based xCELLigence System (RTCA device, Roche Applied Science, Mannheim, Germany). Therefore a 96 well e-plate (Roche Applied Science, Mannheim, Germany) was precoated with collagen and filled with 50 µl Epithelia-Cell-Growth-Medium + supplement mix (Promocell, Germany) + 1% penicillin/streptomycin (PAA, Germany) per well to take the blank values. After that, HUVECs were cultured (2500 cells/well) in corresponding wells yielding 100 µl volume per well. The cells were allowed to settle down for 30 min at RT before incubation at 37 °C and 5% CO$_2$ for 24 h. Proliferation was monitored by increasing impedance automatically by the RTCA.

Samples were added to the cells, yielding a final volume of 150 µl and impedance was analyzed for another 4 days at 37 °C and 5% CO$_2$.

Data collected during the experiment were analyzed with RTCA Software 1.2.1.1002 (Roche Applied Science).

2.4 MSOT imaging

2.4.1 Animal model

All animal experiments were performed with the approval of the Government of Upper Bavaria (Reference number 55.2-1-54-2532-179-11). We used a collagen induced arthritis CIA mouse model, which is widely used as an arthritis model, because of its strong similarity to human rheumatoid arthritis [31]. For the induction of the arthritis, Complete Freund's Adjuvant CFA, which consists of mineral oil and heat-killed *Mycobacterium tuberculosis* at a concentration of 1 mg/ml, and a phosphate buffered saline (PBS) solution containing bovine type II collagen at a concentration of 1 mg/ml were mixed together in

633

equal parts. 20 µl of this compound were injected between the left knee and ankle. Within approximately 25-30 days after the injection, most animals developed moderate to advanced arthritis. All animals were examined daily for their general state of health and specifically for arthritis associated symptoms. Swelling, redness, and lameness of the arthritic leg were graded by an experienced veterinarian in a scale from 0 to 3, where 0 stands for no, 1 for mild, 2 for moderate, and 3 for severe development of each symptom. For this study, 6 animals with arthritis were used (4 for AuNR-dPGS, 2 for AuNR-PEG).

2.4.2 Optoacoustic imaging procedure and processing

All MSOT measurements were performed in a custom-built real time optoacoustic imaging system adapted from previously described equipment [35]. Briefly, optical excitation was provided by a Q-switched Nd:YAG laser with a pulse duration of around 10 ns and a repetition rate of 10 Hz and a tunable range of 680-980 nm. Homogeneous delivery of light to the sample was achieved using a fiber bundle split into 10 output arms. A cylindrically focused 256-element transducer array with a central frequency of 5 MHz was used to detect and record the emitted ultrasound waves, allowing acquisition of transverse plane images. A moving stage enabled the imaging of different planes by the static illumination and detection devices. Measurements were performed in a temperature controlled water bath (34 °C) for acoustic coupling and a thin clear polyethylene membrane attached to the sample holder was used to keep the samples dry.

2.4.3 In vitro imaging

For *in vitro* imaging, cylindrical phantoms of 2 cm diameter were prepared using a gel made from distilled water containing Agar (Sigma-Aldrich, St. Louis, MO, USA) for jellification (1.3% w/w) and an intralipid 20% emulsion (Sigma-Aldrich, St. Louis, MO, USA) for light diffusion (6% v/v), which resulted in a gel with a reduced scattering coefficient of $\mu'_s \approx 10\ cm^{-1}$. A cylindrical inclusion containing various concentrations of the sample of approximately 3 mm diameter was put approximately in the middle of the phantom, along with a tube containing classical black ink with an optical density of around 0.2 for intensity measurement references. Imaging was performed using 20 averages per illumination wavelength, from 680 to 900 nm in steps of 5 nm.

2.4.4 In vivo imaging

Imaging of the animals was performed roughly from toes to hips using 0.5 mm steps in order to image the whole region possibly inflamed. After injection of 5 mg/kg of AuNR *i.v.* in the animals, a similar con-

centration to what is classically used in the field, the lower half of the body was imaged with transversal slides at various time points, ranging from directly after injection to 24 h post-injection. Data acquisition was performed using 30 averages per illumination wavelengths, which were as followed: 700, 730, 760, 800, 830, and 860 nm. This resulted in an acquisition time of around 20 minutes.

Data processing was performed using the commercial suite proposed by iThera Medicals (Munich, Germany). Briefly, model based image reconstruction is performed on the raw data and followed by spectral unmixing, based on spectral fitting by the least square method.

For 3D-video reconstruction, 2D images from MSOT experiments were processed using Amira® (VGS, Burlington, MA, USA), using volume rendering of thresholded images stacks. The anatomical data, which came from 800 nm illumination experiments (grey), is displayed using 50% transparency. The dPGS-AuNR volume (green) is displayed with 0% transparency.

3. Results and Discussion

3.1. Gold nanorod functionalization: CTAB to dPGS

Dendritic polyglycerolsulfate with a molecular weight of 10 kDa was chosen as an active ligand for the functionalization of gold nanorods due to low-cost [36], confirmed targeting potential for inflammatory diseases [22–24], and strong electrosteric repulsion required for stabilizing large colloids under physiological conditions. Furthermore, the high molecular weight of the polymer favors a ligand exchange reaction due to entropic gain upon replacing smaller molecular weight ligands. The obtained polymer with a molecular weight of ~10 kDa presented approximately 70 functional groups at the periphery with a degree of amination and sulfation of 10% and 85%, respectively. As a result, approximately seven amine groups are available for functionalization *via* amide coupling, while 60 sulfate groups form the predominant part of the polymer surface. TA-dPGS was synthesized by a simple amide coupling of *N*-hydroxysuccinimide (NHS) activated thioctic acid (TA) which was prepared by a procedure established by Liu *et al.* [32], to the 10% amine functionalized dendritic polyglycerolsufate with a molecular mass of 10 kDa as presented in Scheme 1A. After careful adjustment of the dimethylformamide/water solvent ratio, the reaction was performed with quantitative yields and resulted in approximately one equivalent of TA per polymer as confirmed by ^{1}H-NMR.

CTAB functionalized gold nanorods were syn-

Polyglycerolsulfate functionalized gold nanorods as optoacoustic signal nanoamplifiers for in vivo bioimaging of rheumatoid arthritis

thesized by a slightly modified, one-step synthetic method established by Nikhil R. Jana [25], resulting in nearly monodisperse gold nanorods as confirmed by the transmission electron micrographs presented in the Additional file 1: Figure S1. In order to remove excess CTAB, the synthesized gold nanorods were centrifuged twice at 6500 rpm at 35 °C for 2 h, the supernatant was removed, and the rods redispersed

in water. Further purification would have resulted in aggregation due to deceeding of the critical [CTAB]/[AuNR] ratio of $7.4 \cdot 10^5$ required for a stable AuNR-CTAB dispersions [37]. The subsequent ligand exchange reactions on the gold nanorods were performed by a two-step method that permitted the complete removal of free CTAB before the addition of the polyanion (Scheme 1B).
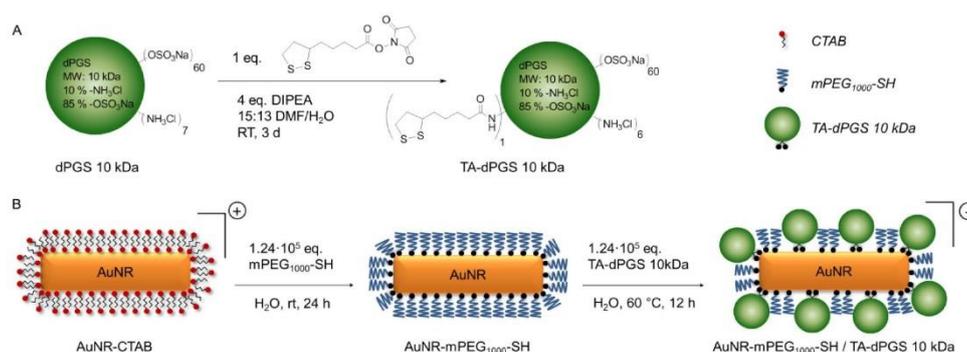
Scheme 1. (A) Synthesis of thioctic acid functionalized dendritic polyglycerolsulfate *via* amide coupling. (B) Functionalization of CTAB double-layer coated gold nanorods with mPEG$_{1000}$-SH followed by a partial replacement of mPEG$_{1000}$-SH with TA-dPGS 10 kDa *via* thermally induced ligand exchange reaction. Note: Elements in the scheme are not drawn to scale.

PEGylation was performed by incubating the AuNR-CTAB with $1.24 \cdot 10^5$ eq. of mPEG$_{1000}$–SH as this ratio was identified to result in the highest possible degree of functionalization by a simple ligand exchange as the binding process is relatively slow [38]. The ligand exchange was confirmed macroscopically due to the perfect dispersability of the AuNRs in ethanol. As additional proof, an evenly spaced gold nanorod assembly with an interparticle diameter approximately resembling twice the length of an extended mPEG$_{1000}$-SH chain was visualized by transmission electron microscopy (TEM) (Additional file 1: Figure S1B). Attenuated total reflectance – fourier transform infrared spectroscopy (ATR-FTIR) measurements further confirmed the functionalization with mPEG$_{1000}$-SH due to the appearance of the characteristic (C-O-C) stretching vibration at 1100 cm^{-1} (Figure 1).

Since residual CTAB and mPEG$_{1000}$-SH would hinder the TA-dPGS ligand exchange on the nanorods, mPEG$_{1000}$-SH functionalized AuNRs were purified twice by centrifugation. Ligand exchange with TA-dPGS 10 kDa was performed by incubation of the purified AuNR-PEG$_{1000}$ with $1.24 \cdot 10^5$ eq. of TA-dPGS 10 kDa at 60 °C over 12 h. The elevated temperature of 60 °C was applied in order to capitalize upon the entropic gain by exchanging the smaller AuNR-PEG$_{1000}$

with TA-dPGS 10 kDa and to accelerate the replacement of the mono-thiol with the more stable bivalent anchor moiety by breaking the thiol-gold coordinative bond. By estimating the surface area of a single gold nanorod and dividing it by an assumed footprint of one TA-dPGS 10 kDa polymer of 1 nm^2, 1400 TA-dPGS 10 kDa molecules would be required for a complete surface coverage of one gold nanorod. Nevertheless, the 88-fold amount, $1.24 \cdot 10^5$ eq., was chosen because the thiol-thiol exchange reaction follows Langmuir diffusion kinetics and the conversion was thus largely dependent on the incoming-outcoming ligand ratio [39]. Furthermore, we were able to show in this specific case that $1.24 \cdot 10^4$ eq. was not sufficient for a successful ligand exchange reaction. Neither was the functionalization with $1.24 \cdot 10^5$ eq. at room temperature successful, even after 72 h of incubation. The removal of unbound TA-dPGS 10 kDa was achieved by five times centrifugation at 11,000 rpm for 15 min, disposal of the supernatant, and redispersion of the nanorods in water. The appearance of the strong stretching vibration characteristic for sulfate groups at 1250 cm^{-1} in the IR spectrum of purified AuNR-dPGS confirmed a successful functionalization with TA-dPGS 10 kDa (Figure 1) [40].

Polyglycerolsulfate functionalized gold nanorods as optoacoustic signal nanoamplifiers for in vivo bioimaging of rheumatoid arthritis
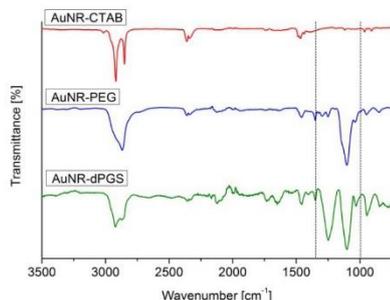
Figure 1. ATR-FTIR spectra of the synthesized gold nanorods. The dotted lines mark the range of wavenumbers with characteristic changes.

Furthermore, in contrast to AuNR-PEG, AuNR-dPGS particles were no longer dispersible in ethanol and precipitated over time, which confirmed the successful functionalization on the macroscopic scale. The characteristic stretching vibrations of PEG and dPGS were further employed for determination of the dPGS to PEG mass ratio, which was identified to be 47.4 +/- 4.1% (Additional file 1: Figure S2, S3). Due to the 10-fold higher molecular mass of TA-dPGS, approximately 10 times more PEG molecules were present on the surface than TA-dPGS molecules. It is noteworthy that dPGS 10 kDa has a hydrodynamic diameter of 6 nm, which is much larger than the hydrodynamic diameter of PEG_{1000}, beeing only 1.72 nm [10,41]. The circular areas covered by one molecule of PEG_{1000} and dPGS 10 kDa were thus approximately 3 nm^2 and 36 nm^2, respectively. As there were 10 times more PEG molecules on the surface than dPGS 10 kDa molecules, but with each covering only 1/12th of the surface, half of the overall gold nanorod surface can be assumed to have been covered by TA-dPGS 10 kDa sticking out of the shorter PEG layer. This maximum degree of functionalization that was achievable by the employed ligand exchange method appears to be reasonable as the highly charged, polyanionic dPGS molecules strongly repel each other. The formation of an evenly spaced TA-dPGS 10 kDa lattice with $mPEG_{1000}$ –SH in-between was thus favored. The addition of salt during the ligand exchange reaction could have increased the degree of dPGS functionalization due to the screening of charges [42], yet we did not encourage this. We have already shown that a higher degree of sulfate functionalization above 40% on a 6 nm dPGS only marginally increased the L-selectin binding affinity, indicating a cap for the multivalent enhancement of the binding affinity [10]. For a smaller dPGS of 3 kDa, higher degrees of functionalization

were required to compensate the smaller size and thus number of binding sites in order to achieve maximum binding affinity. As the gold nanorods are at least one order of magnitude larger than the investigated dendritic polyglycerols, this cap should have been strongly exceeded even by 50% surface coverage of the gold nanorods with TA-dPGS. A further enhancement of the binding affinity of AuNR-dPGS by increasing the dPGS to PEG ratio is therefore unlikely. In this specific case, we even surmise that the mixed PEG/dPGS layer can beneficial for *in vivo* targeting of inflammation, as the clustered sulfate groups on the protein resistant PEG layer mimic the physiological selectin ligand distribution on the surface of inflamed endothelia and leukocytes. Zeta potentials measured by dynamic light scattering (DLS) were furthermore employed for monitoring the functionalization steps. The PEGylation of AuNR-CTAB resulted in a decreased zeta potential from 63.0 +/- 2.9 mV to 5.12 +/- 0.8 mV, clearly indicating a successful ligand exchange reaction. The slightly positive zeta potential of the AuNR-PEG is due to some residual CTAB on the nanorod surface which could not be removed by this simple exchange reaction. Just recently, the group of Alke Petri-Fink established a protocol for removing this small residual amount as well by a two-step place exchange [43]. Nevertheless, this residual amount of CTAB is negligible, as it does not contribute to the cytotoxicity of gold nanorods [44]. The interpretation of the zeta potential after TA-dPGS 10 kDa ligand exchange is ambiguous, as TA-dPGS 10 kDa itself has a zeta potential of approximately -14 mV [10]. The significantly lower zeta potential for gold nanorods functionalized with TA-dPGS of -36.8 +/- 0.85 mV after extensive washing, confirmed a high degree of TA-dPGS functionalization but not the absence of unbound TA-dPGS. The conservation of the optical properties of the gold nanorods was approved *via* normalized absorption spectra which resulted in a LSPR band of 782 nm for AuNR-dPGS, which was perfectly suited for *in vivo* imaging (Additional file 1: Figure S4). Size determination by DLS measurements further confirmed the required stability in buffer for biological testing, as no aggregation could be observed for the AuNR-PEG and AuNR-dPGS (Additional file 1: Figure S6).

3.2. Removal of unbound ligands

The removal of unbound TA-dPGS from the colloidal solution after purification is essential for an accurate determination of the AuNR-dPGS targeting potential. Unfortunately, zeta potential measurements only give cumulative information about the colloidal solution and thus prohibit identification of unbound ligands. Even though altering SPR bands due to

plasmon-plasmon interactions upon reduction of the interparticle diameter by cross-linking has been reported in literature [6,45–47], this has not been used as an analytic tool to assess colloidal purity. We employed $BaCl_2$ to induce agglomeration of sulfate functionalized gold nanorods, which confirmed a successful functionalization with dPGS when the plasmon resonance was altered. The nanorod dispersion was purified *prior* to $BaCl_2$ incubation several times by centrifugation. After each purification cycle, a small sample of the redispersed colloidal dispersion was removed for the $BaCl_2$ agglomeration assay. The respective samples were incubated with $BaCl_2$ and their absorption monitored *via* time-resolved UV-VIS spectroscopy. Surprisingly, no change in plasmon resonance, and thus agglomeration, was observed for samples of unpurified AuNR-dPGS after incubation with $BaCl_2$. There was also no agglomeration for samples of AuNR-dPGS after four purification cycles (Additional file 1: Figure S7). Only samples of five-fold purified AuNR-dPGS exhibited a dramatic change of their plasmon resonance seconds after the addition of $BaCl_2$ (Figure 2).
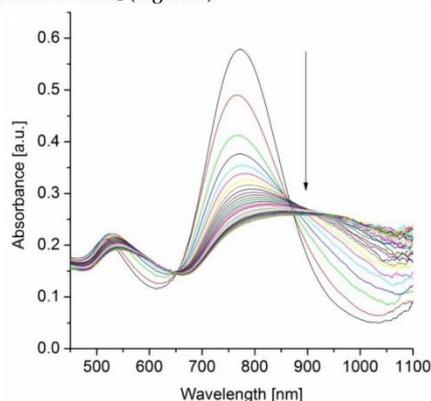
file 1: Figure S9). We surmise that only in the case of highly purified AuNR-dPGS the interparticle distance of agglomerated gold nanorods were small enough for plasmon-plasmon interactions, as the electromagnetic field around the nanorods exponentially decays with distance. In the case of insufficiently purified gold nanorods, the approximately 5 nm large TA-dPGS ligands acted as an additional cross-linker between gold nanorods and thus separated the AuNR-dPGS to an interparticle distance too large for alterations of the plasmon resonance. In order to confirm the specific agglomeration of purified AuNR-dPGS by $BaCl_2$, transmission electron micrographs were recorded as shown in Figure 3.

Figure 2. Time-resolved UV-VIS absorption spectra from 0-600 s in 20 s time steps after the addition of $BaCl_2$ to five-fold purified AuNR-dPGS by centrifugation.

In order to exclude agglomeration effects due to high ionic strength, a control experiment was conducted in which samples of five-fold purified AuNRs-dPGS were incubated with NaCl at an ionic strength of 100 mM. The absence of plasmon coupling and thus agglomeration confirmed the stability of AuNR-dPGS at this ionic strength (Additional file 1: Figure S8). Furthermore, the UV-VIS absorption spectra of PEGylated AuNRs did not change after the addition of $BaCl_2$, which proved the specific interaction of the polysulfate layer with $BaCl_2$ (Additional
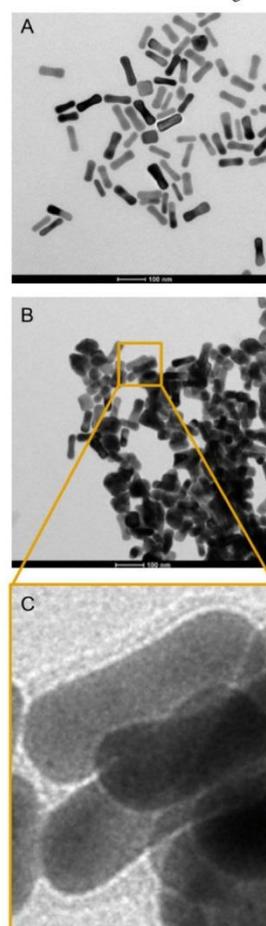

Figure 3. Transmission electron micrographs of purified AuNR-dPGS incubated with (A) NaCl and (B) $BaCl_2$ at an ionic strength of 100 mM. (C) A magnified detail from (B) depicts a dark seam around the nanorods indicating the dPGS corona.

Polyglycerolsulfate functionalized gold nanorods as optoacoustic signal nanoamplifiers for in vivo bioimaging of rheumatoid arthritis

No agglomeration was observed for purified AuNR-dPGS incubated with NaCl (Figure 3A). On the contrary, incubation with $BaCl_2$ induced strong agglomeration of AuNR-dPGS as depicted in Figure 3B, which confirms a solely Ba^{2+}-sulfate induced agglomeration (for even larger agglomerates see Figure S11 in Additional file 1). Due to the high atomic mass of Ba, $BaCl_2$ acted as a positive staining agent and successfully visualized the dPGS corona as presented in Figure 3C. In the case of AuNR-PEG, incubation with $BaCl_2$ neither resulted in aggregation nor staining of the nanorods, confirming the specific, positive staining of sulfates with $BaCl_2$ (Additional file 1: Figure S12). The small interparticle distance between the AuNR-dPGS upon incubation with $BaCl_2$ further explains the change in the SPR bands as plasmon coupling occurs. The assay was furthermore employed to prove the covalent binding of the TA-dPGS to the gold nanorod, as AuNR functionalized in an analogous manner with dPGS without thioctic acid moiety and did not show any signs of agglomeration after incubation with $BaCl_2$ (Additional file 1: Figure S10).

3.3. *In vitro* determination of AuNR-dPGS L-selectin and leukocyte binding

In order to acquire quantitative information about the binding strength of AuNR-dPGS to L-selectin, a competitive binding assay based on surface plasmon resonance measurements (SPR) was performed [9,10,33,34]. In this assay, the binding of L-selectin coated 15 nm gold nanoparticles (AuNP) with a synthetic L-selectin ligand-modified sensor chip was measured as the positive control and normalized to 100% binding. Subsequently, the L-selectin coated AuNPs were preincubated with increasing concentrations of the respective gold nanorod sample and the relative binding was determined (Figure 4A). While AuNR-PEG did not show any inhibition of L-selectin ligand binding, AuNR-dPGS proved to be a potent inhibitor with an IC_{50} value of 135 pM, calculated on the basis of the nanorod concentration. Removal of the unbound TA-dPGS was essential for an accurate determination of the binding affinity, since soluble dPGS already exhibits an IC_{50} value of 8 nM [10].

In order to test the efficiency of AuNR-dPGS as a L-selectin inhibitor under more physiological conditions, the nanorods were applied in a cellular based flow chamber assay (Figure 4B) [10,48]. Therefore, L-selectin transfected K562 cells were passed through a PSGL-1-coated flow channel under a constant shear stress of 1 dyn/cm². The number of rolling cells (flux) of the untreated cells was set to 100%. The flux of the treated cells (preincubated with AuNR-dPGS and AuNR-PEG) was calculated as a percentage flux of the

control (representative movies are provided in the Supplementary Material). Figure 4B confirms a strong binding of AuNR-dPGS to the cells with an IC_{50} value of 9 nM. The nearly 10-fold higher IC_{50} value compared to the SPR measurements is due to the much higher concentration of L-selectin presented on the cells in comparison to the gold nanoparticles in the SPR assay.
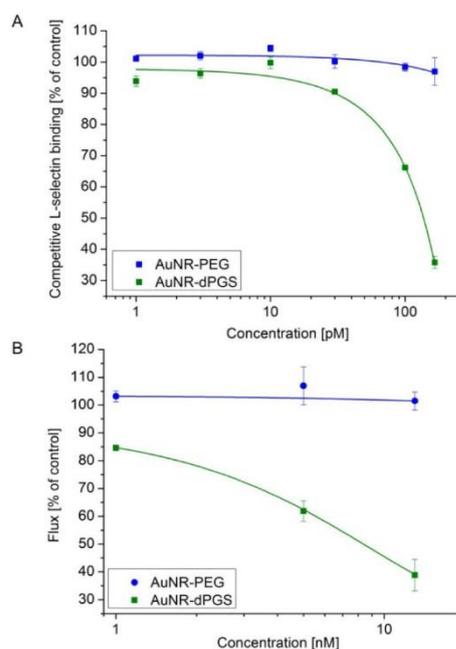
Figure 4. (A) Competitive L-selectin binding with different concentrations of gold nanorods. **(B)** Inhibition of leukocyte binding to immobilized ligands in a modified flow chamber by AuNR-dPGS. Data correspond to mean +/- SEM.

3.4. *In vitro* cytotoxicity of AuNRs

The cytotoxicity of the synthesized gold nanorods on human umbilical vein endothelial cells (HUVECs) was evaluated *via* a real time cell analyzer (RTCA) based on impedance measurements (Additional file 1: Figure S13). For AuNR-CTAB, particle concentrations >0.1 nM already resulted in complete death of the HUVECs after 1 day of incubation. The high cytotoxicity is in agreement with the results of Wyatt and coworkers, who have previously shown that AuNR-CTAB has a strong cytotoxic effect on HT-29 cells in concentrations of ≥ 0.2 nM after 4 days of exposure [49]. AuNR-CTAB`s high cytotoxicity was ascribed to the unbound CTAB in solution required to

stabilize the gold nanorods and not to particle bound CTAB. PEGylation and subsequent purification removed the CTAB and thus significantly lowered the cytotoxicity of AuNR-PEG by > 40-fold, as even concentrations as high as 20 nM did not show any cytotoxic effect on the proliferation of HUVECs. AuNR-dPGS was not cytotoxic at concentrations < 5 nM. Possible changes in the cytotoxicity due to aggregation can be excluded [50], as the stability of AuNR-PEG and AuNR-dPGS in PBS was confirmed by DLS measurements (Additional file 1: Figure S6). Van Leeuwen and coworkers investigated the cytotoxicity of gold nanorods functionalized with polystyrene sulfonate by a LBL approach (AuNR-PSS) [44]. For the investigated cell lines, *i.e.*, SKBR3, CHO, C2C12, HL60, 50% cell death was observed in all cases after 1 day of incubation with concentrations ≤ 0.05 nM. We surmise that the significantly lower cytotoxicity of AuNR-dPGS was from the absence of complexed CTAB. As the LBL functionalization of gold nanorods prohibits the complete removal of CTAB from the solution before the addition of the polyanion, large amounts of CTAB are complexed within the polyanionic layer. The thermally induced ligand exchange of PEG permitted the removal of unbound CTAB before addition of the polyanion and thus significantly lowers the resulting cytotoxicity.

3.5. AuNR-dPGS as MSOT contrast agents

In order to compare the influence of the grafting dPGS onto the surface of AuNR with the more commonly used PEG coating, we synthesized both types of surface functionalization and their properties investigated with an optoacoustic imaging system. Figure 5 shows spectra and sensitivity assays in MSOT. In Figure 5A, it can be seen that the light absorbance remained very similar even though surface functionalization changed. Using a dPGS layer did not induce aggregation as this would have changed the absorbance spectra by inducing a significant bathochromic shift. Reconstitution of the light absorbance from the optoacoustic signal perfectly fitted the light absorbance of the compound measured in the spectrometer. By looking at the different concentrations of gold nanorods, expressed by the optical density (OD), we investigated the concentration dependent optoacoustic signal generation in phantoms. Figure 5B shows that the overall optoacoustic spectra shape remained the same at different concentrations, enabling identification of the compound at concentrations as low as 0.05 OD. Figure 5C displays optoacoustic signals as a function of concentration and indicates a linear correlation between the two, with a coefficient of determination of more than 0.92. With the confirmation that the AuNR-dPGS can be identified in a quantita-

tive manner in the optoacoustic system, the stage is set for *in vivo* experiments.
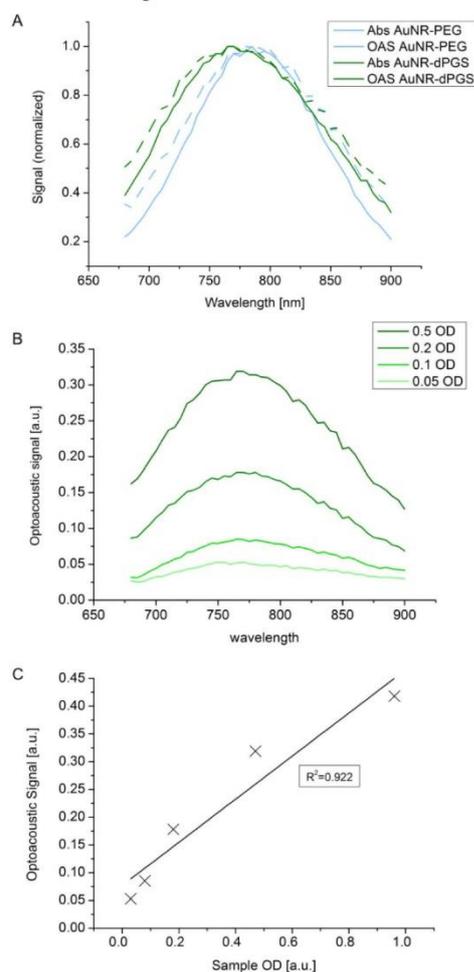
Figure 5. (A) Phantom study of AuNR-dPGS as optoacoustic imaging contrast agents. Optoacoustic signal (OAS) and light absorbance (Abs) comparison of gold nanorods functionalized with either PEG or dPGS. **(B)** Wavelength-dependent influence of the concentration of AuNR-dPGS on the optoacoustic signal shape at different optical densities. **(C)** Intensity of the optoacoustic signal relative to the concentration of the AuNR-dPGS sample.

Further investigations to estimate the potency of the AuNR-dPGS *in vivo* were performed with a well-established murine arthritis model that selectively triggered rheumatoid arthritis in the left injected limb. Figure 6 compares transverse images of two representative sample animals that exhibited

Polyglycerolsulfate functionalized gold nanorods as optoacoustic signal nanoamplifiers for in vivo bioimaging of rheumatoid arthritis

moderate arthritis (stage 2 using clinical criteria) in their left ankle 4 h after intravenous injection with gold nanorods bearing either PEG or dPGS. (3D models of the lower part of the animals injected with AuNR-dPGS and AuNR-PEG can be found in supplementary movies). From the observed images acquired at the maximum absorbance wavelength of the gold nanorods (800 nm, Figure 6A and 6D), no molecular information can be extracted because they depict both nanoparticle and blood signal. Spectral unmixing depicted in Figure 6B and 6E was done to identify and determine the exact location and accumulation of the nanoparticles in the joint. The same processing technique can be applied to blood, in the form of oxygenated hemoglobin, to yield a vasculature map of the region of interest and is presented in panels Figure 6C and 6F.

The colocalizing signals in Figure 6B and 6C nicely show that AuNR-PEG did not seem to accumulate in either articulation as expected, and preferentially stayed in the blood flow as both signals colocalized nicely. This is justified by the long circulation times typically exhibited by PEG coated particles *in vivo*. In that case, the signals provided by the gold on both sides were equivalent with a difference of a mean signal value of less than 10% (n=2). Because of its inflammation targeting characteristics, AuNR-dPGS featured a significantly higher signal in the left (arthritic) ankle of the animal. When measuring the mean signal values shown in Figure 6, the left ankle exhibited 1.7 times more signal than the right side control (4.59 to 2.73 a.u., respectively). On average,

the arthritic leg of animals injected with AuNR-dPGS presented 1.7 ± 0.3 times more signal than their healthy leg (n=4). As AuNR-dPGS binds to the vascularly presented P-selectin as an inflammation specific target, a staining of the respective blood vessel section was observed. Furthermore, the AuNR-dPGS signal clearly diffused from the blood vessels of the arthritic ankle into the inflamed tissue. This indicates that the enhanced permeability of the vasculature *per se* is not sufficient to allow for extravasation of the nanorods, but that the active targeting, achieved here by the dPGS functionalization, appears to be necessary [51]. In a recent study, we described the tissue accumulation of dPGS in a comparable arthritic mouse model and found a colocalization with the infiltrate of inflammatory cells [22]. Therefore, it is possible that AuNR-dPGS recognized and bound to leukocytes and co-extravasate to the inflammatory tissue [52]. In addition, specific binding of AuNR-dPGS to inflammation relevant cytokines is conceivable. In the case of dPGS functionalization, this active targeting has the advantage of facilitating retention of the contrast agent, something which is impossible with untargeted AuNR-PEG. In imaging terms, this translates into an accumulation of nanoparticles and a noticeable increase in contrast, which enables diagnosis of this inflammatory disease through imaging and a direct distinction between healthy and arthritic joints. Finally, it is our hope that AuNR-dPGS turns out to act as a theragnostic agent that in addition to its imaging property also dampens inflammation due to its anti-complement activity [9].
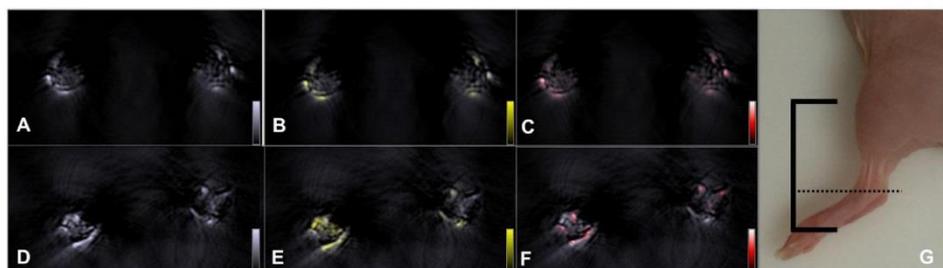

Figure 6. Accumulation of gold nanorods in the ankle of an arthritic mouse. Top row: anatomic optoacoustic images acquired at (A) 800 nm illumination wavelength, (B) overlayed with the signal coming from AuNR-PEG (yellow scale) or (C) with oxygenated hemoglobin signal (red scale). Bottom row: anatomic optoacoustic image acquired at (D) 800 nm illumination wavelength, (E) overlayed with the signal coming from AuNR-dPGS (yellow) or (F) with oxygenated hemoglobin signal (red scale). (G) Photograph of a mouse leg indicating the scanning region (solid lines) with the corresponding imaging plane displayed in the left panels (dotted line).

4. Conclusions

Dendritic polyglycerolsulfate functionalized gold nanorods were shown to be a promising candidate as contrast agent for the imaging of inflammatory diseases, *i.e.*, rheumatoid arthritis, *via* MSOT.

Gold nanorods were functionalized with dPGS by a thermally induced exchange of PEG-thiol ligands on the nanorod surface. This novel ligand exchange requires no additional solvents or challenging reaction conditions and offers a universal way for the covalent

Polyglycerolsulfate functionalized gold nanorods as optoacoustic signal nanoamplifiers for in vivo bioimaging of rheumatoid arthritis

640

functionalization of gold nanorods with hydrophilic ligands. The complete removal of CTAB before addition of polyanions significantly lowers the cytotoxicity of the resulting gold nanorods in comparison to other polysulfated gold nanorods reported in literature. Furthermore, we were able to show that the changes of SPR bands by plasmon coupling upon agglomeration can be utilized for the confirmation of a quantitative removal of unbound ligands with high sensitivity. The inflammation targeting potential of the AuNR-dPGS, which was evaluated *in vitro* by SPR in a competitive L-selectin binding assay, revealed a striking IC_{50} value of 135 pM. Functional testing under more physiological conditions in a flow chamber further confirmed inhibition of L-selectin mediated leukocyte adhesion with an IC_{50} below 10 nM. Further investigation on the efficiency of the dPGS coated colloid was performed with an *in vivo* imaging technique that allowed visualization, identification, and mapping of the gold nanorods without any chemical alteration. MSOT studies in a rheumatoid arthritis model were not only able to visualize and identify the signal of the nanorods, but were also able to highlight the better targeting potential of the functional polymer coating than classical AuNR-PEG, thereby inducing a significant contrast difference between healthy and arthritic joints. By demonstrating the synthesis, *in vitro* properties, and *in vivo* imaging possibilities offered by AuNR-dPGS, we show a promising tool for enabling diagnosis of inflammatory diseases through volumetric molecular imaging using the example of rheumatoid arthritis. Even though the biodistribution and *in vivo* toxicity remain to be investigated, the combination of the readily available gold nanorods as an imaging modality and the low-cost of dPGS for targeting paves the way for further research on other inflammatory diseases. Particularly when photothermal therapy can be applied using the gold core of the nanoparticle for cancer for example, the AuNRs-dPGS has great theranostic potential. Furthermore, as the residual amine groups on the TA-dPGS can be further functionalized with additional drugs or imaging modalities, AuNR-dPGS are perfectly suited as a platform for future research in multimodal imaging and theranostics.

Supplementary Material

Additional File 1:
Figure S1-S13.
http://www.thno.org/v04p0629s1.pdf
Additional File 2:
Leukocyte binding flow chamber assay.
http://www.thno.org/v04p0629s2.avi
Additional File 3:
MSOT imaging of arthritic mice - the left ankles are inflamed.
http://www.thno.org/v04p0629s3.avi

Competing Interests

The authors have declared that no competing interest exists.

References

1. Ntziachristos V, Razansky D. Molecular imaging by means of multispectral optoacoustic tomography (MSOT). Chem Rev. 2010; 110: 2783-94.
2. Ntziachristos V. Going deeper than microscopy: the optical imaging frontier in biology. Nat Methods. 2010; 7: 603-14.
3. Manohar S. Gold nanorods as molecular contrast agents in photoacoustic imaging: the promises and the caveats. Contrast Media Mol Imaging. 2011; 6: 389-400.
4. Bao C, Beziere N, del Pino P, et al. Gold nanoprisms as optoacoustic signal nanoamplifiers for in vivo bioimaging of gastrointestinal cancers. Small. 2013; 9: 68-74.
5. Tomography O, Herzog E, Taruttis A, et al. Optical imaging of cancer heterogeneity with Multispectral. Radiology. 2012; 263: 461-8.
6. Huang X, Neretina S, El-Sayed M. Gold nanorods: from synthesis and properties to biological and biomedical applications. Adv Mater. 2009; 19122: 4880-910.
7. Zhang Z, Wang J, Chen C. Gold nanorods based platforms for light-mediated theranostics. Theranostics. 2013; 3: 223-38.
8. Alkilany AM, Thompson LB, Boulos SP, et al. Gold nanorods : Their potential for photothermal therapeutics and drug delivery , tempered by the complexity of their biological interactions. Adv Drug Deliv Rev. 2012; 64: 190-9.
9. Dernedde J, Rausch A, Weinhart M, et al. Dendritic polyglycerol sulfates as multivalent inhibitors of inflammation. PNAS. 2010; 107: 19679-84.
10. Weinhart M, Gröger D, Enders S, et al. The role of dimension in multivalent binding events: structure-activity relationship of dendritic polyglycerol sulfate binding to L-selectin in correlation with size and surface charge density. Macromol Biosci. 2011; 11: 1088-98.
11. Ley K. The role of selectins in inflammation and disease. Trends Mol Med. 2003; 9: 263-8.
12. Jung U, Ley K, Alerts E. Mice Lacking Two or All Three Selectins Demonstrate Overlapping and Distinct Functions for Each Selectin. J Immunol. 2014; 162: 6755-62.
13. Lowe JB. Glycosylation in the control of selectin counter-receptor structure and function. Immunol Rev. 2002; 186: 19-36.
14. Everts M, Kok RJ, Ásgeirsdóttir SA, et al. Selective Intracellular Delivery of Dexamethasone into Activated Endothelial Cells Using an E-Selectin-Directed Immunoconjugate. J Immunol. 2014; 168: 883-9.
15. Lindner JR, Song J, Christiansen J, et al. Ultrasound Assessment of Inflammation and Renal Tissue Injury With Microbubbles Targeted to P-Selectin. Circulation. 2001; 104: 2107-12.
16. Gompels LL, Madden L, Lim NH, et al. In vivo fluorescence imaging of E-selectin: quantitative detection of endothelial activation in a mouse model of arthritis. Arthritis Rheum. 2011; 63: 107-17.
17. Sanders WJ, Katsumoto TR, Bertozzi CR, et al. L-Selectin-Carbohydrate Interactions : Relevant Modifications of the Lewis x. Biochemistry. 1996; 2960: 14862-7.
18. Somers WS, Tang J, Shaw GD, et al. Insights into the Molecular Basis of Leukocyte Tethering and Rolling Revealed by Structures of P- and E-Selectin Bound to SLe X and PSGL-1. Cell. 2000; 103: 467-79.

Polyglycerolsulfate functionalized gold nanorods as optoacoustic signal nanoamplifiers for in vivo bioimaging of rheumatoid arthritis

641

19. Koenig A, Jain R, Karin RV, et al. Selectin inhibition : synthesis and evaluation of novel sialylated , sulfated and fucosylated oligosaccharides , including the major capping group of GlyCAM-1. Glycobiology. 1997; 7: 79-93.

20. Woelke AL, Kuehne C, Meyer T, et al. Understanding selectin counter-receptor binding from electrostatic energy computations and experimental binding studies. J Phys Chem B. 2013; 117: 16443-54.

21. Weinhart M, Gröger D, Enders S, et al. Synthesis of dendritic polyglycerol anions and their efficiency toward L-selectin inhibition. Biomacromolecules. 2011; 12: 2502-11.

22. Licha K, Welker P, Weinhart M, et al. Fluorescence imaging with multifunctional polyglycerol sulfates: novel polymeric near-IR probes targeting inflammation. Bioconjugate Chem. 2011; 22: 2453-60.

23. Taruttis A, Wildgruber M, Kosanke K, et al. Multispectral optoacoustic tomography of myocardial infarction. Photoacoustics. 2013; 1: 3-8.

24. Biffi S, Dal Monego S, Dullin C, et al. Dendritic polyglycerolsulfate near infrared fluorescent (NIRF) dye conjugate for non-invasively monitoring of inflammation in an allergic asthma mouse model. PLoS One. 2013; 8: e57150.

25. Jana NR. Gram-scale synthesis of soluble, near-monodisperse gold nanorods and other anisotropic nanoparticles. Small. 2005; 1: 875-82.

26. Gole A, Murphy C. Polyelectrolyte-coated gold nanorods: synthesis, characterization and immobilization. Chem Mater. 2005; 3: 1325-30.

27. Villiers MM De, Otto DP, Strydom SJ, et al. Introduction to nanocoatings produced by layer-by-layer (LbL) self-assembly. Adv Drug Deliv Rev. 2011; 63: 701-15.

28. Hu X, Gao X. Multilayer coating of gold nanorods for combined stability and biocompatibility. Phys Chem Chem Phys. 2011; 13: 10028-35.

29. Wijaya A, Hamad-Schifferli K. Ligand customization and DNA functionalization of gold nanorods via round-trip phase transfer ligand exchange. Langmuir. 2008; 24: 9966-9.

30. Tsai D-H, Shelton MP, DelRio FW, et al. Quantifying dithiothreitol displacement of functional ligands from gold nanoparticles. Anal Bioanal Chem. 2012; 404: 3015-23.

31. Brand DD, Latham K a, Rosloniec EF. Collagen-induced arthritis. Nat Protoc. 2007; 2: 1269-75.

32. Liu W, Howarth M, Greytak AB, et al. Compact Biocompatible Quantum Dots Functionalized for Cellular Imaging. JACS. 2008; 130(4) :1274-84.

33. Papp I, Dernedde J, Enders S, et al. Modular synthesis of multivalent glycoarchitectures and their unique selectin binding behavior. chem commun. 2008; 44:5851-3.

34. Enders S, Bernhard G, Zakrzewicz A, et al. Inhibition of L-selectin binding by polyacrylamide-based conjugates under defined flow conditions. BBA. 2007; 1770: 1441-9.

35. Rosenthal A, Razansky D, Ntziachristos V. Quantitative optoacoustic signal extraction using sparse signal representation. Opt Express. 2009; 28: 1997-2006.

36. Gröger D, Paulus F, Licha K, et al. Synthesis and biological evaluation of radio and dye labeled amino functionalized dendritic polyglycerol sulfates as multivalent anti-inflammatory compounds. Bioconjugate Chem. 2013; 24: 1507-14.

37. Rostro-Kohanloo BC, Bickford LR, Payne CM, et al. The stabilization and targeting of surfactant-synthesized gold nanorods. Nanotechnology. 2009; 20: 434005.

38. Boca SC, Astilean S. Detoxification of gold nanorods by conjugation with thiolated poly(ethylene glycol) and their assessment as SERS-active carriers of Raman tags. Nanotechnology. 2010; 21: 235601.

39. Kassam A, Bremner G, Clark B, et al. Place exchange reactions of alkyl thiols on gold nanoparticles. JACS. 2006; 128: 3476-7.

40. Saad P, Flach C. Infrared spectroscopic studies of sodium dodecyl sulphate permeation and interaction with stratum corneum lipids in skin. Int J Cosmet Sci. 2012; 34(1) :36-43.

41. Verdon J, Falge M, Maier E, et al. Detergent-like activity and alpha-helical structure of warnericin RK, an anti-Legionella peptide. Biophys J. 2009; 97: 1933-40.

42. Hurst SJ, Lytton-jean AKR, Mirkin CA. Maximizing DNA Loading on a Range of Gold Nanoparticle Sizes. Anal Chem. 2006; 78: 8313-8.

43. Kinnear C, Dietsch H, Clift MJD, et al. Gold nanorods: controlling their surface chemistry and complete detoxification by a two-step place exchange. Angew Chem Int Ed. 2013; 52: 1934-8.

44. Rayavarapu RG, Petersen W, Hartsuiker L, et al. In vitro toxicity studies of polymer-coated gold nanorods. Nanotechnology. 2010; 21: 145101.

45. Yang YI, Choi I, Hong S, et al. Selective Aggregation of Polyanion-Coated Gold Nanorods Induced by Divalent Metal Ions in an Aqueous Solution. J Nanosci Nanotechnol. 2010; 10: 3538-42.

46. Jain PK, Eustis S, El-Sayed M a. Plasmon coupling in nanorod assemblies: optical absorption, discrete dipole approximation simulation, and exciton-coupling model. J Phys Chem B. 2006; 110: 18243-53.

47. Basu S, Panigrahi S, Praharaj S, et al. Dipole-dipole plasmon interactions in self-assembly of gold organosol induced by glutathione. New J Chem. 2006; 30: 1333-9.

48. Buscher K, Riese SB, Shakibaei M, et al. The transmembrane domains of L-selectin and CD44 regulate receptor cell surface positioning and leukocyte adhesion under flow. J Biol Chem. 2010; 285: 13490-7.

49. Alkilany AM, Nagaria PK, Hexel CR, et al. Cellular uptake and cytotoxicity of gold nanorods: molecular origin of cytotoxicity and surface effects. Small. 2009; 5: 701-8.

50. Rivera-Gil P, Jimenez de Aberasturi D, Wulf V, et al. The challenge to relate the physicochemical properties of colloidal nanoparticles to their cytotoxicity. Acc Chem Res. 2013; 46: 743-9.

51. Williams TJ, Brain SD, Hellewell PG, et al. Alteration in microvascular permeability induced by products released during inflammation. Prog Clin Biol Res. 1988; 263: 55-69.

52. Vestweber D, Blanks JE. Mechanisms that regulate the function of the selectins and their ligands. Physiol Rev 1999; 79: 181-213.

Polyglycerolsulfate functionalized gold nanorods as optoacoustic signal nanoamplifiers for in vivo bioimaging of rheumatoid arthritis

3.7   Synthesis, photophysical, and biological evaluation of sulfated polyglycerol dendronized perylenebisimides (PBIs)-a promising platform for anti-inflammatory theranostic agents?

Timm Heek*, Christian Kuehne*, Harald Depner, Katharina Achazi, Jens Dernedde, Rainer Haag
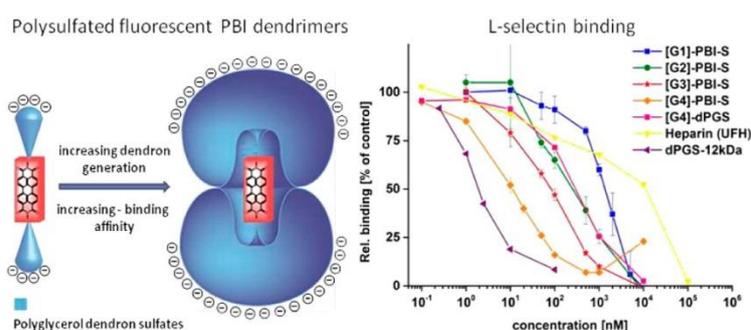
*Autoren trugen in gleichem Maße zur Arbeit bei.

Zu dieser Veröffentlichung hat der Autor mit Teilen des Konzepts, den Bindungsstudien, der Evaluation der Biokompatibilität und der Erstellung von Teilen des Manuskripts beigetragen.

Heek, T., C. Kuehne, H. Depner, K. Achazi, J. Dernedde and R. Haag (2016) Synthesis, Photophysical, and Biological Evaluation of Sulfated Polyglycerol Dendronized Perylenebisimides (PBIs)-A Promising Platform for Anti-Inflammatory Theranostic Agents? *Bioconjugate chemistry*. **27**, 727-36.

3.8 Size dependence of steric shielding and multivalency effects for globular binding inhibitors

Jonathan Vonnemann, Susanne Liese, Christian Kuehne, Kai Ludwig, Jens Dernedde, Christoph Böttcher, Roland R. Netz, Rainer Haag
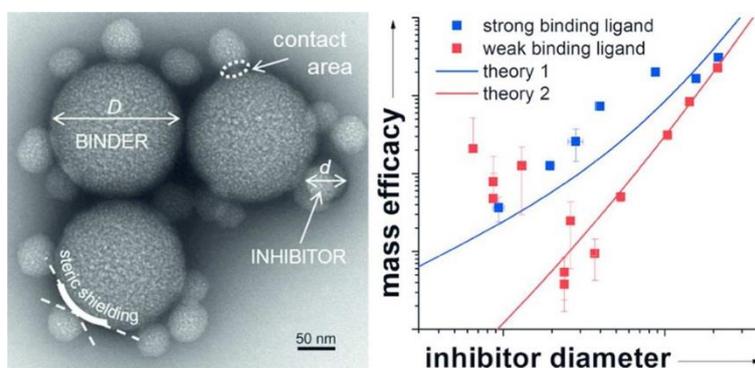
Zu dieser Veröffentlichung hat der Autor mit Teilen des Konzepts, der Entwicklung des SPR Bindungsassays, der Durchführung und Auswertung von Teilen der SPR Bindungsstudien und der Erstellung von Teilen des Manuskripts beigetragen.

Vonnemann, J., S. Liese, C. Kuehne, K. Ludwig, J. Dernedde, C. Bottcher, R. R. Netz and R. Haag (2015) Size dependence of steric shielding and multivalency effects for globular binding inhibitors. *Journal of the American Chemical Society*. **137**, 2572-9.

4 Zusammenfassung und Ergebnisse

Ziel der vorliegenden Arbeit war es neue Substanzen, die Adhäsionsrezeptoren adressieren, exemplarisch am Adhäsionsrezeptor L-Selektin zu untersuchen. Die strukturelle Charakterisierung von Ligand und Rezeptor ermöglicht ein rationales Design von Wirkstoffen.

Die *N*-terminale Lektindomäne der humanen Selektine, die mit Liganden interagiert, zeigt über alle drei Selektine hinweg eine Sequenzhomologie von über 50% und resultiert in einer gleichen dreidimensionalen Struktur. Es liegt nahe, bekannte co-kristallisierte Strukturen wie die von P-Selektin mit dem Liganden PSGL-1 als Vorlage zu nehmen, um die der anderen Selektine nach diesem Vorbild und anhand vorhandener Kristallstrukturen ohne Liganden zu modellieren. Die Gültigkeit der Modelle wurde am Beispiel von L-Selektin durch Bestimmung der Affinitäten zwischen dem Rezeptor und seinen Liganden sLex und sTyr überprüft. Dazu wurden ausgewählte Punktmutationen generiert und die Ligandbindung der Mutanten mit der des Wildtypproteins verglichen. Innerhalb der Loopsequenz, die für die Koordination von Ca^{2+} zuständig ist, befindet sich bspw. die konservierte Aminosäure Glutaminsäure an der Position 88 in der P-Selektin/PSGL-1-Struktur und trägt aktiv zur Koordination des Ca^{2+} bei. In der P-Selektin-Struktur ohne Liganden ist dieser Loop vom koordinierenden Zentrum weg orientiert und leistet keine Bindungsenergie für das Ca^{2+} (Abbildung 10, links). Eine Verkürzung dieser Aminosäure um ein C-Atom, also eine Mutation von Glutaminsäure zu Asparaginsäure (E88D) sollte, im Falle der Wichtigkeit von Glutaminsäure an dieser Position, zur Schwächung der Bindung des Ca^{2+}-Ions führen. Dadurch wird die Bindung zu sLex geschwächt und damit die gesamte Affinität von P-Selektin zu PSGL-1. Aufgrund der Sequenzhomologie zwischen den Selektinen müsste die Konformation des Loops in L- und E-Selektin analog dazu sein und eine entsprechende Mutation ebenfalls zur Reduktion der Affinität führen.
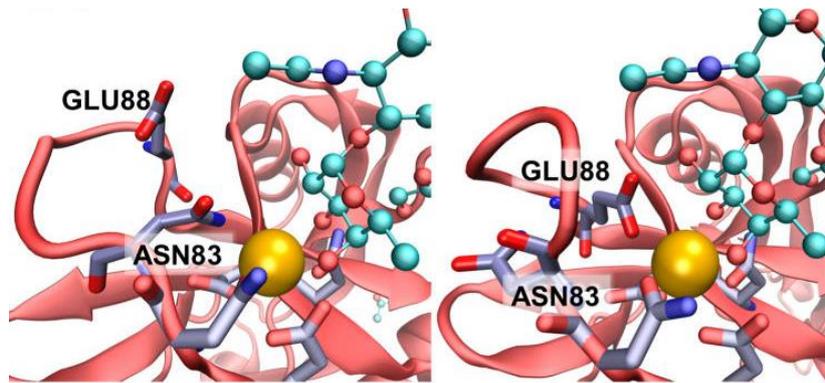
Abbildung 10: links: GLU88 (E88) in der *soaked* Struktur von P-Selektin; rechts: GLU88 (E88) in der *ko-kristallisierten* Struktur von P-Selektin (*Woelke *et al.* 2013)

Ein weiteres Beispiel ist in der L-Selektinsequenz die Asparaginsäure an Position 107 (D107) in der Koordinationsstelle für die Fukose im sLex. Im P- und E-Selektin ist an dieser Stelle eine um ein C-Atom längere Glutaminsäure präsent. Trotz der Homologie der Koordination von Fukose beider Selektine, unterscheidet sich P-Selektin im Bereich der Sialinsäure-Bindungsstelle (Aminosäuren 97-100) im Vergleich zu L- und E-Selektin signifikant und zeigt die schwächste Bindung zu sLex. E-Selektin andererseits, weist die höchste Affinität zu sLex auf, bindet aber keine sulfatierten Tyrosine, weshalb die Affinität zum Liganden PSGL-1 insgesamt weniger affin ist. In der modellierten E-Selektin/sLex-Struktur ist durch die kürzere Distanz der Säuregruppe zur Fukose sLex stärker gebunden. Dies wäre eine Erklärung für die höhere Affinität von E-Selektin zum Tetrasaccharid. Wenn die Vorhersagen also korrekt sind und die dreidimensionalen Strukturen der Selektine übereinstimmen, sollte die Veränderung von Asparaginsäure zu Glutaminsäure auch im L-Selektin Protein zu einer Bindungsverstärkung führen (D107E). In Abbildung 7 sind neben zwei Salzbrücken-betreffenden Mutationen die Ergebnisse zu den Mutationen E88D und D107E gezeigt. Für E88D sowie die beiden Salzbrückenmutationen K85A und R46A hat sich die Affinität wie vorhergesagt verschlechtert. Die ausgewählten Aminosäuren befinden sich nach Reorientierung am Vorbild von P-Selektin ko-kristallisiert mit PSGL-1 also in bindungsrelevanten Positionen, die sie vor der Anpassung in der einfach kristallisierten oder der *soaked* Struktur nicht eingenommen hatten. Wie zuvor bereits angedeutet, konnte für die Mutation D107E am Biliganden sLex und sTyr keine Bindungsverstärkung festgestellt werden, da hier ein Affinitätsgewinn durch die starken Interaktionen mit den sulfatierten Tyrosinen maskiert wird. Erst die Messung an sLex allein zeigt den Gewinn an Bindungsenergie und damit den Beweis für die Richtigkeit des angepassten Modells.

Die Kenntnis der Struktur des Rezeptors ermöglicht somit die gezielte Adressierung durch optimiertes Design synthetischer Liganden (*Woelke *et al.* 2013).

Die Verkürzung des von *Hicke et al.* beschriebenen originalen L-Selektin Aptamers von 36 auf 28 Nukleotide (*Riese *et al.* 2016) erhöht die DNA-Schmelztemperatur um theoretische 7°C und stabilisiert dadurch die Struktur ohne das wesentlich inhibitorisches Potential im SPR basierten L-Selektin-Inhibitionsassay eingebüßt wird. Damit ist der Bereich der Aptamerstruktur, die den Loop A bildet für dessen direkte Funktion nicht relevant. Im Gegensatz dazu sind Loop B und Loop C strukturgebend und somit bindungsrelevant wie der Verlust der Inhibition im kompetetiven Bindungsassay zeigt. Durch Dimerisierung über einen 9 Nukleotide langen Linker konnte der IC_{50} nochmal um Faktor 30 verbessert werden. Kürzere, als auch längere Linker, sowie die trimere Präsentation ergaben etwas schlechtere IC_{50}-Werte.

Die Mutationsanalyse der Aptamersequenz lieferte einen optimierten Rezeptor-bindenden Liganden und trägt entscheidend zum Verständnis der L-Selektin-Ligand Interaktion bei (*Riese *et al.* 2016).

Die neue, verkürzte Variante des L-Selektin-Aptamers ist immer noch hochaffin und konnte dank seiner Spezifität benutzt werden um L-Selektin aus einer komplexen Mischung (Zellkulturüberstand) heraus in einem Schritt aufzureinigen. Der direkte Vergleich zur *Ni-NTA* Affinitätschromatographie zur Reinigung *His*-markierten L-Selektins zeigt, dass das Protein mittels Aptamer ohne weitere Optimierung in hohen Ausbeuten erhalten wird. Zusätzlich ermöglichen die Eigenschaften Affinität und Spezifität die kalibrationsfreie Konzentrationsbestimmung und die Affinitätsmessung mittels SPR direkt aus dem komplexen Kulturmedium ohne Aufreinigung (*Kuehne *et al.* 2017).

Das dendritische Polyglycerolsulfat zeigt *in vitro* als auch *in vivo* sehr gute antiinflammatorische Eigenschaften ohne dabei im wirksamen Bereich große Auswirkungen auf Blutgerinnung oder Komplementaktivierung zu haben. Mit einem hydrodynamischen Durchmesser von 6 nm ist es theoretisch in einer Größenordnung welche problemlos über die Nieren ausgeschieden werden sollte. Allerdings akkumuliert dPGS in Leber und Milz, entweder durch direkte Bindung an ortsständige Rezeptoren oder vermittelte Interaktion mit Serumproteinen. Die dPGS-Derivate mit spaltbaren Linkern von *Reimann et al.* (*Reimann *et al.* 2015) zeigten in Untersuchungen durchweg ebenfalls sehr gutes antiinflammatorisches Potential ohne die Hämostase im entsprechenden Konzentrationsbereich stark zu

beeinflussen, ähnlich dem Verhalten von dPGS. In weiteren Biokompatibilitätsuntersuchungen konnte festgestellt werden, dass gerade die Thioether in der Lage sind die Aktivierung des Komplementsystems stark zu unterdrücken. Sowohl die Spaltbarkeit der Substanzen als auch ihr Einfluss auf Entzündungsreaktionen und das Komplementsystem würden sie für Szenarien prädestinieren, in denen speziell diese Kombination einen therapeutischen Effekt erzielt.

An Fluorophore oder andere Photoabsorber gekoppelte Polyanionen können zum Imaging von inflammatorischen Prozessen verwendet werden. In Kombination mit Absorbern die Anregungsenergie in Wärme umwandeln, ist dann auch die parallele Anwendung als Therapeutikum (Theranostika) denkbar. Zum Beispiel wurden mit dPGS dekorierte Goldnanostäbchen (gold nanorods, AuNR´s) erfolgreich zum Imaging von rheumatoider Arthritis in einem Mausmodell eingesetzt (*Vonnemann *et al.* 2014). Goldnanostäbchen eignen sich dazu besonders, da sie eine sehr hohe photothermale Konversion besitzen und nach Anregung wieder nahezu strahlungsfrei in den Grundzustand übergehen (Ntziachristos and Razansky 2010; Manohar *et al.* 2011). Durch gepulste Anregung eines Lasers emittieren sie Druckwellen nach thermoelastischer Expansion. Diese Ultraschallwellen können im Rahmen der *multispectral optoacoustic tomography* (MSOT), einem bildgebenden Verfahren, ausgewertet werden. Die sulfatierten Goldnanostäbchen zeigten gegenüber den unsulfatierten erwartungsgemäß ein hohes antiinflammatorisches Potential im SPR basierten L-Selektin Inhibitionsassay. IC_{50} Werte im mittleren picomolaren Bereich übertreffen hier 6 kDa großes dPGS um das 100 fache und sollten im Hinblick auf multivalenten Charakter und Affinität kritisch betrachtet werden, da hier mit den Goldnanostäbchen große Bindungsflächen am L-Selektin Goldnanopartikel abgeschirmt werden können (*Vonnemann *et al.* 2015). Im Mausmodell konnten die Goldnanostäbchen dann durch MSOT visualisiert werden. Dabei zeigten die dPGS dekorierten Stäbchen im Gegensatz zu den PEG funktionalisierten eine doppelt so hohe Akkumulation und damit ein Targeting im Bereich der induzierten Arthritis im Vergleich zum Fußgelenk, bei welchem diese nicht induziert wurde. Um ein anisotropisches Wachstum der Goldnanopartikel zu Goldnanostäbchen zu gewährleisten, wurden diese mit Cetyltrimethylammoniumbromid (CTAB) stabilisiert. Dieses kationische Detergens macht eine anionische Oberflächenfunktionalisierung synthetisch anspruchsvoll und muss vor der Bioapplikation aufgrund seiner Toxizität komplett entfernt werden. *Vonnemann et al.* beschreiben hier eine neue Methode zum zweistufigen Ligandenaustausch. Hierbei wird zuerst die kationische Schicht gegen eine neutrale PEG-Funktionalisierung getauscht, um in einem zweiten Schritt diese wiederum gegen dPGS zu tauschen. Die treibende Kraft hierbei

ist der Liponsäurelinker am dPGS, der im Gegensatz zur Thiolgruppe am PEG zweizähnig ist und Gold somit stärker koordinieren kann als der einzähnige Thiolrest.

Die Derivatisierung von Perylenbisimid (PBI) mit sulfatierten Polyglyceroldendronen ergibt definierte Strukturen und erlaubt daher genaue Aussagen zu Struktur-Wirkungsbeziehungen. Durch die Kopplung der Dendronen an das Fluorophor stieg dessen Wasserlöslichkeit und damit die Quantenausbeute in wässriger Lösung. Aggregation aufgrund hydrophober Effekte führt zum Löschen der Fluoreszenz. Werden die Fluorophore durch Derivatisierung mit wasserlöslichen Gruppen sterisch anspruchsvoller, können sie untereinander immer weniger hydrophobe Wechselwirkungen eingehen und werden nach und nach vereinzelt. Bei den hier verwendeten Polyglycerolen gekoppelt an PBI konnte dies bis zur Generation 3 der Dendronen beobachtet werden. Durch Sulfatierung konnte aber schon ab der 1. Generation die volle Quantenausbeute erreicht werden. Die sterisch anspruchsvollen Sulfate schirmen durch ihre Ladung schon ab der niedrigsten Generation ausreichend ab (*Heek *et al.* 2016). Durch die hohe Quantenausbeute und ihre Funktionalisierung mit Polyanionen können diese Substanzen sehr gut zum *in vitro* Imaging der Biodistribution von Polysulfatsystemen verwendet werden. Die hohe antiinflammatorische Wirkung im L-Selektin-Inhibitionsassay als auch die effiziente Unterdrückung des Komplementsystems bei geringen Konzentrationen könnte zusätzlich einen Einsatz als Entzündungshemmer indizieren. Im Vergleich zu Heparin ist der Einfluss auf die Blutgerinnung gering und beginnt erst beim 5 bis 10-fachen der Konzentration des IC_{50} im inhibitorischen Assay.

Bei flächigen, mehrbindigen Inhibitoren spielt neben der Multivalenz auch noch der, aufgrund der Größe des Inhibitors, nicht mehr frei zugängliche Raum am Rezeptor, die sterische Abschirmung (*steric shielding*) eine Rolle. Um den Effekt der sterischen Abschirmung durch globuläre Binder theoretisch zu erfassen, wurden zwei geometrische Kreismodelle erstellt. Eines beschreibt die komplette Abschirmung mit maximal möglicher Anzahl an koordinierten Inhibitoren (P_{max}, mit P = Anzahl an Inhibitoren notwendig für Abschirmung) und eines mit minimal notwendiger Anzahl an koordinierten Inhibitoren (P_{min}) (Abbildung 11). Die mathematischen Beschreibungen für beide Modelle sind in Abbildung 12 als Abhängigkeit der notwendigen Anzahl an Inhibitoren für die vollständige Abschirmung des Binders (P) gegen das Größenverhältnis zwischen Inhibitor und Binder aufgetragen (d/D).
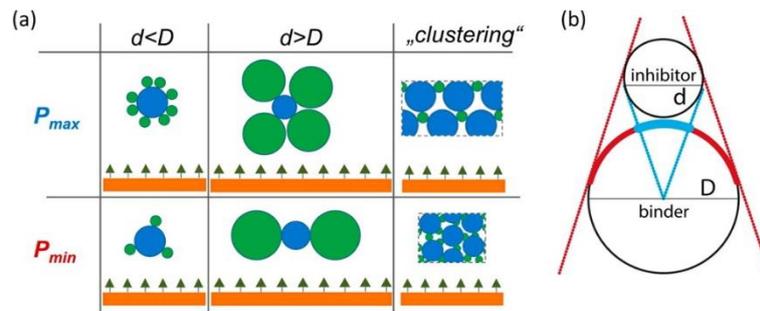
Abbildung 11: (a): geometrische Kreismodelle für P_{max} und P_{min} für verschiedene Randbedingungen d<D und d>D sowie für ein theoretisches *clustering* (b): Darstellung der Kontaktfläche (blau) zwischen Binder und Inhibitor sowie der sterisch abgeschirmten, für planare Oberflächen nicht mehr zugänglichen Fläche des Binders (rot) (*Vonnemann *et al.* 2015)

Um den Effekt der sterischen Abschirmung experimentell zu überprüfen, musste ein Modellsystem benutzt werden, bei dem der Inhibitor an den Binder schon bei geringen Konzentrationen komplett gebunden, die Affinität also sehr hoch ist. Der verwendete Streptavidin-Nanopartikel/Biotin-Nanopartikel Assay erfüllt diese Voraussetzung im gemessenen Bereich ($K_D \sim 10^{-15}$ M (Chaiet and Wolf 1964); eingesetzte Konzentration vom Binder: $\sim 10^{-12}$ M) und folgt dem vorhergesagten Modell für P_{max}. Im SPR basierten L-Selektin Inhibitionsassay, mit einem K_D von $\sim$500 nM von monovalentem L-Selektin an sLex-sTyr-PAA (*Woelke *et al.* 2013), spielen beide Effekte eine Rolle. Die experimentellen Werte folgen hier erst ab einem d/D Verhältnis von 0,3 dem Modell von P_{min}. Für Werte kleiner 0,3 weichen sie vom Modell ab und sind stark vom Multivalenzeffekt abhängig. Dadurch ist hier die inhibitorische Leistung von Inhibitorgrößen über d/D = 0,3 hier nur noch von der sterischen Abschirmung abhängig. Einen weiteren Gewinn durch multivalente Effekte gibt es nicht mehr.
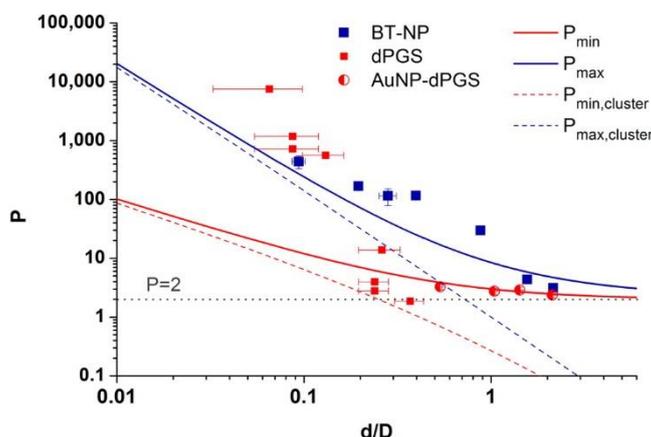
Abbildung 12: Grafische Darstellungen der mathematischen Beschreibungen für P_{min} und P_{max}. Die Anzahl der nötigen Inhibitoren **P** zur vollständigen Abschirmung eines Binders von einer planaren Oberfläche für verschiedene Größenverhältnisse Inhibitor/Binder (**d/D**). Der Biotin/Streptavidin Bindungsassay folgt dem Modell für die zufällige und damit maximale Koordination von Inhibitoren am Binder. Der L-Selektin Inhibitionsassay folgt dem Modell für die symmetrische Koordination, welche in der minimal nötigen Anzahl resultiert. Keiner der beiden Assays folgt dem Modell für das Clustern der Bindungspartner (gestrichelte Linie). (*Vonnemann *et al.* 2015)

Über das Modell kann nun zum einen vorausgesagt werden, ab welchen Inhibitorgrößen kein Affinitätsgewinn mehr stattfindet und allein noch das Volumen des Inhibitors steigt (Abbildung 13). Hier ist ab d/D = 0,3 eine Steigerung der inhibitorischen Leistung nur noch durch Größenzuwachs zu erreichen, der im Hinblick auf die *Clearance* eher zu vermeiden ist. Damit können aus den erstellten Modellen Prinzipien für das Design globulärer Inhibitoren anhand der Größe des Binders und K_D^{mono} (die Dissoziationskonstante, reduziert auf den monovalenten Fall) hergeleitet werden.
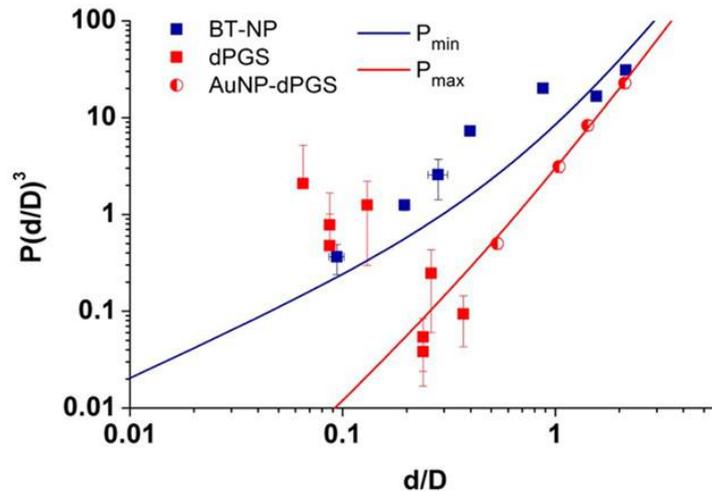
Abbildung 13: Die Volumen-normalisierte Darstellung von Abbildung 12 zeigt nach dem Erreichen der maximalen Bindungsaffinität einen starken Anstieg an benötigten Inhibitoren mit steigendem Volumen. (*Vonnemann *et al.* 2015)

Zum anderen kann aus dem gemessenen IC_{50} durch Bereinigung des Terms für die sterische Abschirmung der K_D^{multi} (Dissoziationskonstante für den multivalenten Binder) (Abbildung 14) und aus den Daten für die sukzessive Messung verschiedener Inhibitorgrößen auch der K_D^{mono} berechnet werden (Abbildung 15). Die Linearisierung der von P_{min} abweichenden Messungen ergibt einen K_D^{mono} von 94 nM und ist damit sehr gut vergleichbar mit dem experimentell bestimmten Wert von L-Selektin/Fc-Chimäre (divalent) an dPGS mit 45±17 nM (*Boreham *et al.* 2015).

$$IC_{50} = \underbrace{K_d^{multi}}_{\substack{\text{multivalency}\\\text{contribution}}} + \underbrace{0.5P[B]}_{\substack{\text{steric shielding}\\\text{contribution}}}$$

Abbildung 14: Die Konzentration eines multivalenten Inhibitors zur Inhibition eines multivalenten Binders um 50% ergibt sich im Wesentlichen aus dem Gleichgewicht zwischen am Binder gebundenem und ungebundenem Inhibitor, K_D^{multi} und der Hälfte der für eine sterische Abschirmung notwendigen Anzahl an Inhibitoren, 0,5P multipliziert mit der Konzentration der Binder [B] (*Vonnemann *et al.* 2015).
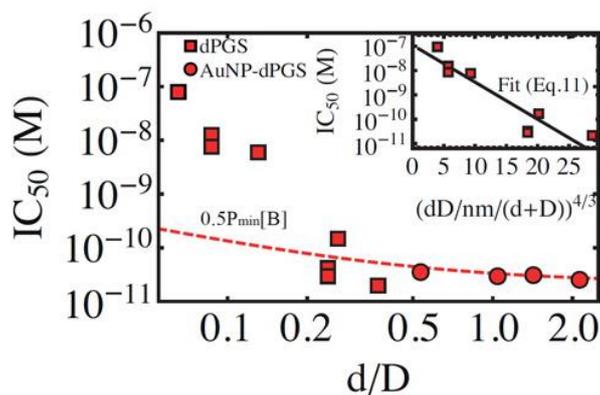
Abbildung 15: Aus der Linearisierung des stark multivalent geprägten Bereiches der Messreihe des L-Selektin Inhibitionsassays (für d/D<0,3) lässt sich bei Inhibitoren mit Durchmessern gegen 0 nm die Dissoziationskonstante K_D^{mono} ablesen (94 nM). (*Vonnemann *et al.* 2015)

Unspezifische Wirkstoffe adressieren ein breiteres Spektrum von Zielstrukturen. Um zusätzliche Bindungspartner neben der Zielstruktur L-Selektin zu identifizieren, wurden Konzepte und Assays zur *Traceability in vitro* (*Heek *et al.* 2016) und in *vivo* (*Vonnemann *et al.* 2014) beschrieben. Die Bindung an weitere Strukturen kann Nebeneffekte bedingen, welche im Rahmen von Biokompatibilitätsstudien (Blutgerinnung, Komplementaktivierung) untersucht wurden (*Reimann *et al.* 2015; *Heek *et al.* 2016). Auch konnte beim Einsatz hochmolekularer, globulärer Inhibitoren eine Limitation im Assaydesign zur Rezeptorbindung aufgezeigt werden, da das inhibitorische Potential von zwei synergistischen Effekten (Affinität und sterische Abschirmung) abhängt. Eine angepasste Datenevaluation erlaubt nun die mathematische Trennung beider Effekte (*Vonnemann *et al.* 2015).

5 Ausblick

Basierend auf den Ergebnissen dieser Arbeit können anhand der Kristallstruktur Inhibitoren rationaler designt werden. Die anschließende multivalente Präsentation auf geeigneten, biokompatiblen und spaltbaren Gerüstarchitekturen verspricht dann neben hoher Spezifität auch eine um ein Vielfaches stärkere Affinität. Durch spezielles Linkerdesign könnte die Spaltbarkeit variiert und damit die Bioverfügbarkeit moduliert werden.

Der Übergang von globulären Grundstrukturen hin zu flächigen Inhibitoren wie beispielsweise *Nanosheets* kann das Problem der großen Volumina bis zum Erreichen der maximalen Bindungsaffinität umgehen.

Eine Stabilisierung des DNA Aptamers durch PEGylierung, Kopplung von Polyglycerol oder Verwendung der Spiegelisomeren Form der Ribose (*L-Ribose*) als RNA Spiegelmer kann die Serumhalblebenszeit des Aptamers verlängern. Multivalent präsentiert kann dadurch ein hochspezifisches Targeting von L-Selektin erreicht werden.

Die Kombination spezifisch designter Binder für die einzelnen Selektine würde durch das relativ große therapeutische Fenster, sowie den multivalenten Charakter der Selektin/PSGL-1 Interaktion, das Anpassen der Therapie auf individuelle Krankheitsbilder oder sogar den einzelnen Patienten ermöglichen.

6 Abstract

6.1 Kurzzusammenfassung

Adhäsionsrezeptoren übernehmen zentrale Aufgaben bei Zell-Zell Kontakten und bei der Anbindung von Zellen an die extrazelluläre Matrix. Selektine spielen eine dominante Rolle bei der Rekrutierung von Leukozyten in entzündetes Gewebe.

Wichtig im Rahmen der angeborenen Immunität zum Bekämpfen von Pathogenen, aber ungewollt bei überschießender Entzündung, wie beispielsweise bei Autoimmunkrankheiten, ist die Modulation dieses Prozesses auf der Ebene der Selektine ein vielversprechender therapeutischer Ansatzpunkt. Mit Fokus auf das leukozytäre L-Selektin beschreibt diese Arbeit Ansätze zur Adressierung von Adhäsionsrezeptoren.

Rationales Design von spezifischen Proteinbindern erfordert die Kenntnis der Zielstruktur. Nicht immer sind entsprechende Kristallstrukturen vorhanden, können aber anhand bekannter, ähnlicher Strukturen modelliert werden. Hier wurden Selektinstrukturen auf der Basis der bekannten P-Selektin und E-Selektin Struktur modelliert und über Affinitätsmessungen generierter Mutationen von L-Selektin die Modelle verifiziert. Die Punktmutationen denen laut Modell eine Schwächung der Bindung prognostiziert wurde (R46A, K85A, E88D), zeigten in SPR Bindungsstudien signifikant höhere K_D Werte verglichen mit nicht mutiertem L-Selektin (das heißt R46A 2,1-fach, K85A 2,3-fach und E88D 2,9-fach höher). Die Mutation, für die eine stärkere Bindung an Sialyl Lewis^x (sLe^x) berechnet wurde (D107E), zeigte an einem Polymerliganden der nur sLe^x präsentiert signifikant stärkere Affinität (2,1-fach stärker), an einem Polymerliganden der sLe^x und sulfatiertes Tyrosin (sTyr) präsentiert, aber keinen Unterschied zu nicht mutiertem L-Selektin. Hier wird der Affinitätsgewinn an das sLe^x durch die starke Interaktion mit sTyr maskiert.

Binder können aber auch durch nachträgliche Optimierung einer Struktur rational designt werden, die durch nicht-rationale, evolutionäre Techniken wie SELEX entstanden sind. Im Rahmen dieser Arbeit wurde ein L-Selektin spezifisches DNA Aptamer hinsichtlich seiner Struktur-Wirkungs-Beziehung charakterisiert und die Sequenz auf wesentliche, bindungsrelevante Abschnitte verkürzt. Die entstandene finale Struktur zeigt eine höhere Stabilität ohne ihre hohe Bindungsaffinität zu verlieren, wobei Affinität und Spezifität auch durch Anwendung in einer Affinitätschromatographie demonstriert wurden. Trotz der Verkürzung um 8 Basen besitzt das Aptamer jetzt eine um 7°C höhere Schmelztemperatur und ein inhibitorisches Potential im SPR basierten L-Selektin Inhibitionsassay von IC_{50} = 11 nM, welches vergleichbar mit dem IC_{50} der originalen Struktur ist (8 nM).

Dimerisierung der verkürzten Struktur verbesserte den IC_{50} um ein 30-faches auf 0,3 nM. L-Selektin zeigt bei direkter Bindung an die neue Struktur eine Affinität von K_D = 11 nM.

Die Verwendung nicht-spezifischer Binder erfordert weitergehende Untersuchungen im Hinblick auf Bioverteilung, Akkumulation und *off-target* Effekte. Teile dieser Arbeit beschreiben zwei unterschiedliche Ansätze (anisotropische Goldnanostäbchen zur optoakustischen Bildgebung und intrinsische Fluoreszenz bspw. für die Fluoreszenzmikroskopie) zum Monitoring nicht-spezifischer L-Selektin Inhibitoren zur Anwendung *in vivo* und *in vitro*. Da das inhibitorische Potential nicht-spezifischer Polysulfate größtenteils von Größe und Ladung abhängt, rücken Fragen zur Biokompatibilität und Ausscheidung aus dem Organismus in den Fokus. Deshalb wurden Polysulfate mit spaltbaren Linkern neben inhibitorischem Potential auch auf Blutkompatibilität untersucht. Während die antiinflammatorischen Eigenschaften sowie der Einfluss auf die Blutgerinnung der Polyanionen mit den spaltbaren Linkern, mit denen der Grundstruktur ohne spaltbare Linker (dPGS) vergleichbar ist, weisen die spaltbaren dPGS Derivate aber einen verstärkten Einfluss auf die Blockade des Komplementsystems auf. Die Polysulfate mit intrinsischer Fluoreszenz, die sulfatierten Perylenbisimide (sPBI), zeigen mit steigender Anzahl an Sulfaten von Generation 1 (G1) bis Generation 4 (G4) eine Verbesserung des antiinflammatorischen Potentials um jeweils das 4-6 Fache. G4 mit 64 Sulfaten ist dann um das 30-fache potenter (IC_{50} = 11 nM) als ein dPGS-Molekül mit vergleichbarer Größe und vergleichbarer Anzahl an Sulfaten (IC_{50}: 300 nM). Hinsichtlich der Biokompatibilität steigt mit der Anzahl der Sulfate auch der Einfluss auf Blutgerinnung und Komplementaktivität. Dieser ist bei sPBI-G1 und sPBI-G2 bis 1 µM vernachlässigbar gering. Aber auch für sPBI-G3 und sPBI-G4 zeigt sich im Bereich des jeweiligen IC_{50} noch kein Einfluss auf die Blutkompatibilität.

Die Änderung der Größe eines multivalenten Inhibitors kann die Bindungsaffinität an ein multivalentes Target beträchtlich beeinflussen. Dadurch gewinnt ein anderer Faktor an Bedeutung, da größere Inhibitoren zusätzlich zum Anstieg der Affinität in der Lage sind, allein durch ihre Größe eine entsprechende Fläche am Binder abzuschirmen. Im Rahmen dieser Arbeit gelang es den Autoren, die sterische Abschirmung bei globulärer Inhibition mathematisch zu beschreiben und vom Multivalenzeffekt zu trennen.

6.2   Abstract

Adhesion receptors take over vital tasks in the attachment of cells to the extracellular matrix and in cell to cell binding communication. Here the selectins play a dominant role in the recruitment of leukocytes to inflamed tissue.

Desired in innate immunity to fight pathogens, but unwanted for example in autoimmune diseases, modulation of cell-cell recognition mediated by the selectins is a promising therapeutically approach. Focusing on L-selectin which is presented by leukocytes, this work describes approaches to target adhesion receptors.

Rational design of specific protein binders requires the knowledge of the target structure. However, if crystal structures aren´t available, configurations can be modelled based on known closely related structures. Selectin structures were modelled on the basis of a known P-selectin and E-selectin structure and subsequently verified via binding affinity of generated L-selectin mutants. The point mutations that were predicted to weaken the binding (R46A, K85A, E88D), showed significantly higher K_D values in SPR binding studies compared to non-mutated L-selectin (i.e. R46A 2.1-times, K85A 2.3-times und E88D 2.9-times higher). The mutation, for which a stronger binding to sialyl Lewis^x (sLe^x) was calculated (D107E), showed a significantly stronger binding to a polymeric ligand that presented only the sLe^x epitope (2.1-fach stronger), but didn't show any difference compared to the non-mutated L-selectin when bound to a polymer presenting both sLe^x and sTyr. Here the gain in affinity to sLe^x is hidden by strongly interacting sTyr ligands.

Rational design could be also achieved by applying non-rational evolutionary techniques like SELEX and further optimizing the ligand structure. Here an L-selectin specific DNA aptamer was characterized regarding its structure-function relationship and shortened to sections relevant for binding affinity. This approach yielded a final structure with higher stability without losing its high binding affinity and specificity, also demonstrated by its application as a ligand in a single step affinity chromatography. Despite the shortening by 8 bases, the aptamer now features a 7°C higher melting temperature and an inhibitory potential of $IC_{50} = 11$ nM in the SPR based L-selectin inhibition assay. This is comparable to the result of the original structure ($IC_{50} = 8$ nM). Dimerization of the shortened structure improved the IC_{50} by 30-fold yielding a value of 0,3 nM. L-selectin itself shows a direct binding affinity to the new structure of $K_D = 11$ nM.

The use of non-specific binders demands a closer look on biodistribution, accumulation and *off-target* effects. In this work two different approaches (anisotropic gold nanorods for

optoacoustic imaging and intrinsic fluorescence e.g. for fluorescence microscopy) of monitoring non-specific L-selectin inhibitors are presented. One for the use *in vivo* and the other one suited for *in vitro* experiments. As inhibitory potential is mainly dependent on size and charge of these non-specific polysulfates, biocompatibility and clearance are reaching the focus. Therefore cleavable linker equipped polysulfates for better clearance were probed for inhibitory potential and blood compatibility as well. While the polyanions with cleavable linkers have comparable properties compared to the template structure without cleavable linkers (dPGS) regarding anti-inflammatory potential as well as the influence on blood coagulation, the cleavable dPGS derivatives demonstrate a more potent anti-complement activity. The polysulfates with intrinsic fluorescence, the sulfated perylenebisimides (sPBI), show an increasing anti-inflammatory potential by the 4-6 fold with increasing number of sulfates from generation 1 (G1) to generation 4 (G4). G4 with 64 sulfates is 30-fold more potent (IC_{50}: 11 nM) than a dPGS-molecule of comparable size and with a comparable number of sulfates (IC_{50}: 300 nM). Regarding the biocompatibility, the impact on blood coagulation and complement activity rises with the number of sulfates. In sPBI-G1 and sPBI-G2, this impact is negligible below 1 µM. But even for sPBI-G3 and sPBI-G4 there is no impact on blood compatibility at their respective IC_{50} values.

The change of size of a multivalent inhibitor could dramatically alter binding affinity to a multivalent target. Here, another factor comes into play. Big globular inhibitors are able to shield a certain area of the binder simply due to size. In line with the scope of this work it was possible to describe steric shielding mathematically and to separate it from the rise of binding affinity due to the multivalent effect.

7 Literaturverzeichnis

Arbones, M. L., D. C. Ord, K. Ley, H. Ratech, C. Maynard-Curry, G. Otten, D. J. Capon and T. F. Tedder (1994) Lymphocyte homing and leukocyte rolling and migration are impaired in L-selectin-deficient mice. *Immunity*. **1**, 247-60.

Aydt, E. and G. Wolff (2002) Development of synthetic pan-selectin antagonists: A new treatment strategy for chronic inflammation in asthma. *Pathobiology*. **70**, 297-301.

Bevilacqua, M. P., S. Stengelin, M. A. Gimbrone, Jr. and B. Seed (1989) Endothelial leukocyte adhesion molecule 1: an inducible receptor for neutrophils related to complement regulatory proteins and lectins. *Science*. **243**, 1160-5.

*Boreham, A., J. Pikkemaat, P. Volz, R. Brodwolf, C. Kuehne, K. Licha, R. Haag, J. Dernedde and U. Alexiev (2015) Detecting and Quantifying Biomolecular Interactions of a Dendritic Polyglycerol Sulfate Nanoparticle Using Fluorescence Lifetime Measurements. *Molecules*. **21**, E22.

Bullard, D. C., E. J. Kunkel, H. Kubo, M. J. Hicks, I. Lorenzo, N. A. Doyle, C. M. Doerschuk, K. Ley and A. L. Beaudet (1996) Infectious susceptibility and severe deficiency of leukocyte rolling and recruitment in E-selectin and P-selectin double mutant mice. *The Journal of experimental medicine*. **183**, 2329-36.

Butcher, E. C. (1991) Leukocyte-endothelial cell recognition: three (or more) steps to specificity and diversity. *Cell*. **67**, 1033-6.

Campbell, J. J., J. Hedrick, A. Zlotnik, M. A. Siani, D. A. Thompson and E. C. Butcher (1998) Chemokines and the arrest of lymphocytes rolling under flow conditions. *Science*. **279**, 381-4.

Chaiet, L. and F. J. Wolf (1964) The Properties of Streptavidin, a Biotin-Binding Protein Produced by Streptomycetes. *Arch Biochem Biophys*. **106**, 1-5.

Chang, J., J. T. Patton, A. Sarkar, B. Ernst, J. L. Magnani and P. S. Frenette (2010) GMI-1070, a novel pan-selectin antagonist, reverses acute vascular occlusions in sickle cell mice. *Blood*. **116**, 1779-86.

Collins, R. G., U. Jung, M. Ramirez, D. C. Bullard, M. J. Hicks, C. W. Smith, K. Ley and A. L. Beaudet (2001) Dermal and pulmonary inflammatory disease in E-selectin and P-selectin double-null mice is reduced in triple-selectin-null mice. *Blood*. **98**, 727-35.

Dernedde, J., A. Rausch, M. Weinhart, S. Enders, R. Tauber, K. Licha, M. Schirner, U. Zugel, A. von Bonin and R. Haag (2010) Dendritic polyglycerol sulfates as multivalent inhibitors of inflammation. *Proceedings of the National Academy of Sciences of the United States of America*. **107**, 19679-84.

Dunne, J. L., C. M. Ballantyne, A. L. Beaudet and K. Ley (2002) Control of leukocyte rolling velocity in TNF-alpha-induced inflammation by LFA-1 and Mac-1. *Blood*. **99**, 336-41.

Ehrhardt, C., C. Kneuer and U. Bakowsky (2004) Selectins-an emerging target for drug delivery. *Advanced drug delivery reviews*. **56**, 527-49.

Enders, S., G. Bernhard, A. Zakrzewicz and R. Tauber (2007) Inhibition of L-selectin binding by polyacrylamide-based conjugates under defined flow conditions. *Biochimica et biophysica acta*. **1770**, 1441-9.

Ercolani, G. (2003) Assessment of cooperativity in self-assembly. *Journal of the American Chemical Society*. **125**, 16097-103.

Ercolani, G., C. Piguet, M. Borkovec and J. Hamacek (2007) Symmetry numbers and statistical factors in self-assembly and multivalency. *The journal of physical chemistry. B*. **111**, 12195-203.

Etzioni, A., C. M. Doerschuk and J. M. Harlan (1999) Of man and mouse: leukocyte and endothelial adhesion molecule deficiencies. *Blood*. **94**, 3281-8.

Fasting, C., C. A. Schalley, M. Weber, O. Seitz, S. Hecht, B. Koksch, J. Dernedde, C. Graf, E. W. Knapp and R. Haag (2012) Multivalency as a chemical organization and action principle. *Angewandte Chemie*. **51**, 10472-98.

Frenette, P. S., T. N. Mayadas, H. Rayburn, R. O. Hynes and D. D. Wagner (1996) Susceptibility to infection and altered hematopoiesis in mice deficient in both P- and E-selectins. *Cell*. **84**, 563-74.

Gumina, R. J., J. el Schultz, Z. Yao, D. Kenny, D. C. Warltier, P. J. Newman and G. J. Gross (1996) Antibody to platelet/endothelial cell adhesion molecule-1 reduces myocardial infarct size in a rat model of ischemia-reperfusion injury. *Circulation*. **94**, 3327-33.

*Heek, T., C. Kuehne, H. Depner, K. Achazi, J. Dernedde and R. Haag (2016) Synthesis, Photophysical, and Biological Evaluation of Sulfated Polyglycerol Dendronized Perylenebisimides (PBIs)-A Promising Platform for Anti-Inflammatory Theranostic Agents? *Bioconjugate chemistry*. **27**, 727-36.

Hicke, B. J., S. R. Watson, A. Koenig, C. K. Lynott, R. F. Bargatze, Y. F. Chang, S. Ringquist, L. Moon-McDermott, S. Jennings, T. Fitzwater, H. L. Han, N. Varki, I. Albinana, M. C. Willis, A. Varki and D. Parma (1996) DNA aptamers block L-selectin function in vivo. Inhibition of human lymphocyte trafficking in SCID mice. *The Journal of clinical investigation*. **98**, 2688-92.

Jenison, R. D., S. D. Jennings, D. W. Walker, R. F. Bargatze and D. Parma (1998) Oligonucleotide inhibitors of P-selectin-dependent neutrophil-platelet adhesion. *Antisense & nucleic acid drug development*. **8**, 265-79.

Johnston, G. I., R. G. Cook and R. P. McEver (1989) Cloning of GMP-140, a granule membrane protein of platelets and endothelium: sequence similarity to proteins involved in cell adhesion and inflammation. *Cell*. **56**, 1033-44.

Joshi, A., D. Vance, P. Rai, A. Thiyagarajan and R. S. Kane (2008) The design of polyvalent therapeutics. *Chemistry*. **14**, 7738-47.

Jung, U. and K. Ley (1999) Mice lacking two or all three selectins demonstrate overlapping and distinct functions for each selectin. *Journal of immunology*. **162**, 6755-62.

Jutila, M. A., T. K. Kishimoto and E. C. Butcher (1990) Regulation and lectin activity of the human neutrophil peripheral lymph node homing receptor. *Blood*. **76**, 178-83.

Kansas, G. S. (1996) Selectins and their ligands: current concepts and controversies. *Blood*. **88**, 3259-87.

Keelan, E. T., S. T. Licence, A. M. Peters, R. M. Binns and D. O. Haskard (1994) Characterization of E-selectin expression in vivo with use of a radiolabeled monoclonal antibody. *The American journal of physiology*. **266**, H278-90.

Kishimoto, T. K., M. A. Jutila, E. L. Berg and E. C. Butcher (1989) Neutrophil Mac-1 and MEL-14 adhesion proteins inversely regulated by chemotactic factors. *Science*. **245**, 1238-41.

Kishimoto, T. K., M. A. Jutila and E. C. Butcher (1990) Identification of a human peripheral lymph node homing receptor: a rapidly down-regulated adhesion molecule. *Proceedings of the National Academy of Sciences of the United States of America*. **87**, 2244-8.

Klopocki, A. G., T. Yago, P. Mehta, J. Yang, T. Wu, A. Leppanen, N. V. Bovin, R. D. Cummings, C. Zhu and R. P. McEver (2008) Replacing a lectin domain residue in L-selectin enhances binding to P-selectin glycoprotein ligand-1 but not to 6-sulfo-sialyl Lewis x. *The Journal of biological chemistry*. **283**, 11493-500.

Konstantopoulos, K., W. D. Hanley and D. Wirtz (2003) Receptor-ligand binding: 'catch' bonds finally caught. *Current biology : CB*. **13**, R611-3.

Kubes, P., M. Jutila and D. Payne (1995) Therapeutic potential of inhibiting leukocyte rolling in ischemia/reperfusion. *The Journal of clinical investigation*. **95**, 2510-9.

*Kuehne, C., S. Wedepohl and J. Dernedde (2017) Single-Step Purification of Monomeric l-Selectin via Aptamer Affinity Chromatography. *Sensors*. **17**, 226.

Lasky, L. A., M. S. Singer, T. A. Yednock, D. Dowbenko, C. Fennie, H. Rodriguez, T. Nguyen, S. Stachel and S. D. Rosen (1989) Cloning of a lymphocyte homing receptor reveals a lectin domain. *Cell*. **56**, 1045-55.

Ley, K., C. Laudanna, M. I. Cybulsky and S. Nourshargh (2007) Getting to the site of inflammation: the leukocyte adhesion cascade updated. *Nature reviews. Immunology*. **7**, 678-89.

Lou, J., T. Yago, A. G. Klopocki, P. Mehta, W. Chen, V. I. Zarnitsyna, N. V. Bovin, C. Zhu and R. P. McEver (2006) Flow-enhanced adhesion regulated by a selectin interdomain hinge. *The Journal of cell biology*. **174**, 1107-17.

Lowe, J. B. (2002) Glycosylation in the control of selectin counter-receptor structure and function. *Immunological reviews*. **186**, 19-36.

Maly, P., A. Thall, B. Petryniak, C. E. Rogers, P. L. Smith, R. M. Marks, R. J. Kelly, K. M. Gersten, G. Cheng, T. L. Saunders, S. A. Camper, R. T. Camphausen, F. X. Sullivan, Y. Isogai, O. Hindsgaul, U. H. von Andrian and J. B. Lowe (1996) The alpha(1,3)fucosyltransferase Fuc-TVII controls leukocyte trafficking through an essential role in L-, E-, and P-selectin ligand biosynthesis. *Cell*. **86**, 643-53.

Mammen, M., S.-K. Choi and G. M. Whitesides (1998) Polyvalent Interactions in Biological Systems: Implications for Design and Use of Multivalent Ligands and Inhibitors. *Angewandte Chemie International Edition*. **37**, 2754-2794.

Manohar, S., C. Ungureanu and T. G. Van Leeuwen (2011) Gold nanorods as molecular contrast agents in photoacoustic imaging: the promises and the caveats. *Contrast Media Mol Imaging*. **6**, 389-400.

Marshall, B. T., M. Long, J. W. Piper, T. Yago, R. P. McEver and C. Zhu (2003) Direct observation of catch bonds involving cell-adhesion molecules. *Nature*. **423**, 190-3.

Mayadas, T. N., R. C. Johnson, H. Rayburn, R. O. Hynes and D. D. Wagner (1993) Leukocyte rolling and extravasation are severely compromised in P selectin-deficient mice. *Cell*. **74**, 541-54.

Mehta, P., R. D. Cummings and R. P. McEver (1998) Affinity and kinetic analysis of P-selectin binding to P-selectin glycoprotein ligand-1. *The Journal of biological chemistry*. **273**, 32506-13.

Muller, W. A. (2002) Leukocyte-endothelial cell interactions in the inflammatory response. *Laboratory investigation; a journal of technical methods and pathology*. **82**, 521-33.

Ntziachristos, V. and D. Razansky (2010) Molecular imaging by means of multispectral optoacoustic tomography (MSOT). *Chem Rev*. **110**, 2783-94.

O'Connell, D., A. Koenig, S. Jennings, B. Hicke, H. L. Han, T. Fitzwater, Y. F. Chang, N. Varki, D. Parma and A. Varki (1996) Calcium-dependent oligonucleotide antagonists specific for L-selectin. *Proceedings of the National Academy of Sciences of the United States of America*. **93**, 5883-7.

Oishi, K., Y. Hamaguchi, T. Matsushita, M. Hasegawa, N. Okiyama, J. Dernedde, M. Weinhart, R. Haag, T. F. Tedder, K. Takehara, H. Kohsaka and M. Fujimoto (2014) A crucial role of L-selectin in C protein-induced experimental polymyositis in mice. *Arthritis & rheumatology*. **66**, 1864-71.

Paulus, F., R. Schulze, D. Steinhilber, M. Zieringer, I. Steinke, P. Welker, K. Licha, S. Wedepohl, J. Dernedde and R. Haag (2014) The effect of polyglycerol sulfate branching on inflammatory processes. *Macromolecular bioscience*. **14**, 643-54.

Poppe, L., G. S. Brown, J. S. Philo, P. V. Nikrad and B. H. Shah (1997) Conformation of sLe^x Tetrasaccharide, Free in Solution and Bound to E-, P-, and L-Selectin. *Journal of the American Chemical Society*. **119**, 1727-1736.

Pouyani, T. and B. Seed (1995) PSGL-1 recognition of P-selectin is controlled by a tyrosine sulfation consensus at the PSGL-1 amino terminus. *Cell*. **83**, 333-43.

*Reimann, S., D. Gröger, C. Kühne, S. B. Riese, J. Dernedde and R. Haag (2015) Shell Cleavable Dendritic Polyglycerol Sulfates Show High Anti-Inflammatory Properties by Inhibiting L-Selectin Binding and Complement Activation. *Advanced healthcare materials*. **4**, 2154-2162.

*Riese, S. B., K. Buscher, S. Enders, C. Kuehne, R. Tauber and J. Dernedde (2016) Structural requirements of mono- and multivalent L-selectin blocking aptamers for enhanced receptor inhibition in vitro and in vivo. *Nanomedicine : nanotechnology, biology, and medicine*. **12**, 901-8.

*Riese, S. B., C. Kuehne, T. F. Tedder, R. Hallmann, E. Hohenester and K. Buscher (2014) Heterotropic modulation of selectin affinity by allosteric antibodies affects leukocyte rolling. *Journal of immunology*. **192**, 1862-9.

Robinson, S. D., P. S. Frenette, H. Rayburn, M. Cummiskey, M. Ullman-Cullere, D. D. Wagner and R. O. Hynes (1999) Multiple, targeted deficiencies in selectins reveal a predominant role for P-selectin in leukocyte recruitment. *Proceedings of the National Academy of Sciences of the United States of America*. **96**, 11452-7.

Rodgers, S. D., R. T. Camphausen and D. A. Hammer (2001) Tyrosine sulfation enhances but is not required for PSGL-1 rolling adhesion on P-selectin. *Biophysical journal*. **81**, 2001-9.

Romig, T. S., C. Bell and D. W. Drolet (1999) Aptamer affinity chromatography: combinatorial chemistry applied to protein purification. *Journal of chromatography. B, Biomedical sciences and applications*. **731**, 275-84.

Sako, D., K. M. Comess, K. M. Barone, R. T. Camphausen, D. A. Cumming and G. D. Shaw (1995) A sulfated peptide segment at the amino terminus of PSGL-1 is critical for P-selectin binding. *Cell*. **83**, 323-31.

Siegelman, M. H., M. van de Rijn and I. L. Weissman (1989) Mouse lymph node homing receptor cDNA clone encodes a glycoprotein revealing tandem interaction domains. *Science*. **243**, 1165-72.

Siegelman, M. H. and I. L. Weissman (1989) Human homologue of mouse lymph node homing receptor: evolutionary conservation at tandem cell interaction domains. *Proceedings of the National Academy of Sciences of the United States of America*. **86**, 5562-6.

Singbartl, K., S. A. Green and K. Ley (2000) Blocking P-selectin protects from ischemia/reperfusion-induced acute renal failure. *FASEB journal : official publication of the Federation of American Societies for Experimental Biology*. **14**, 48-54.

Singbartl, K. and K. Ley (2000) Protection from ischemia-reperfusion induced severe acute renal failure by blocking E-selectin. *Critical care medicine*. **28**, 2507-14.

Somers, W. S., J. Tang, G. D. Shaw and R. T. Camphausen (2000) Insights into the molecular basis of leukocyte tethering and rolling revealed by structures of P- and E-selectin bound to SLe(X) and PSGL-1. *Cell*. **103**, 467-79.

Sunder, A., R. Hanselmann, H. Frey and R. Mulhaupt (1999) Controlled synthesis of hyperbranched polyglycerols by ring-opening multibranching polymerization. *Macromolecules*. **32**, 4240-4246.

Tedder, T. F., C. M. Isaacs, T. J. Ernst, G. D. Demetri, D. A. Adler and C. M. Disteche (1989) Isolation and chromosomal localization of cDNAs encoding a novel human lymphocyte cell surface molecule, LAM-1. Homology with the mouse lymphocyte homing receptor and other human adhesion proteins. *The Journal of experimental medicine*. **170**, 123-33.

Tedder, T. F., D. A. Steeber and P. Pizcueta (1995) L-selectin-deficient mice have impaired leukocyte recruitment into inflammatory sites. *The Journal of experimental medicine*. **181**, 2259-64.

Turk, H., R. Haag and S. Alban (2004) Dendritic polyglycerol sulfates as new heparin analogues and potent inhibitors of the complement system. *Bioconjugate chemistry*. **15**, 162-7.

*Vonnemann, J., N. Beziere, C. Bottcher, S. B. Riese, C. Kuehne, J. Dernedde, K. Licha, C. von Schacky, Y. Kosanke, M. Kimm, R. Meier, V. Ntziachristos and R. Haag (2014) Polyglycerolsulfate functionalized gold nanorods as optoacoustic signal nanoamplifiers for in vivo bioimaging of rheumatoid arthritis. *Theranostics*. **4**, 629-41.

*Vonnemann, J., S. Liese, C. Kuehne, K. Ludwig, J. Dernedde, C. Bottcher, R. R. Netz and R. Haag (2015) Size dependence of steric shielding and multivalency effects for globular binding inhibitors. *Journal of the American Chemical Society*. **137**, 2572-9.

Weinhart, M., D. Groger, S. Enders, S. B. Riese, J. Dernedde, R. K. Kainthan, D. E. Brooks and R. Haag (2011) The role of dimension in multivalent binding events: structure-activity relationship of dendritic polyglycerol sulfate binding to L-selectin in correlation with size and surface charge density. *Macromolecular bioscience.* **11**, 1088-98.

Weninger, W., L. H. Ulfman, G. Cheng, N. Souchkova, E. J. Quackenbush, J. B. Lowe and U. H. von Andrian (2000) Specialized contributions by alpha(1,3)-fucosyltransferase-IV and FucT-VII during leukocyte rolling in dermal microvessels. *Immunity.* **12**, 665-76.

*Woelke, A. L., C. Kuehne, T. Meyer, G. Galstyan, J. Dernedde and E. W. Knapp (2013) Understanding selectin counter-receptor binding from electrostatic energy computations and experimental binding studies. *The journal of physical chemistry. B.* **117**, 16443-54.

Wong, J., B. Johnston, S. S. Lee, D. C. Bullard, C. W. Smith, A. L. Beaudet and P. Kubes (1997) A minimal role for selectins in the recruitment of leukocytes into the inflamed liver microvasculature. *The Journal of clinical investigation.* **99**, 2782-90.

8 Abkürzungsverzeichnis

AuNR	Gold nanorod
CTAB	Cetyltrimethylammoniumbromid
d	Durchmesser Inhibitor
D	Durchmesser Binder
dPGS	dendritisches Polyglycerolsulfat
DREG	Down-regulated antigen
EGF	Epidermal growth factor
ELISA	Enzyme linked immunosorbent assay
FLIM	Fluorescence lifetime imaging microscopy
GPCR	G-protein-coupled receptors
IC_{50}	Inhibitorische Konzentration um 50% Restsignal zu erreichen
ICAM1	ICAM1 Intercellular adhesion
IgG	Immunglobulin G
K_D	Dissoziationskonstante
K_D^{mono}	Dissoziationskonstante monovalenter Binder
K_D^{multi}	Dissoziationskonstante multivalenter Binder
LAD-II	Leukocyte adhesion deficiency type-II
LFA-1	Lymphocyte function-associated antigen 1
LPS	Lipopolysaccharid
MADCAM1	Mucosal vascular addressin cell adhesion molecule 1
MSOT	Multispectral optoacoustic tomography
MST	Microscale Thermophoresis
Ni-NTA	Nickel-Nitrilotriessigsäure
NMR	Nuclear magnetic resonance
PAA	Polyacrylamid
PBI	Perylenbisimid
PEG	Polyethylenglycol
P_{max}	Abschirmung mit maximal möglicher Anzahl an koordinierten Inhibitoren

P_{min}	Abschirmung mit minimal notwendiger Anzahl an koordinierten Inhibitoren
PSGL-1	P-selectin glycoprotein ligand-1
ROMBP	Ring opening multibranching polymerisation
SCR	Short consensus repeat
SELEX	Systematic evolution of ligands by exponential enrichment
sLe^x	Sialyl Lewis^X
sLex-sTyr-PAA	Sialyl-Lewis^X und sulfatierte Tyrosine präsentiert auf Polyacrylamidrückgrat
sPBI	sulfatiertes Perylenbisimid
SPR	Surface plasmon resonance
sTyr	sulfatierte Tyrosine
VCAM1	Vascular cell adhesion protein 1
VLA-4	Very late antigen 4

9 Publikationen

***Kuehne, C.**, S. Wedepohl and J. Dernedde (2017) Single-Step Purification of Monomeric l-Selectin via Aptamer Affinity Chromatography. *Sensors*. **17**, 226.

*Wycisk, V., K. Achazi, P. Hillmann, O. Hirsch, **C. Kuehne**, J. Dernedde, R. Haag and K. Licha (2016) Responsive Contrast Agents: Synthesis and Characterization of a Tunable Series of pH-Sensitive Near-Infrared Pentamethines. *ACS Omega*. **1**, 808-817.

*Heek, T., **C. Kuehne**, H. Depner, K. Achazi, J. Dernedde and R. Haag (2016) Synthesis, Photophysical, and Biological Evaluation of Sulfated Polyglycerol Dendronized Perylenebisimides (PBIs)-A Promising Platform for Anti-Inflammatory Theranostic Agents? *Bioconjugate chemistry*. **27**, 727-36.

*Riese, S. B., K. Buscher, S. Enders, **C. Kuehne**, R. Tauber and J. Dernedde (2016) Structural requirements of mono- and multivalent L-selectin blocking aptamers for enhanced receptor inhibition in vitro and in vivo. *Nanomedicine : nanotechnology, biology, and medicine*. **12**, 901-8.

*Vonnemann, J., S. Liese, **C. Kuehne**, K. Ludwig, J. Dernedde, C. Bottcher, R. R. Netz and R. Haag (2015) Size dependence of steric shielding and multivalency effects for globular binding inhibitors. *Journal of the American Chemical Society*. **137**, 2572-9.

*Reimann, S., D. Gröger, **C. Kühne**, S. B. Riese, J. Dernedde and R. Haag (2015) Shell Cleavable Dendritic Polyglycerol Sulfates Show High Anti-Inflammatory Properties by Inhibiting L-Selectin Binding and Complement Activation. *Advanced healthcare materials*. **4**, 2154-2162.

*Mühlberg, M., M. G. Hoesl, **C. Kuehne**, J. Dernedde, N. Budisa and C. P. R. Hackenberger (2015) Orthogonal dual-modification of proteins for the engineering of multivalent protein scaffolds. *Beilstein Journal of Organic Chemistry*. **11**, 784-791.

*Boreham, A., J. Pikkemaat, P. Volz, R. Brodwolf, **C. Kuehne**, K. Licha, R. Haag, J. Dernedde and U. Alexiev (2015) Detecting and Quantifying Biomolecular Interactions of a Dendritic Polyglycerol Sulfate Nanoparticle Using Fluorescence Lifetime Measurements. *Molecules*. **21**, E22.

*Vonnemann, J., N. Beziere, C. Bottcher, S. B. Riese, **C. Kuehne**, J. Dernedde, K. Licha, C. von Schacky, Y. Kosanke, M. Kimm, R. Meier, V. Ntziachristos and R. Haag (2014) Polyglycerolsulfate functionalized gold nanorods as optoacoustic signal nanoamplifiers for in vivo bioimaging of rheumatoid arthritis. *Theranostics*. **4**, 629-41.

*Riese, S. B., **C. Kuehne**, T. F. Tedder, R. Hallmann, E. Hohenester and K. Buscher (2014) Heterotropic modulation of selectin affinity by allosteric antibodies affects leukocyte rolling. *Journal of immunology*. **192**, 1862-9.

*Woelke, A. L., **C. Kuehne**, T. Meyer, G. Galstyan, J. Dernedde and E. W. Knapp (2013) Understanding selectin counter-receptor binding from electrostatic energy computations and experimental binding studies. *The journal of physical chemistry*. *B*. **117**, 16443-54.

10 Curriculum Vitae

Der Lebenslauf wurde aus Gründen des Datenschutzes aus der Online-Version entfernt.

11 Danksagungen

An dieser Stelle möchte ich allen danken die diese Arbeit ermöglicht haben.

Prof. Dr. Hendrik Fuchs danke ich für die Übernahme des Erstgutachtens und für interessante als auch erheiternde Gespräche in den täglichen Mittagspausen.

Prof. Dr. Rainer Haag danke ich für Übernahme des Zweitgutachtens und sein unermüdliches Engagement bei der Realisierung des SFB 765 der diese Arbeit finanziert hat.

Dr. Jens Dernedde danke ich für die Überlassung des Themas und für die unkomplizierte und anschauliche Art mir als Chemiker komplexe biochemische Zusammenhänge in kürzester Zeit vollumfänglich erklärt zu haben.

Stefanie Wedepohl, Sebastian Riese, Paul O. Wafula, Figen Beceren-Braun, Luise Kosel, Thomas Hug und Kai Albring danke ich allen für das Anleiten, Lehren und Beibringen der verschiedensten Laborpraktiken.

Allen folgenden Personen danke ich in wertfreier, alphabetischer Reihenfolge für wissenschaftliche Diskussionen, Kooperationen, Hilfestellungen und ganz besonders wichtig, einfach sinnbefreite Blödeleien.

Alexandra Trautner	Daniel Stöbener	Katharina Achazi	Ronny Schulze
Anja Stöshel	Dominic Gröger	Kim Silberreis	Sabine Reimann
Anna Lena Wölke	Era Kapourani	Leonhard Urner	Serena Rossi
Benjamin Ziem	Falko Neumann	Luis Cuéllar Camacho	Shalini Kumari
Carlo Fasting	Hossein Panjideh	Marianne Boxberger	Susanne Liese
Cheenu Bhargava	Ievgen Donskyi	Nadine Rades	Timm Heek
Christian Schwedler	Johann Moschner	Nicole Niesler	Virginia Wycisk
Daniel Pushpa Raju	Jonathan Vonnemann	Paul Hillmann	

Nicht zuletzt danke ich meiner Familie für ihre Geduld und moralische Unterstützung, insbesondere Beatrice und meiner Tochter Mathilda die mich selbst nach dem längsten und anstrengendsten Arbeitstag aufzuheitern wussten.